Large-scale irrigation of Cr^{3+} into different octahedra of zinc aluminate toward continual broadband near-infrared emission

Lu Chen[a], Sisi Yu[a], Guichang Shen[b], Shuai Tang[b], Tao Zhang[c], Ji-Guang Li[d], Qi Zhu[a*]

[a]*Key Laboratory for Anisotropy and Texture of Materials (Ministry of Education), School of Materials Science and Engineering, Northeastern University, Shenyang, Liaoning 110819, China*

[b]*State Key Laboratory of Rolling and Automation, Northeastern University, Shenyang, Liaoning 110819, China*

[c]*Shenyang National Laboratory for Materials Science, Northeastern University, Shenyang, Liaoning 110819, China*

[d]*Research Center for Functional Materials, National Institute for Materials Science, Namiki 1-1, Tsukuba, Ibaraki 305-0044, Japan*

*Corresponding author

Dr. Qi Zhu

Tel: +86-24-8367-2700

E-mail: zhuq@smm.neu.edu.cn

ABSTRACT

Broadband near-infrared (NIR) phosphors, as key materials in NIR phosphor-converted light-emitting diodes (pc-LED) for emerging applications, have recently attracted considerable attention. Herein, by selecting a comprehensive engineering strategy of co-substituting [Al^{3+}-Al^{3+}] with [Mg^{2+}-Ge^{4+}] units and increasing Cr^{3+} concentration, a novel Cr^{3+}-doped $ZnAl_{1.16}Mg_{0.4}Ge_{0.4}O_4$ ($ZA(MG)_{0.4}$:2 at.%Cr^{3+}) phosphor with continual broadband NIR emission was synthesized. The site occupation of Mg^{2+}/Ge^{4+} in $ZnAl_2O_4$ is unraveled by Rietveld structure refinement and density functional theory (DFT) calculations. According to the photoluminescence behaviors, the formed defect clusters of $Zn_{Al}^{'}$-Cr^{3+}-$Ge_{Al}^{\cdot}$ and $Mg_{Al}^{'}$-Cr^{3+}-$Ge_{Al}^{\cdot}$ can not only introduce shallow defects to serve as new traps to obtain long-persistent luminescence but can also enhance the emission intensity at ~689 nm and ~694 nm. The quantity and scale of Cr^{3+}-Cr^{3+} pairs and Cr^{3+} in distorted sites, which can improve the thermal quenching resistance and emission intensity in the range of 700-800 nm, can be accurately regulated by varying the concentration of Cr^{3+}. Under 387 nm excitation, the designed material exhibits intensive NIR emission from 685 to 750 nm with a wide full-width at half maximum (FWHM) of 95 nm. The electroluminescence spectrum and potential applications of the NIR pc-LED prepared using $ZA(MG)_{0.4}$:2 at.%Cr^{3+} phosphor are also reported. The results promise a feasible strategy to develop NIR phosphors as NIR pc-LEDs lighting sources for applications in nondestructive detection and anticounterfeiting.

Keywords: Chemical unit co-substitution, Defect clusters, Distorted site, Near-infrared persistent luminescence, Broadband emission

1. Introduction

Recently, near-infrared (NIR) light sources have attracted considerable research attention due to their wide application in the fields of bioimaging/sensing, night vision, plant growth, food detection, anticounterfeiting, and so on [1-3]. Traditional NIR light sources, such as tungsten-halogen lamps and supercontinuum lasers, usually have the disadvantages of bulkiness, low luminous efficiency, poor thermal stability, and narrow emission bands. These traditional NIR sources are expected to be replaced by NIR phosphor-converted light-emitting diodes (pc-LEDs), which consist of an LED chip and NIR-emitting phosphors. NIR pc-LEDs have the advantages of compactness, portability, efficiency, and low energy consumption [4-7]. Therefore, developing a highly efficient broadband NIR-emitting phosphor is crucial for expansion applications, as the performance of NIR pc-LEDs is determined by the NIR phosphors used. Both rare earth ions, such as Eu^{2+}, and transition metal ions, such as Cr^{3+} and Mn^{2+}, can serve as activators for broadband NIR-emitting phosphors [8-10]. However, the currently Eu^{2+}-doped NIR phosphors typically exhibit low quantum efficiency and limited emission bandwidth. In contrast, Cr^{3+}-doped NIR phosphors have received considerable attention owing to their broadband and efficient NIR emission, which are regarded as the most promising NIR phosphors for NIR pc-LEDs [11, 12]. Many kinds of broadband NIR phosphors doped with Cr^{3+} have been reported recently, for instance, $Ga_4GeO_8:Cr^{3+}$ (λ_{em} = 850 nm; FWHM = 215 nm) [13], $LiGaP_2O_7:Cr^{3+}$ (λ_{em} = 840 nm; FWHM = 170 nm) [14], $Lu_2CaMg_2Ge_3O_{12}:Cr^{3+}$ (λ_{em} = 795 nm; FWHM = 152 nm) [15], and $Mg_2SnO_4:Cr^{3+}$ (λ_{em} = 800 nm; FWHM = 180 nm) [6]. Unfortunately, most of these Cr^{3+}-doped NIR phosphors still suffer from low thermal stability and insufficient effective broadband emission (the emission intensity reaches the maximum only at a certain wavelength), which will hinder their applications for pc-LEDs. Hence, it is necessary to develop Cr^{3+}-activated NIR phosphors to achieve highly efficient broadband NIR emission.

It is known that the d-d transition of Cr^{3+} is greatly affected by the crystal field environment, which is dependent on the crystal structure of the matrix [16]. Owing to

the appropriate bandgap and tunable crystal field, spinel oxides AB_2O_4 are suitable for hosting Cr^{3+} to generate broadband NIR emission accompanied by a long afterglow duration. Normally, AB_2O_4 comprises two types of coordination polyhedral with the divalent cation A occupying the tetrahedral site and trivalent cation B occupying the octahedral site [17]. The antisite defects generated by the exchange of cations A and B can introduce a local electric field and serve as energy storage centers, which are crucial for the persistent luminescence (PersL) and duration of $AB_2O_4:Cr^{3+}$ phosphors [18-20]. Among the spinel family, $ZnGa_2O_4$ and its related solid solutions are known to exhibit wide excitation and emission ranges as well as superlong NIR PersL due to a suitable number of antisite defects [21-23]. After being pre-charged by the excitation source, NIR PersL phosphors, which can continuously emit light for minutes to hours, have received particular interest as biomarker probes for background-free biomedical imaging [24]. Zinc aluminate ($ZnAl_2O_4$) is another AB_2O_4 compound with a similar structure to $ZnGa_2O_4$, which is considered a potential candidate for cost-prohibitive gallate and gallogermanate oxides. However, the low level of intrinsic antisite defects (less than 1%) results in unsatisfactory optical properties of $ZnAl_2O_4:Cr^{3+}$, including NIR photoluminescence (PL) and PersL [19, 20].

In consideration of the intensive influence of the matrix local structure on the optical properties of Cr^{3+}-activated phosphors, several strategies for broadening spectra and enhancing afterglow are effectively demonstrated. 1) Introducing dopants at the octahedral site to tailor the local crystal field around the activator center Cr^{3+}; this is because in the medium-strength ligand field with $Dq/B \approx 2.3$, Cr^{3+} would give a mixture of narrow-band emission (~700 nm) and broadband emission (650-1600 nm) originating from the $^2E \rightarrow {}^4A_2$ and $^4T_2 \rightarrow {}^4A_2$ transitions, respectively [25, 26]. For example, precise adjustment of the local crystal field around Cr^{3+} is realized by adding aluminum into the Sn^{4+} site of $Zn_2SnO_4:Cr^{3+}$ [27] or replacing gallium with tin in $ZnGa_2O_4$: Cr^{3+} [28] to obtain a tunable chromium emission band. 2) Generating distorted octahedral defects could enhance the luminescence of Cr^{3+} in distorted sites using the chemical unit co-substitution method. Moreover, the formed defect clusters can store and release excited electrons that contribute to the long-lasting NIR PersL and

excellent thermal stability [7, 22, 29]. Successful examples can be found in increasing the delayed emission and the NIR emission intensity of $ZnGa_2O_4$ by co-substitution of [Mg^{2+}-Ge^{4+}] for [Ga^{3+}-Ga^{3+}] [30, 31]. 3) Increasing the concentration of Cr^{3+} can not only improve the emission corresponding to Cr^{3+}-Cr^{3+} pairs [32, 33] but also increase the probability of Cr^{3+} neighboring antisite defects (denoted as Cr_{N2}^{3+}) and further increase the emission intensity of Cr_{N2}^{3+}. Thus, comprehensively engineering a distorted environment is of utmost importance for integrating the broadband NIR PL and PersL for $ZnAl_2O_4$:Cr^{3+}.

In this work, we designed and synthesized a high-content Cr^{3+}-doped $ZnAl_{1.16}Mg_{0.4}Ge_{0.4}O_4$ phosphor that exhibits continuous broadband near-infrared emission with a full width at half maximum (FWHM) of 95 nm *via* a solid-state reaction. [Mg^{2+}-Ge^{4+}] was first used to replace [Al^{3+}-Al^{3+}] in $ZnAl_2O_4$:Cr^{3+} to generate defect clusters of $Zn_{Al}^{'}$-Cr^{3+}-$Ge_{Al}^{\cdot}$ and $Mg_{Al}^{'}$-Cr^{3+}-$Ge_{Al}^{\cdot}$, which are beneficial for obtaining long-lasting NIR PersL and enhancing the emission intensity at ~689 nm and ~694 nm. Then, the introduction of excessive Cr^{3+} led to further enhancement of the emission intensity in the range of 700-800 nm, mainly due to Cr^{3+}-Cr^{3+} pairs and more Cr^{3+} in distorted sites. This work not only presents a comprehensive strategy for developing tunable NIR phosphors, but also demonstrates the potential applications for NIR pc-LEDs lighting sources.

2. Experimental section

2.1. Materials and synthesis

A series of $ZnAl_{1.975-2x}Mg_xGe_xO_4$:1.25 at.% Cr^{3+} (ZAMG:Cr^{3+}, x = 0-0.7), $ZnAl_{2-0.02y}O_4$:y at.%Cr^{3+} (ZAO:Cr^{3+}, y = 1-2), and $ZnAl_{1.2-0.02z}Mg_{0.4}Ge_{0.4}O_4$:$z$ at.%Cr^{3+} (ZA(MG)$_{0.4}$:Cr^{3+}, z = 1-2) phosphors were synthesized through high-temperature solid-state reaction. Al_2O_3 (99.99%), ZnO (99.99%), Cr_2O_3 (99.95%), MgO (99.99%), and GeO_2 (99.99%) purchased from Aladdin were employed as raw materials. The above materials were weighted accurately according to the stoichiometric ratio. And then, the mixtures were transferred into an agate mortar and finely grounded for 30 min to form homogeneous powders. After prefiring at 1000 ℃ for 2 h, the materials were ground again for more than 10 min and subsequently sintered at 1500 °C for 6 h in air

atmosphere.

2.2. Measurements and characterization

X-ray diffraction (XRD, Model SmartLab, Rigaku, Tokyo, Japan) operating at 40 kV/200 mA and using nickel-filtered Cu Kα radiation (λ = 0.15406 nm) was used to collect the XRD results of all samples. The data was measured at a scanning speed of 10° 2θ/min from 10° to 80° in the continuous-scan mode. The XRD data for Rietveld refinement was obtained in a step-scan mode over the 2θ range of 10-120°, using a step interval of 0.02° and a counting time of 1 s/step. Transmission electron microscopy (TEM, Model JEM-2000FX, JEOL, Tokyo) was employed to observe the morphology of product. Selected area electron diffraction (SAED) and High-Resolution TEM (HR-TEM) were used to further confirm the crystal structure of the samples. The structure of coordination polyhedral was evaluated using the Raman microscope (Model R-XploRA Plus, Horiba, Kyoto, Japan) with a 532 nm laser as the excitation source. The formation energies (ΔE_f) of different antisite configurations were calculated using density functional theory (DFT) method with the help of the Vienna ab initio Simulation Package (VASP) [34-36]. The electron interaction with ions was replaced by the projector augmented wave (PAW) method, and the generalized gradient approximation (GGA) with the Perdew-Burke-Ernzerhof (PBE) functional was employed as the exchange-correlation potential [37]. The cut-off energy E_{cut} for the plane-wave basis set was fixed value of 520 eV. The crystal lattice was fully relaxed until the force on each atom was less than 0.01 eV $Å^{-1}$. Diffuse reflectance (DR) spectra were performed on the UV-Vis-NIR spectrophotometer (UV-3600 Plus, Shimadzu, Kyoto, Japan). The photoluminescence spectra, including the PL and PLE spectra, at 77 K and in the range of 298-573 K were measured by the fluorospectrophotometer (Model FP-8600, Jasco, Tokyo) with a slit of 10 nm for both excitation and emission. The PL, PLE, persistent luminescence emission (PersL) spectra, as well as persistent luminescence decay curves at room temperature (RT) were recorded using a model JY FL3-21 spectrophotometer (Horiba, Kyoto). The night vision apparatus (P4-0118, ZHANEN, China) was employed to take NIR pictures. The thermoluminescence (TL) glow curves were measured using an FJ-427A TL meter (Beijing Nuclear Instrument Factory). The

samples were first exposed to an UV lamp for 10 min before collecting PersL spectra, PersL decay curves, NIR pictures, and TL curves.

2.3. LED performances

The NIR pc-LED device was fabricated by using the 395 nm UV chip and the as-synthesized $ZnAl_{1.16}Mg_{0.4}Ge_{0.4}O_4$:2 at.%$Cr^{3+}$ phosphor with NIR broadband emitting. The mass ratio of the mixture of type A and B epoxy resin to NIR phosphor was set as 1:1. The electroluminescence (EL) spectra of the fabricated NIR pc-LED were collected with a Model HS-1000 spectral detector (Otsuka Electronics Co. Ltd., Osaka, Japan). The photoelectric properties of the pc-LEDs were measured by using an OHSP-350M photoelectric measuring system (600-900 nm, HOPOOCOLOR, China). The forward bias current for pc-LEDs was 20-100 mA. The electro-optical conversion efficiency is defined as the ratio of the output power of NIR emission (600-900 nm) to the input electric power of LED. Use the rear-facing camera of iPhone as the visible camera. The demonstration images using NIR pc-LED as the lighting source were taken by the near infrared IR CMOS USB digital camera (ADOS-TECH, UAB, Europe, Lithuania).

3. Results and discussion

3.1. Crystal structure and local structure of $ZnAl_{1.975-2x}Mg_xGe_xO_4$:1.25 at.% Cr^{3+}

The XRD patterns of the as-synthesized $ZnAl_{1.975-2x}Mg_xGe_xO_4$:1.25 at.% Cr^{3+} (ZAMG:Cr^{3+}, x = 0-0.7), $ZnAl_2O_4$:y at.%Cr^{3+} (ZAO:Cr^{3+}, y = 1-2), and $ZnAl_{1.2}Mg_{0.4}Ge_{0.4}O_4$:$z$ at.%Cr^{3+} (ZA(MG)$_{0.4}$:Cr^{3+}, z = 1-2) samples are shown in Fig. 1a-c. The phase structure of a series of powders is compared with the standard file of JCPDS No.05-0669 of the $ZnAl_2O_4$ phase (spinel structure). All diffraction peaks of the products coincide well with those of the standard $ZnAl_2O_4$ phase, whereas a secondary impurity of Zn_2GeO_4 (hexagonal structure) appears for ZAMG:Cr^{3+} when x further increases to 0.7. According to the amplified view of the diffractions at 2θ = 30-38°, it is clear that the diffraction peaks gradually shift toward the lower 2θ side with increasing x value. Herein, the chemical unit of [Mg^{2+}-Ge^{4+}] is introduced into $ZnAl_2O_4$ to replace [Al^{3+}-Al^{3+}], which can be attributed to the lattice expansion induced by the replacement of [Mg^{2+}-Ge^{4+}] for [Al^{3+}-Al^{3+}] in the octahedral sites, considering that the average ionic radius of the co-substituted ion pair (r = 0.625 Å, CN (coordination

number) = 6) is larger than that of Al^{3+} (r = 0.535 Å, CN = 6) [22, 29]. The ionic radii with different coordination of each substitution ion and substituted ion are shown in Table 1. In addition, the acceptable radius of Mg^{2+} (r = 0.57 Å, CN = 4) allows it to partially replace Zn^{2+} (r = 0.60 Å, CN = 4) in the tetrahedral sites, while an equal amount of Zn^{2+} will replace Al^{3+}. Given that the ionic radius of Ge^{4+} (r = 0.53 Å, CN = 6) is close to that of Al^{3+}, Ge^{4+} is more likely to replace Al^{3+} than Zn^{2+}. However, Huang and Guo et al. proposed that Ge^{4+} may also enter tetrahedral sites in the case of $Zn_{1+x}Al_{2-2x}Ge_xO_4:Cr^{3+}$ [22]. For ZAMG:Cr^{3+}, whether Ge^{4+} may replace Al^{3+} or Zn^{2+} will be discussed later. Fig. 1d shows the TEM morphology of the x = 0.4 sample. SAED and HR-TEM were performed for single particle, as shown in Fig. 1e and f. The SAED pattern shows the presence of the (220) and (400) planes of cubic $ZnAl_2O_4$, and the results indicate that the nanoparticles are single-crystalline with good crystallinity. Clear resolved lattice fringes can be observed in the HR-TEM image, and the d spacing of 0.247 nm is assigned to the (311) plane of $ZnAl_2O_4$ (cubic structure, d(311) = 0.244 nm, JCPDS No. 05-0669). Because [Mg^{2+}-Ge^{4+}] and Cr^{3+} doping contribute to lattice expansion, the interplanar spacing of the (311) plane of the ZAMG:Cr^{3+} (x = 0.4) sample was larger than the pure $ZnAl_2O_4$. The above results indicate that the sample belongs to the target cubic crystal structure.

Table 1 Ionic radii of metal elements in ZAMG:Cr^{3+} spinel solid solution.

r (Å)	Zn^{2+}	Al^{3+}	Cr^{3+}	Mg^{2+}	Ge^{4+}
r (CN = 4)	0.60	0.39	-	0.57	0.39
r (CN = 6)	0.74	0.535	0.615	0.72	0.53

To further elucidate the local structure evolution with the [Mg^{2+}-Ge^{4+}] unit co-substitution, the Rietveld refinement of the as-prepared ZAMG:Cr^{3+} (x = 0, 0.2, 0.4, and 0.6) samples was performed using TOPAS software, and the results are shown in Fig. 2a-d. All peaks can be indexed by cubic cell (*Fd3m*) and their parameters are close to the $ZnAl_2O_4$ spinel structure; hence, the crystallographic data of standard $ZnAl_2O_4$ (ICSD 94156) was taken as the initial structure model. The calculated data fit well with the experimental patterns, and the residual factors (R_{wp}, R_p and χ^2) show considerable credibility (Table S1). The consistency between the diffraction peaks and the standard

$ZnAl_2O_4$ card indicates the formation of the spinel solid solution phase without any impurities. With the increase in the substitution content of [Mg^{2+}-Ge^{4+}], the cell parameters $a = b = c$, cell volume V, and M-O (M = Al/Mg/Ge/Cr) average bond length of the MO_6 octahedra show a linear increase as shown in Fig. S1a-c, which implies the successful incorporation of Mg^{2+} and Ge^{4+}. As discussed previously, the expansion of the unit cell caused by the incorporation of [Mg^{2+}-Ge^{4+}] to replace [Al^{3+}-Al^{3+}] is due to the larger ionic radii of the Mg^{2+}-Ge^{4+} pair, which leads to the diffraction peaks shifting to the lower angle side (Fig. 1a). It has been reported that $ZnAl_2O_4$ is a near normal spinel structure without cation disorder [19, 38]. In other words, Zn^{2+} completely occupies the tetrahedral site, while Al^{3+} occupies the octahedral site in the pure $ZnAl_2O_4$ host. When the doping ion pair Mg^{2+}-Ge^{4+} is introduced, the co-substitution of Mg^{2+}/Ge^{4+} for Al^{3+} plays the dominant role due to the presence of many octahedral vacancies in the case of Zn/(Mg/Al/Ge)=0.5. On the one hand, considering the matching degree of the cation radius and valence states, it is assumed that Mg^{2+} mainly occupies the Al^{3+} site (octahedral site) and slightly occupies the Zn^{2+} site (tetrahedral site) accompanied by an equal amount of Zn^{2+} occupying the Al^{3+} site. On the other hand, the significant differences in ionic radii and valence states between Ge^{4+} (r = 0.39 Å, CN = 4) and Zn^{2+} (r = 0.60 Å, CN = 4) make Ge^{4+} entirely occupy the Al^{3+} site. The cation lattice occupancy has been refined, and the refined results are summarized in Table 2 and Table S2-5. Interestingly, with an increase in x, the occupation of Mg^{2+} in the tetrahedral site changes from 0.018 (x = 0.2) to 0.071 (x = 0.4), but with a further increase in the Mg^{2+} concentration, the occupation for x = 0.6 sample only increases slightly. This phenomenon shows that in the case of a high concentration of Mg^{2+}, $Mg_{Al}^{'}$ rather than $Zn_{Al}^{'}$ is the main defect component. Meanwhile, the substitution of the larger [MgO_6] and the smaller [GeO_6] polyhedra for [AlO_6] polyhedra could lead to local structural distortion and bond distance variation [29, 30].

The distortion of ZAMG:Cr^{3+} (x = 0-0.6) was further characterized by Raman spectroscopy, as shown in Fig. 2e. According to group theory, the phonon modes of cubic spinel (Fd3m) are predicted as follows: $\Gamma = A_{1g}(R) + E_g(R) + T_{1g} + 3T_{2g}(R) + 2A_{2u}$

+ $2E_u$ + $5T_{1u}$(IR) + $2T_{2u}$, from which the A_{1g}, E_g and $3T_{2g}$ modes are Raman-active, $5T_{1u}$ is IR-active, and the others are acoustic or silent [39, 40]. As a rule, the three strongest Raman bands at ~416, ~656 and ~750 cm^{-1} correspond to the E_g, T_{2g} and A_{1g} modes, respectively. However, it has been reported that the high-frequency band located at 750 cm^{-1} is much weaker than others in the gahnite spectrum [41, 42]. Thus, the observed band peaks at ~416 and ~656 cm^{-1} in the pure $ZnAl_2O_4$ (x = 0) sample are consistent with those for single crystal gahnite reported by Chopelas and Hofmeister [42]. It is widely accepted that the Raman modes of the spinel structure in the range of 300-600 cm^{-1} are assigned to MO_6 octahedra, while the modes in the range of 600-700 cm^{-1} are associated with MO_4 tetrahedra [30, 43, 44]. The result for x = 0 sample indicates that a large number of AlO_6 and ZnO_4 groups with symmetric stretching vibrations exist. Furthermore, with the increase in the x value, the intensities of the peaks at ~416 and ~656 cm^{-1} gradually decrease and shift to lower wavenumbers due to the transformation from symmetric AlO_6 and ZnO_4 groups to distorted AlO_6 and ZnO_4 groups by doping Mg^{2+}/Ge^{4+}. A similar phenomenon without the movement of the T_{2g} (~610 cm^{-1}) mode frequency emerges in the Raman spectra of $ZnGa_{2-x}(Mg/Ge)_xO_4:Cr^{3+}$ [30]. Here, all three Raman frequencies undergo a modest progressive softening passing, particularly the E_g mode, which is greatly related to the increase in cell volume and M-O bond length obtained from the Rietveld refinements [45], as shown in Fig. 2f; this suggests that the octahedra become more distorted and asymmetric with increasing x value, which may influence the crystal field of Cr^{3+}, thus affecting the luminescence property of the ZAMG:Cr^{3+} phosphors. In addition, an intense band with an inflection at ~750 cm^{-1} appears and gradually strengthens, due to the introduction of magnesium and germanium ions in the octahedral positions. Similarly, the Raman spectral activity present at ~720 cm^{-1} and ~780 cm^{-1} is attributed to the replacement of aluminum by titanium and zinc ions in the Ti-doped $ZnAl_2O_4$ [46]. The $ZnAl_2O_4$ spinel crystal structure is shown in Fig. 2g, which has two types of coordination polyhedra with different tetrahedral (ZnO_4 and MgO_4) and octahedral (AlO_6, ZnO_6, MgO_6 and GeO_6) sites based on the co-substitution of Mg^{2+}/Ge^{4+}. Moreover, since the average valence of [Mg^{2+}-Ge^{4+}] is similar to that of Al^{3+}, there is

no additional charge compensating defects. Thus, the opposite charged defect pairs of $Mg_{Al}^{'}$ or $Zn_{Al}^{'}$ and $Ge_{Al}^{\cdot}$ are formed, which provide a local electric field around Cr_{N2}^{3+} [30, 31]. The defect cluster of $Mg_{Al}^{'}$-Cr_{N2}^{3+}-$Ge_{Al}^{\cdot}$ may be used as an effective trap, contributing to the long-persistent luminescence [22, 30].

Table 2 The Rietveld refinement results of the octahedral and tetrahedral sites for the ZAMG:Cr^{3+} (x = 0-0.6) samples.

	Tetrahedral site		Octahedral site			
Sample	Zn^{IV}	Mg^{IV}	Zn^{VI}	Al^{VI}	Mg^{VI}	Ge^{VI}
x = 0	1	-	-	0.9875	-	-
x = 0.2	0.982	0.018	0.018	0.790	0.082	0.100
x = 0.4	0.929	0.071	0.071	0.590	0.129	0.200
x = 0.6	0.926	0.074	0.074	0.390	0.226	0.300

In addition, Mg^{2+}/Ge^{4+}/Al^{3+} may replace Zn^{2+} to form antisite defects due to Mg^{2+}/Ge^{4+} doping, leading to the different defect clusters associated with the traps. To investigate the preferential formation of antisite defects, the formation energy of potential configurations is calculated. A 56-atom unit cell of $ZnAl_2O_4$ containing 8-atom Zn, 16-atom Al, and 32-atom O is built as a model, which is defined as UC-1 in Fig. 3a. To demonstrate the variation in the band gap with increasing Mg^{2+}/Ge^{4+} doping, the model of the 56-atom unit cell of $ZnAl_2O_4$ with one Mg^{2+} and one Ge^{4+} replacing two Al^{3+} is defined as UC-2, while the similar model of $ZnAl_2O_4$ with Mg^{2+}/Ge^{4+} completely replacing Al^{3+} is used as UC-3, as shown in Figs. 3b and c. According to the atomic number ratio of Mg/Ge and Al, the corresponding Mg^{2+}/Ge^{4+} doping concentrations for UC-1, UC-2, and UC-3 crystal structure types are 0 at.%, 12.5 at.%, and 100 at.%, respectively. The exchange of Zn atoms and nearest Al atoms is equivalent in the $ZnAl_2O_4$ host, and the formation energy for Zn and Al in a non-nearby position is too large; thus, one Zn-Al antisite is first built in UC-1. To further study the site preference of ZAMG, 15 possible configurations of antisite in UC-2 are also built. These 15 configurations are established by exchanging the site of Mg, Al, and Ge atoms with one of the surrounding Zn atoms, while some antisite configurations with excessive formation energies are ignored. The formation energies (ΔE_f) are given in Fig. 3d and are calculated as [18, 31]

$$\Delta E_f = E(\text{antisite}) - E(\text{perfect}) \quad (1)$$

where E(perfect) is the total energy of the $ZnAl_2O_4$ host with or without Mg^{2+}/Ge^{4+} doping (UC-1 or UC-2) and E(antisite) is the total energy of the unit cell with either one antisite. The formation energy of the Zn-Al antisite in UC-1 is calculated as 0.96 eV. According to the work of Kashii et al. [38] and Priolkar et al. [19, 20], there is almost no cation disorder in the $ZnAl_2O_4$ spinel structure, which implies that the formation energy of Zn-Al antisite in UC-1 is too large. However, the formation energy of the Zn-Al antisite at certain positions can be reduced to below 0.96 eV in the case of UC-2, indicating that it is possible to form a small amount of Zn-Al antisite due to local structural distortion by Mg^{2+}/Ge^{4+} doping. Meanwhile, the formation energy of the Zn-Mg antisite is only 0.46 eV, while that of the Zn-Ge antisite is approximately 1.34-1.37 eV. These results indicate that Zn-Mg antisite is easily formed, but Zn-Ge antisite hardly exists. The behavior of antisite defect configurations obtained via DFT theoretically proves the correctness of the XRD Rietveld structure refinement results, although a small percentage of Zn-Al antisite is ignored when Mg^{2+}/Ge^{4+} doping occurs. Additionally, these antisite configurations prefer to form more stable antisite pairs rather than isolated antisites [18]. Therefore, Mg^{2+}/Ge^{4+} doping effectively generates more Zn-Mg and a few Zn-Al antisite defects in $ZnAl_2O_4$, leading to the formation of $Mg_{Al}^{'} - Ge_{Al}^{\bullet}$ and $Zn_{Al}^{'} - Ge_{Al}^{\bullet}$ defect clusters. This phenomenon agrees with previous findings of Zhu et al. on the structure evolution in $ZnGa_2O_4$ codoped with Mg^{2+}/Ge^{4+} [30, 31]. The luminescent chromium dopants always preferentially occupy the distorted octahedral site [18]. The insertion of antisite defect clusters provides a severe distortion of the local environment for Cr^{3+}, which influences the emission of Cr^{3+} and contributes to the persistent luminescence. As previously published, the emission intensity of Cr^{3+} can be increased by replacing Mg^{2+} with alkaline-metal atoms (Ca, Sr, Ba) in $Mg_7Ga_2GeO_{12}:Cr^{3+}$ [47], and the afterglow of $ZnGa_2O_4:Cr^{3+}$ can be improved through Sn^{4+} partially replacing Ga^{3+} [48].

3.2. Photoluminescence and persistent luminescence properties

The diffuse reflectance (DR) spectra of the ZAMG:Cr^{3+} (x = 0-0.6) phosphors are shown in Fig. 4a, while the bandgap energies of the samples were estimated from the

DR spectra of ZAMG (Fig. 4b). All the samples have three characteristic absorption bands at 273 nm (near ultraviolet region, $^4A_2 \rightarrow CB$), 387 nm (ultraviolet region, $^4A_2 \rightarrow {}^4T_1$ (^4F)), and 535 nm (visible region, $^4A_2 \rightarrow {}^4T_2$) [49]. Mg^{2+}/Ge^{4+} doping yields enhanced intensity of the absorption bands, indicating that Mg^{2+}/Ge^{4+} doping contributes to the increased absorption of ultraviolet and visible light. A redshift of the latter two bands is found by increasing the Cr^{3+} concentration. The optical bandgap energy (E_g) of the ZAMG (x = 0-0.6) host can be calculated by the Kubelka-Munk formula [50, 51]:

$$F(R)=\frac{K}{S}=\frac{(1-R)^2}{2R} \quad (2)$$

$$[F(R)\times h\nu]^2=A(h\nu-E_g) \quad (3)$$

where K, S, R, A, $h\nu$, and E_g are the molar absorption coefficient, scattering factor, diffuse reflectance, absorption constant, incident photon energy, and bandgap energy, respectively. The calculated E_g of the ZAMG host gradually decreases from 4.15 eV to 4.06 eV along with the increase in the x value, illustrating that Mg^{2+}/Ge^{4+} doping results in a narrower bandgap. To investigate the change in the electronic band structure of $ZnAl_2O_4$ and $ZnAl_2O_4$ with low and high concentrations of Mg^{2+}/Ge^{4+} doping, the total and partial density of states (DOS) of UC-1, UC-2, and UC-3 (Fig. 3a-c) are calculated by density functional theory and plotted in Fig. 4c-e. For $ZnAl_2O_4$ in Fig. 4c, the valence band (VB) in the lower part is mainly composed of the hybridization of Zn 3d, Al 3s, Al 3p, and O 2p states, while the conduction band (CB) in the upper part has major contributions from Al 3s and Al 3p states. The composition of the electronic structure of $ZnAl_2O_4$ after Mg^{2+}/Ge^{4+} doping still originates predominantly from the states of Al, Zn, and O, as shown in Fig. 4d. As the concentration of Mg^{2+}/Ge^{4+} increases until Al^{3+} is completely replaced, the CB and VB are affected by the states of Ge (Fig. 4e), resulting in significant changes in the band gap. The calculated band gaps for UC-1, UC-2, and UC-3 are 3.82, 3.50, and 2.48 eV, respectively, which are close to that reported earlier of 3.8-3.9 eV [52, 53]. However, the calculated values are always smaller than the values measured from the optical reflectivity experiment since the standard DFT exchange-correlation function greatly underestimates the size of the band

gap [37]. Above all, the band gaps calculated by DFT-GGA are in good agreement with the experimental values from the UV−vis analysis. All of the results demonstrate that the band gap decreases with increasing Mg^{2+}/Ge^{4+} doping.

Fig. 5 shows the photoluminescence excitation (PLE) and emission (PL) spectra of the ZAMG:Cr^{3+} samples (x = 0-0.6) at room temperature. The PLE spectra monitored at 686 nm contain two strong excitation bands centered at 387 nm and 530 nm, which are attributed to the $^4A_2 \rightarrow {}^4T_1$ (^4F) and $^4A_2 \rightarrow {}^4T_2$ transitions of Cr^{3+} ions (Fig. 5a) [22, 54]. Moreover, the asymmetric broad band at 394 nm can be regarded as the overlap of two bands at 390 nm and 414 nm. These two peaks originate from the energy level splitting in the trigonal crystal field and under the spin-orbit effect and correspond to $^4A_2(^4F) \rightarrow {}^4E(^4T_1(^4F))$ and $^4A_2(^4F) \rightarrow {}^4A_2(^4T_1(^4F))$ transitions [32, 55]. The band at approximately 252 nm ascribed to the transition of $^4A_2 \rightarrow$CB shifts to lower energy with increasing x, which is consistent with the reduction in the band gap of ZAMG (x = 0-0.6) [23, 24, 56]. It is worth noting that the peaks of the PLE spectra exhibit an obvious redshift with increasing x value. This shift can be ascribed to the weakening of the crystal field with increasing Mg^{2+}/Ge^{4+} co-doping [27]. The dominating emission lines at 686 nm in the PL spectra for all samples are related to the spin-forbidden $^2E \rightarrow {}^4A_2$ transition of Cr^{3+} in the octahedral crystal field under excitation at 530 nm or 387 nm (Figs. 5b and c). The zero phonon R lines at 686 nm are associated with Cr^{3+} in undistorted octahedral sites, while the N1 (~689 nm) and N2 (~694 nm) lines correspond to Cr^{3+} neighboring one certain defect [19, 20]. As previously reported, the N1 line may correspond to Cr^{3+} close to $Zn_{Al}^{'}$ and $Ge_{Al}^{\cdot}$ antisite defects (referred to as Cr_{N1}), and the N2 line is assigned to Cr^{3+} adjoining $Mg_{Al}^{'}$ and $Ge_{Al}^{\cdot}$ antisite defects as the first cationic neighbor (Cr_{N2}) [19, 22, 30]. However, the N1 and N2 lines are too low to detect for the x = 0 sample, which is due to the lack of intrinsic antisite defects ($Zn_{Al}^{'}$ and $Al_{Zn}^{\cdot}$) [19, 20]. The R lines are always accompanied by the Stokes phonon side bands (PSB, 706-721 nm) and anti-Stokes PSB (648-683 nm). Remarkably, the relative intensity of the R line becomes weaker than that of the N1 and N2 lines with an incremental substitution of Mg^{2+}-Ge^{4+}, and the latter emerges as a dominating influence in the emission spectra, as shown in Fig. 5d. Another interesting finding is

that the emission band of the $^2E \rightarrow {}^4A_2$ transition becomes broader than that of the sample without Mg^{2+}-Ge^{4+} co-doping. The FWHM of the emission band increases from 34 nm to 79 nm with an increase in *x* (Fig. S2 and Fig. 5d). This phenomenon can be interpreted to arise from the increasing disorder of Cr^{3+} ions induced by Mg^{2+}-Ge^{4+} incorporation [22]. In addition, the peak at approximately 704 nm (denoted by N4) is assigned to Cr^{3+}-Cr^{3+} pairs in the samples with sufficiently high Cr^{3+} concentrations accompanied by its phonon-sidebands in the range of 727-750 nm [32]. The results of Zhang et al. [32] and Jia et al. [33] suggested the presence of coupling Cr-Cr pairs in the spinel lattice when the Cr^{3+} ion concentration was above 0.5% through high-resolution XPS spectra of Cr 2p and EPR.

To further elucidate the luminescence mechanism of Cr^{3+}, the high-resolution PLE and PL spectra of the ZAMG:Cr^{3+} samples were obtained at 77 K. From the PLE and the normalized PLE spectra in Figs. 6a and c, there is a distinct redshift from 527 nm to 545 nm as the *x* value increases from 0 to 0.6. The luminescence of Cr^{3+} is easily affected by the crystal field environment; as a result, the redshift of PLE may be related to the change in the crystal field and nephelauxetic effect caused by Mg^{2+}-Ge^{4+} co-doping. The crystal field intensity Dq/B is determined by using the following formula [14]:

$$\Delta E = E\ (^4A_2 \rightarrow {}^4T_1) - E\ (^4A_2 \rightarrow {}^4T_2) \quad (4)$$

$$\Delta S = E\ (^4A_2 \rightarrow {}^4T_2) - E\ (^4T_2 \rightarrow {}^4A_2) \quad (5)$$

$$10 \times D_q = E\ (^4A_2 \rightarrow {}^4T_2) - \Delta S/2 \quad (6)$$

$$\frac{Dq}{B} = \frac{15(x\text{-}8)}{x^2\text{-}10x} \quad (7)$$

$$x = \frac{\Delta E}{Dq} \quad (8)$$

where Dq is the crystal field parameter and B is the Racah electron repulsion parameter. According to Figs. 6a and b, the values of ΔE (the energy difference between $^4A_2 \rightarrow {}^4T_1$ and $^4A_2 \rightarrow {}^4T_2$), ΔS (the Stokes shift), and Dq/B are calculated and summarized in Table 3. The calculated value of Dq/B for the $x = 0$ sample is 2.42, reflecting that Cr^{3+} ions are in a strong crystal field. By comparison, the values of Dq/B for $x = 0.1$, 0.2, 0.3, 0.4, 0.5, and 0.6 are relatively low, which implies that the crystal field of Cr^{3+}

becomes weaker at a higher Mg^{2+}/Ge^{4+} concentration. The weakening crystal field of Cr^{3+} in ZAMG is presented with the help of the Tanabe-Sugano diagram (Fig. S3). It is well known that Cr^{3+} generates narrowband emission (~700 nm) due to $^2E \rightarrow {}^4A_2$ in the high field (Dq/B>2.3), while Cr^{3+} exhibits broadband emission (650-1600 nm) arising from $^4T_2 \rightarrow {}^4A_2$ in the low field (Dq/B<2.3). Among previous reports, the $^2E \rightarrow {}^4A_2$ and $^4T_2 \rightarrow {}^4A_2$ luminescence transitions occurred simultaneously in Cr^{3+}-doped gallogermanate with an intermediate crystal field [25, 26]. By comparing the measured band shapes with those given in the references [25, 26], the broad emission at approximately 720 nm can be assigned to the $^4T_2 \rightarrow {}^4A_2$ transition. The PL intensity of the $^4T_2 \rightarrow {}^4A_2$ transition increases with increasing x values at RT and 77 K because the weaker the crystal field is, the higher the transition probability of the $^4T_2 \rightarrow {}^4A_2$ transition. In addition, the PL intensity ratios of the as-measured N1/R and N2/R lines as a function of x are shown in Fig. 6d. The R line of the ZAMG:Cr^{3+} sample (x = 0) is strong, while the N1 and N2 lines can be ignored. With the increase in x, the N1 and N2 lines become stronger and wider, and in the case of higher x values, the N2 line gradually dominates. This phenomenon indicates that the antisite defect clusters $Zn_{Al}^{'}$-Cr^{3+}-$Ge_{Al}^{\cdot}$ and $Mg_{Al}^{'}$-Cr^{3+}-$Ge_{Al}^{\cdot}$ significantly increase due to the incorporation of Mg^{2+}-Ge^{4+}, which would enhance the inversion disorder of the host [19, 20, 57]. Generally, the resulting defect clusters and increasing disorder remarkably improve the persistent luminescence.

Table 3 Crystal field parameters of ZAMG:Cr^{3+} samples (x = 0-0.6) at 77 K.

Sample	$E(^4A_2 \rightarrow {}^4T_1)$ (cm^{-1})	$E(^4A_2 \rightarrow {}^4T_2)$ (cm^{-1})	$E(^4T_2 \rightarrow {}^4A_2)$ (cm^{-1})	ΔE (cm^{-1})	ΔS (cm^{-1})	Dq	B	Dq/B
x = 0	25840	18975	14556	6864	4419	1677	692	2.42
x = 0.1	25840	18939	14556	6900	4383	1675	697	2.40
x = 0.2	25840	18832	14556	7007	4276	1669	713	2.34
x = 0.3	25773	18762	14556	7011	4206	1666	714	2.33
x = 0.4	25641	18553	14556	7088	3997	1655	727	2.28
x = 0.5	25575	18416	14556	7159	3860	1649	738	2.23
x = 0.6	25510	18349	14556	7162	3793	1645	739	2.22

In addition to the broad NIR photoluminescence, intense and long persistent NIR luminescence can be observed from the high levels of the Mg^{2+}-Ge^{4+} substituted

samples after removal of the excitation source. Fig. 7a shows the NIR afterglow decay time and persistent luminescence curves of the ZAMG:Cr^{3+} samples (x = 0-0.6) monitored at 686 nm after irradiation by UV light for 10 min. After 1500 s of decay, the persistent luminescence intensity remains 10 times that of the background for the sample with x = 0.4. This result indicates that the NIR afterglow of ZAMG:Cr^{3+} samples (x = 0.4-0.6) can last much longer than 1500 s. The Mg^{2+}-Ge^{4+} co-doping can significantly improve the afterglow performance of ZAO:Cr^{3+}, and with increasing Mg^{2+}-Ge^{4+} concentration, the afterglow intensity and decay time of ZAMG:Cr^{3+} increase. The long persistent NIR afterglow of ZAMG:Cr^{3+} (x = 0.4-0.6) phosphors is further confirmed by a night vision device, as shown in Fig. 7b. The x = 0.6 sample exhibits the best persistent NIR luminescence, which can last longer than 30 min. To further elucidate the variation in the trap after Mg^{2+}-Ge^{4+} substitution, the thermoluminescence (TL) spectra of the ZAMG:Cr^{3+} samples (x = 0.1-0.6) were obtained, as shown in Fig. 7c. Both the shape and the maximum temperature of the TL glow curves are significantly affected by increasing Mg^{2+}-Ge^{4+} content (Fig. S4). Apparently, with increasing Mg^{2+}-Ge^{4+} content, the entire glow curves progressively shift toward lower temperatures, except for x = 0; this may indicate that the trap depth can become shallow, resulting in a lower thermal energy needed to release the trapped charges and thus a longer afterglow. The trap depths were evaluated by the following general order kinetic equation [58, 59]:

$$I(T)=sn_0 \exp\left\{-\frac{E_t}{kT}\right\} \times \left[\frac{(b\text{-}1)s}{\beta}\int_{T_0}^{T} \exp\left\{-\frac{E_t}{kT}\right\} dT+1\right]^{-\frac{b}{(b\text{-}1)}} \quad (9)$$

where s is the frequency factor, n_0 is the initial number of trapped electrons after irradiation, E_t is the trap depth, k is Boltzmann's constant, β is the heating rate (1 K/s for this experiment), b is the kinetic order, and T is the absolute temperature. Considering that there are three possible defects in ZAMG:Cr^{3+}, resulting in close but different trap levels, three trap components have been added to fit these asymmetric glow curves. According to this general order kinetic equation, the accumulation peak of the fit curve (red line) agrees with the experimental data (black line), as shown in Fig. 7c. The trap depth E_t and initial number of trapped electrons n_0 of the three trap

components are listed in Table 4, and the main fitting parameters are summarized in Table S6. The fitted data of kinetic order *b* for all samples are in the range of 1~2, which could suggest that the kinetic processes are not pure first-order or second-order, but rather general order kinetic processes. Based on the general order kinetic equation, three traps with trap depths E_t of ~0.8 eV, ~0.7 eV, and ~0.5 eV are obtained. When the Mg^{2+}-Ge^{4+} content contains a low level, the initial number of trapped electrons n_0 of trap 1 is high, indicating that it corresponds to a large number of certain defects. It seems probable that trap 1 is related to the reported intrinsic defects in $ZnAl_2O_4$, such as V_O^+ and V_O^{2+} [60]. With increasing Mg^{2+}-Ge^{4+} co-doping concentration, the n_0 of trap 2 first increases and then decreases. Trap 2 is more likely to correspond to $Al_{Zn}^{\cdot}$ defects caused by Zn-Al antisites, as the number of such defects does not always increase but remains at a certain level at high Mg^{2+}-Ge^{4+} concentrations. Notably, the proportion of n_0 of trap 3 in that of the three traps gradually increases as the *x* value increases. Trap 3 may be attributed to the major $Ge_{Al}^{\cdot}$ defects formed by Mg^{2+}-Ge^{4+} co-doping. This significantly improves the probability of carrier capture by the $Ge_{Al}^{\cdot}$ defects related to trap 3 due to its shallower trap depth E_t; it can enhance the afterglow level and reduce the photoluminescence intensity of ZAMG:Cr^{3+} phosphors [61]. At the same time, the E_t of all three traps slowly decreases with increasing *x* from 0 to 0.6, possibly due to a decrease in the band gap. According to the above results, the mechanism diagram of luminescence and afterglow for ZAMG:Cr^{3+} phosphors is presented in Fig. 7d. For *x* = 0 samples, the electrons of Cr^{3+} in ZAO:Cr^{3+} are pumped from the ground state level $^4A_{2g}$ to the excited state levels $^4T_{2g}$, $^4T_{1g}$, and conduction band (CB), then transferred to the ^2E_g level *via* non-radiative relaxation, and finally returned back to the $^4A_{2g}$ level, which has a good NIR light output. The content of the defects associated with trap 1 in ZAO:Cr^{3+} is very low and has no ability to trap electrons, so the ZAO:Cr^{3+} phosphor exhibits no afterglow. For other samples, a portion of the electrons is trapped by trap2 and trap3 *via* CB after excitation to CB. When irradiation is stopped, the recombination of the de-trapping electrons occurs *via* CB or through a thermal tunneling process. Meanwhile, the PLE spectra exhibit a distinct redshift with an increased *x* value. This phenomenon can be explained by using the Tanabe-Sugano energy-level diagram (Fig.

S3), which proves that the existence of broad NIR emission corresponds to the $^4T_2 \rightarrow {}^4A_2$ transition in the ZAMG:Cr^{3+} (x = 0.6) phosphor.

Table 4 Fitting results of TL curves of ZAMG:Cr^{3+} samples (x = 0.1-0.6).

Sample	Trap1		Trap2		Trap3		Proportion of trap 3
	E_t (eV)	n_0	E_t (eV)	n_0	E_t (eV)	n_0	
x = 0.1	0.87	6.47×10^5	0.73	1.50×10^5	0.57	2.71×10^4	3.29%
x = 0.2	0.84	4.24×10^5	0.69	8.81×10^5	0.54	2.10×10^5	13.88%
x = 0.3	0.83	1.28×10^5	0.68	7.63×10^5	0.53	5.01×10^5	35.99%
x = 0.4	0.82	1.33×10^5	0.67	3.16×10^5	0.52	7.29×10^5	61.86%
x = 0.5	0.80	4.48×10^4	0.66	1.55×10^5	0.52	9.06×10^5	81.93%
x = 0.6	0.80	3.25×10^4	0.65	1.15×10^5	0.51	7.12×10^5	82.82%

To further broaden the PL emission of ZAMG:Cr^{3+}, the concentration of Cr^{3+} was increased when fixing the Mg^{2+}-Ge^{4+} concentration to increase the Cr^{3+} at the distorted sites. The normalized PLE and PL spectra of ZAO:Cr^{3+} (y = 1-2) and ZA(MG)$_{0.4}$:Cr^{3+} (z = 1-2) are displayed in Fig. S5, Figs. 8a and b. When the Cr^{3+} concentration increases from 1 at.% to 2 at.%, the intensity of the PL spectra ranging from 730 to 750 nm shows a continuous increase. By referring to the previous results [32,33], it can be seen that the emission of N4 (704 nm) and its phonon-sidebands (727-750 nm) should result from the interaction between Cr-Cr pairs. On the one hand, the emission bands at 704 nm and 727-750 nm corresponding to N4 and its PSB become broader with the increase in the concentration of Cr^{3+} for ZAO:Cr^{3+} (y = 1-2). This phenomenon may have resulted from the increase in the Cr^{3+}-Cr^{3+} pairs [32]. On the other hand, the PL emission peaks further become the connected band as the Cr^{3+} concentration increases for ZA(MG)$_{0.4}$:Cr^{3+} (z = 1-2), which can be caused by some possible reasons. First, the peaks at N1 (~689 nm) and N2 (~694 nm) broaden due to the appearance of Cr^{3+} neighboring the antisite defect clusters of $Zn_{Al}^{'}$-Cr^{3+}-$Ge_{Al}^{\cdot}$ and $Mg_{Al}^{'}$-Cr^{3+}-$Ge_{Al}^{\cdot}$ with the [Mg^{2+}-Ge^{4+}] unit replacing the [Al^{3+}-Al^{3+}] unit. Subsequently, the addition of Cr^{3+} may not only form Cr^{3+}-Cr^{3+} pairs, but also significantly increase the probability of adjacent antisite defect clusters of Cr^{3+}, thus widening N4 and the PSB of the N4. Then, the broadened emission at 720-800 nm assigned to the $^4T_2 \rightarrow {}^4A_2$ transition is due to the

weakened crystal field strength caused by Mg^{2+}-Ge^{4+} substitution [25, 26]. In conclusion, the broad-band emission of $ZA(MG)_{0.4}:Cr^{3+}$ can be comprehensively ascribed to the substitution-induced and high content Cr^{3+} causing an increase in Cr^{3+} at distorted sites. As shown in Fig. S6 and Fig. 8c, the FWHM of the overall emission of $ZA(MG)_{0.4}:Cr^{3+}$ changes from 44 nm to 95 nm.

The luminescence thermal stability is vital to assess the practicability of pc-LED devices since the junction temperature is usually above 388 K. Thus, the temperature-dependent PL spectra of $ZAMG:Cr^{3+}$ (x = 0.2, 0.4) and $ZA(MG)_{0.4}:Cr^{3+}$ (z = 2) phosphors under excitation at 394 nm were measured from 298 K to 573 K, as depicted in Fig. S7 and Fig. 8d. Due to the thermal quenching effect, the PL intensity of the $ZAMG:Cr^{3+}$ (x = 0.2, 0.4) phosphors decreases at higher heating temperatures. A special point to note is that the emission intensity of $ZA(MG)_{0.4}:Cr^{3+}$ (z = 2) at the R line (686 nm) is slightly greater than 100% in the temperature range of 323-398 K and then gradually decreases with a further increase in temperature, which proves the satisfactory thermal stability of this phosphor. Such a negative thermal quenching phenomenon can be attributed to the direct energy transfer from the defect states and the high efficiency of capturing carriers for the trap centers [62, 63]. The thermal ionization of Cr^{3+} 3d electrons entering the CB of the host could be partially compensated by the captured electrons detrapped from the shallow trap state at high temperature, which results in enhanced thermal stability. In addition, the multi-phonon relaxation caused by lattice vibration is the main reason for the decrease in the PL intensity at high temperatures [6]. To assess the thermal quenching behavior, the activation energy (E_a) was analyzed based on the Arrhenius equation [64]:

$$I_K = \frac{I_0}{1 + A\exp(-\frac{\Delta E_a}{kT})} \tag{10}$$

where I_K and I_0 represent the PL intensity at the given temperature and 298 K, respectively. A is the constant related to the host, and k stands for the Boltzmann constant (8.629×10^{-5} eV). The value of E_a could be obtained by linear fitting of $\mathrm{Ln}(I_0/I_K\text{-}1)$ *vs.* $1/kT$. The E_a values of the $ZAMG:Cr^{3+}$ (x = 0.2, 0.4) and $ZA(MG)_{0.4}:Cr^{3+}$ (z = 2) phosphors are determined to be 0.216, 0.238, and 0.453 eV (Fig. S8 and Fig. 8e),

which is consistent with the higher quenching temperature of luminescence of the latter. As shown in Fig. 8f, the $ZA(MG)_{0.4}:Cr^{3+}$ (z = 2) sample shows a better thermal stability compared with the other two samples, and the integral PL intensity at 398 K can maintain 101% of the initial intensity at 298 K. For the $ZA(MG)_{0.4}:Cr^{3+}$ (z = 2) sample, the probability that electrons trapped in shallow traps tunnel into the Cr^{3+} center and recombine with holes increases, due to the high content of Cr^{3+} [62]; this may be the reason why only the $ZA(MG)_{0.4}:Cr^{3+}$ (z = 2) sample exhibits a negative thermal quenching phenomenon. This result indicates that the $ZA(MG)_{0.4}:Cr^{3+}$ (z = 2) phosphor is more suitable for pc-LEDs.

3.3. Application for the NIR pc-LED device

A NIR pc-LED device was constructed by combining the optimized $ZA(MG)_{0.4}:Cr^{3+}$ (z = 2) phosphor with a 395 nm ultraviolet LED chip. Fig. 9a depicts the electroluminescence (EL) spectra of the prepared pc-LED under various driving currents, and the insets show the images of pc-LED in both current on and off states. With the rise of the driving currents from 10 to 60 mA, the emission intensity gradually increases. The NIR output power of the fabricated devices is 19 mW at an input current of 100 mA with an electro-optical conversion efficiency of 7.7%. Due to more Cr^{3+} located in distorted sites in $ZA(MG)_{0.4}:Cr^{3+}$ (z = 2), the as-prepared NIR pc-LED has broadband emission that can cover the NIR-Ⅰ region from 700 to 900 nm. By utilizing the remarkable penetration ability of NIR light, non-destructive detection can be conducted on fruits, such as apples, to detect internal bruises caused by collision or extrusion during packaging and transportation (Fig. 9b). Using a fluorescent lamp as the light source, the printed words of all colors can be observed under a visible camera. However, only words with deep colors (deep red, blue, green, etc.) can be clearly detected by the NIR camera using the light source of the fabricated NIR pc-LED (Fig. 9c). Depending on this property, the NIR pc-LED can be applied as a lighting source for information encryption with the help of an NIR camera. For example, the barcodes representing “19230419” and “20230419” are printed in red and black words, respectively, and can be detected with different results under different light sources and cameras, as shown in Fig. 9d. Both types of barcodes and their overlapping information

can be clearly displayed under white light irradiation. The black barcode represents true information, while the red barcode indicates false information. The true information can be identified via the NIR camera under NIR pc-LED irradiation because black ink exhibits stronger absorption in the NIR than other colors. These phenomena strongly demonstrate the application prospects of the ZAMG:Cr^{3+} phosphor as an NIR pc-LEDs light source in non-destructive testing and anti-counterfeiting.

4. Conclusion

We developed a series of $ZnAl_{1.975-2x}Mg_xGe_xO_4$:1.25 at.% Cr^{3+} (ZAMG:Cr^{3+}, x = 0-0.7), $ZnAl_{2-0.02y}O_4$:y at.%Cr^{3+} (ZAO:Cr^{3+}, y = 1-2), and $ZnAl_{1.2-0.02z}Mg_{0.4}Ge_{0.4}O_4$:$z$ at.%Cr^{3+} (ZA$(MG)_{0.4}$:Cr^{3+}, z = 1-2) samples using high-temperature solid-state reaction. Substituting Mg^{2+}-Ge^{4+} for Al^{3+}-Al^{3+} contributes to the formation of distorted octahedral defect clusters of $Zn_{Al}^{'}$-Cr^{3+}-$Ge_{Al}^{\cdot}$ and $Mg_{Al}^{'}$-Cr^{3+}-$Ge_{Al}^{\cdot}$, which enhances the NIR emission intensity at the N1 and N2 lines and achieves long-lasting NIR persistent luminescence for ZAMG:Cr^{3+} phosphors. Moreover, the redshift of the excitation band and the simultaneous emission from the $^2E \rightarrow {}^4A_2$ and $^4T_2 \rightarrow {}^4A_2$ transitions are both due to the variation in crystal field strength by substitution. The introduced positive charged defects $Al_{Zn}^{\cdot}$ and $Ge_{Al}^{\cdot}$ serve as shallow traps, which can efficiently store and release excited electrons after radiation to obtain a long afterglow duration and negative thermal quenching. On the basis of co-substitution of [Mg^{2+}-Ge^{4+}], we further improved the concentration of Cr^{3+} ions. The high content of Cr^{3+} causes the formation of Cr^{3+}-Cr^{3+} pairs and a higher probability of adjoining antisite defects, which leads to a never-before-reported continuous broadband NIR emission of Cr^{3+}. By using this comprehensive strategy, the FWHM of the emission band was ultimately modulated from 34 nm (for $ZnAl_{1.975}O_4$:1.25 at.% Cr^{3+}) to 95 nm (for $ZnAl_{1.16}Mg_{0.4}Ge_{0.4}O_4$:2 at.% Cr^{3+}), in the absence of emission intensity loss in the range of 685-750 nm. We demonstrated that the NIR pc-LED prepared using the ZA$(MG)_{0.4}$:Cr^{3+} (z = 2) phosphor has a potential application in non-destructive analysis and anti-counterfeiting.

Declaration of competing interest

The authors declare that they have no known competing financial interests or personal relationships that could have appeared to influence the work reported in this paper.

Acknowledgements

This work was supported in part by the Fundamental Research Funds for the Central Universities (Grant N2302004), and National Natural Science Foundation of China (Grant 52371057, U21A2045, 52172112).

References

[1] F.Q. He, E.H. Song, Y.Y. Zhou, H. Ming, Z.T. Chen, J.C. Wu, P.S. Shao, X.F. Yang, Z.G. Xia, Q.Y. Zhang, A general ammonium salt assisted synthesis strategy for Cr^{3+}-doped hexafluorides with highly efficient near infrared emissions, Adv. Funct. Mater. 31 (36) (2021) 2103743. https://doi.org/10.1002/adfm.202103743.

[2] Y. Yan, M.M. Shang, S. Huang, Y.N. Wang, Y.X. Sun, P.P. Dang, J. Lin, Photoluminescence properties of $AScSi_2O_6:Cr^{3+}$ (A = Na and Li) phosphors with high efficiency and thermal stability for near-infrared phosphor-converted light-emitting diode light sources, ACS Appl. Mater. Inter. 14 (6) (2022) 8179-8190. https://doi.org/10.1021/acsami.1c23940.

[3] X.K. Zou, X.J. Wang, H.R. Zhang, Y.Y. Kang, X. Yang, X.J. Zhang, M.S. Molokeev, B.F. Lei, A highly efficient and suitable spectral profile Cr^{3+}-doped garnet near-infrared emitting phosphor for regulating photomorphogenesis of plants, Chem. Eng. J. 428 (2022) 132003. https://doi.org/10.1016/j.cej.2021.132003.

[4] W.T. Huang, C.L. Cheng, Z. Bao, C.W. Yang, K.M. Lu, C.Y. Kang, C.M. Lin, R.S. Liu, Broadband Cr^{3+}, Sn^{4+}-doped oxide nanophosphors for infrared mini light-emitting diodes, Angew. Chem. Int. Ed. 58 (7) (2019) 2069-2072. https://doi.org/10.1002/anie.201813340.

[5] V. Rajendran, W.T. Huang, K.C. Chen, H. Chang, R.S. Liu, Energy-saving chromium-activated garnet-structured phosphor-converted near-infrared light-emitting

diodes, J. Mater. Chem. C 10 (39) (2022) 14367-14378. https://doi.org/10.1039/D2TC02817D.

[6] Z.H. Zhou, F.Q. He, E.H. Song, S. Zhang, X.D. Yi, H. Zhang, Y.K. Le, S. Ye, S.H. Xu, J.R. Qiu, G.P. Dong, Broadband and multimode near-infrared emitter based on Cr^{3+}-activated stannate for multifunctional applications, Adv. Optical Mater. 11 (7) (2023) 2202466. https://doi.org/10.1002/adom.202202466.

[7] S. Huang, Y. Yan, M.M. Shang, Y.N. Wang, Y.X. Sun, P.P. Dang, J. Lin, Super broadband near-infrared solid solution phosphors with adjustable peak wavelengths from 1165 to 875 nm for NIR spectroscopy applications, Adv. Optical Mater. 11 (5) (2022) 2202291. https://doi.org/10.1002/adom.202202291.

[8] Z.B. Tang, F. Du, H. Liu, Z.H. Leng, X.Q. Sun, H.D. Xie, M.D. Que, Y.H. Wang, Eu^{2+}-doped layered double borate phosphor with ultrawide near-infrared spectral distribution in response to ultraviolet-blue light excitation, Adv. Optical Mater. 10 (5) (2022) 2102204. https://doi.org/10.1002/adom.202102204.

[9] F.Y. Zhao, Z. Song, Q.L. Liu, Advances in chromium-activated phosphors for near-infrared light sources, Laser Photon. Rev. 16 (11) (2022) 2200380. https://doi.org/10.1002/lpor.202200380.

[10] E.H. Song, X.X. Jiang, Y.Y. Zhou, Z.S. Lin, S. Ye, Z.G. Xia, Q.Y. Zhang, Heavy Mn^{2+} doped $MgAl_2O_4$ phosphor for high-efficient near-infrared light-emitting diode and the night-vision application, Adv. Optical Mater. 7 (24) (2019) 1901105. https://doi.org/10.1002/adom.201901105.

[11] X.X. Xu, Q.Y. Shao, L.Q. Yao, Y. Dong, J.Q. Jiang, Highly efficient and thermally stable Cr^{3+}-activated silicate phosphors for broadband near-infrared LED applications, Chem. Eng. J. 383 (2020) 123108. https://doi.org/10.1016/j.cej.2019.123108.

[12] M.Q. Mao, T.L. Zhou, H.T. Zeng, L. Wang, F. Huang, X.Y. Tang, R.J. Xie, Broadband near-infrared (NIR) emission realized by the crystal-field engineering of $Y_{3-x}Ca_xAl_{5-x}Si_xO_{12}:Cr^{3+}$ (x = 0-2.0) garnet phosphors, J. Mater. Chem. C 8 (6) (2020) 1981-1988. https://doi.org/10.1039/C9TC05775G.

[13] L.Q. Yao, Q.Y. Shao, M.L. Shi, T.Q. Shang, Y. Dong, C. Liang, J.H. He, J.Q. Jiang, Efficient ultra-broadband $Ga_4GeO_8:Cr^{3+}$ phosphors with tunable peak wavelengths

from 835 to 980 nm for NIR pc-LED application, Adv. Optical Mater. 10 (4) (2022) 2102229. https://doi.org/10.1002/adom.202102229.

[14] C.X. Yuan, R.Y. Li, Y.F. Liu, L.L. Zhang, J.H. Zhang, G. Leniec, P. Sun, Z.H. Liu, Z.H. Luo, R. Dong, J. Jiang, Efficient and broadband $LiGaP_2O_7:Cr^{3+}$ phosphors for smart near-infrared light-emitting diodes, Laser Photon. Rev. 15 (11) (2021) 2100227. https://doi.org/10.1002/lpor.202100227.

[15] M.U. Dumesso, W.G. Xiao, G.J. Zheng, E.T. Basore, M.X. Tang, X.F. Liu, J.R. Qiu, Efficient, stable, and ultra-broadband near-infrared garnet phosphors for miniaturized optical applications, Adv. Optical Mater. 10 (16) (2022) 2200676. https://doi.org/10.1002/adom.202200676.

[16] L.M. Fang, L.L. Zhang, H. Wu, H.J. Wu, G.H. Pan, Z.D. Hao, F. Liu, J.H. Zhang, Efficient broadband near-infrared $CaMgGe_2O_6:Cr^{3+}$ phosphor for pc-LED, Inorg. Chem. 61 (23) (2022) 8815-8822. https://doi.org/10.1021/acs.inorgchem.2c00798.

[17] K.E. Sickafus, J.M. Wills, N.W. Grimes, Structure of spinel, J. Am. Ceram. Soc. 82 (12) (1999) 3279-3292. https://doi.org/10.1111/j.1151-2916.1999.tb02241.x.

[18] A. De Vos, K. Lejaeghere, D.E.P. Vanpoucke, J.J. Joos, P.F. Smet, K. Hemelsoet, First-principles study of antisite defect configurations in $ZnGa_2O_4$:Cr persistent phosphors, Inorg. Chem. 55 (5) (2016) 2402-2412. https://doi.org/10.1021/acs.inorgchem.5b02805.

[19] N. Basavaraju, K.R. Priolkar, D. Gourier, S.K. Sharma, A. Bessière, B. Viana, The importance of inversion disorder in the visible light induced persistent luminescence in Cr^{3+} doped AB_2O_4 (A = Zn or Mg and B = Ga or Al), Phys. Chem. Chem. Phys. 17 (3) (2015) 1790-1799. https://doi.org/10.1039/C4CP03866E.

[20] N. Basavaraju, K.R. Priolkar, D. Gourier, A. Bessière, B. Viana, Order and disorder around Cr^{3+} in chromium doped persistent luminescent AB_2O_4 spinels, Phys. Chem. Chem. Phys. 17 (16) (2015) 10993-10999. https://doi.org/10.1039/C5CP01097G.

[21] X.D. Huang, X.J. Wei, Y. Zeng, L.H. Jing, H.R. Ning, X.D. Sun, Y.Y. Li, D. Li, Y.P. Yi, M.Y. Gao, Turning-on persistent luminescence out of chromium-doped zinc aluminate nanoparticles by instilling antisite defects under mild conditions, Nanoscale 13 (18) (2021) 8514-8523. https://doi.org/10.1039/D0NR08267H.

[22] Y. Zhang, R. Huang, H.L. Li, D.J. Hou, Z.X. Lin, J. Song, Y.Z. Guo, H.H. Lin, C. Song, Z.W. Lin, J. Robertson, Germanium substitution endowing Cr^{3+}-doped zinc aluminate phosphors with bright and super-long near-infrared persistent luminescence, Acta Mater. 155 (2018) 214-221. https://doi.org/10.1016/j.actamat.2018.06.020.

[23] Z.W. Pan, Y.Y. Lu, F. Liu, Sunlight-activated long-persistent luminescence in the near-infrared from Cr^{3+}-doped zinc gallogermanates, Nat. Mater. 11 (2012) 58-63. https://doi.org/10.1038/nmat3173.

[24] T. Maldiney, A. Bessière, J. Seguin, E. Teston, S.K. Sharma, B. Viana, A.J.J. Bos, P. Dorenbos, M. Bessodes, D. Gourier, D. Scherman, C. Richard, The *in vivo* activation of persistent nanophosphors for optical imaging of vascularization, tumours and grafted cells, Nat. Mater. 13 (2014) 418-426. https://doi.org/10.1038/nmat3908.

[25] M. Back, E. Trave, J. Ueda, S. Tanabe, Ratiometric optical thermometer based on dual near-infrared emission in Cr^{3+}-doped bismuth-based gallate host, Chem. Mater. 28 (22) (2016) 8347-8356. https://doi.org/10.1021/acs.chemmater.6b03625.

[26] J. Yang, Y.X. Liu, Y.Y. Zhao, Z. Gong, M. Zhang, D.T. Yan, H.C. Zhu, C.G. Liu, C.S. Xu, H. Zhang, Ratiometric afterglow nanothermometer for simultaneous *in situ* bioimaging and local tissue temperature sensing, Chem. Mater. 29 (19) (2017) 8119-8131. https://doi.org/10.1021/acs.chemmater.7b01958.

[27] Y. Li, Y.Y. Li, R.C. Chen, K. Sharafudeen, S.F. Zhou, M. Gecevicius, H.H. Wang, G.P. Dong, Y.L. Wu, X.X. Qin, J.R. Qiu, Tailoring of the trap distribution and crystal field in Cr^{3+}-doped non-gallate phosphors with near-infrared long-persistence phosphorescence, NPG Asia Mater. 7 (2015) e180. https://doi.org/10.1038/am.2015.38.

[28] Z.F. Pan, V. Castaing, L.P. Yan, L.L. Zhang, C. Zhang, K. Shao, Y.F. Zheng, C.K. Duan, J.H. Liu, C. Richard, B. Viana, Facilitating low-energy activation in the near-infrared persistent luminescent phosphor $Zn_{1+x}Ga_{2-2x}Sn_xO_4:Cr^{3+}$ *via* crystal field strength modulations, J. Phys. Chem. C 124 (15) (2020) 8347-8358. https://doi.org/10.1021/acs.jpcc.0c01951.

[29] S.Y. Li, Q. Zhu, X.D. Sun, J.G. Li, Magical polyhedral twist *via* chemical unit co-substitution in $LaAlO_3:Mn^{4+}$ to greatly enhance the zero phonon line for high-efficiency plant-growth LEDs, J. Mater. Chem. C 9 (22) (2021) 7163-7173.

https://doi.org/10.1039/D1TC01116B.

[30] Q. Zhu, J.Q. Xiahou, X.D. Li, X.D. Sun, J.G. Li, Defect cluster engineering in $ZnGa_{2-x}(Mg/Ge)_xO_4:Cr^{3+}$ nanoparticles for remarkably improved NIR persistent luminescence, J. Am. Ceram. Soc. 104 (9) (2021) 4594-4605. https://doi.org/10.1111/jace.17864.

[31] J.Q. Xiahou, Q. Zhu, L. Zhu, S.Y. Li, J.G. Li, Local structure regulation in near-infrared persistent phosphor of $ZnGa_2O_4:Cr^{3+}$ to fabricate natural-light rechargeable optical thermometer, ACS Appl. Electron. Mater. 3 (9) (2021) 3789-3803. https://doi.org/10.1021/acsaelm.1c00305.

[32] D. Zhang, Q.J. Guo, Y.F. Ren, C.Z. Wang, Q. Shi, Q.L. Wang, X. Xiao, W.J. Wang, Q.L. Fan, Influence of inversion defects and Cr-Cr pairs on the photoluminescent performance of $ZnAl_2O_4$ crystals, J Sol-Gel Sci Technol 85 (2018) 121-131. https://doi.org/10.1007/s10971-017-4527-4.

[33] Z.W. Jia, C.X. Yuan, Y.F. Liu, X.J. Wang, P. Sun, L. Wang, H.C. Jiang, J. Jiang, Strategies to approach high performance in Cr^{3+}-doped phosphors for high-power NIR-LED light sources, Light Sci. Appl. 9 (2020) 86. https://doi.org/10.1038/s41377-020-0326-8.

[34] P.E. Blöchl, Projector augmented-wave method, Phys. Rev. B 50 (24) (1994) 17953. https://doi.org/10.1103/PhysRevB.50.17953.

[35] G. Kresse, J. Furthmüller, Efficient iterative schemes for *ab initio* total-energy calculations using a plane-wave basis set, Phys. Rev. B 54 (16) (1996) 11169. https://doi.org/10.1103/PhysRevB.54.11169.

[36] G. Kresse, J. Furthmüller, Efficiency of ab-initio total energy calculations for metals and semiconductors using a plane-wave basis set, Comp. Mater. Sci. 6 (1) (1996) 15-50. https://doi.org/10.1016/0927-0256(96)00008-0.

[37] J.P. Perdew, K. Burke, M. Ernzerhof, Generalized gradient approximation made simple, Phys. Rev. Lett. 77 (18) (1996) 3865. https://doi.org/10.1103/PhysRevLett.77.3865.

[38] N. Kashii, H. Maekawa, Y. Hinatsu, Dynamics of the cation mixing of $MgAl_2O_4$ and $ZnAl_2O_4$ spinel, J. Am. Ceram. Soc. 82 (7) (1999) 1844-

1848. https://doi.org/10.1111/j.1151-2916.1999.tb02007.x.

[39] W.B. White, B.A. DeAngelis, Interpretation of the vibrational spectra of spinels, Spectrochim. Acta A 23 (4) (1967) 985-995. https://doi.org/10.1016/0584-8539(67)80023-0.

[40] P. Loiko, A. Belyaev, O. Dymshits, I. Evdokimov, V. Vitkin, K. Volkova, M. Tsenter, A. Volokitina, M. Baranov, E. Vilejshikova, A. Baranov, A. Zhilin, Synthesis, characterization and absorption saturation of Co:$ZnAl_2O_4$ (gahnite) transparent ceramic and glass-ceramics: a comparative study, J. Alloy. Compd. 725 (2017) 998-1005. https://doi.org/10.1016/j.jallcom.2017.07.239.

[41] I.P. Alekseeva, O.S. Dymshits, V.V. Golubkov, P.A. Loiko, M.Y. Tsenter, K.V. Yumashev, S.S. Zapalova, A.A. Zhilin, Influence of NiO on phase transformations and optical properties of ZnO-Al_2O_3-SiO_2 glass-ceramics nucleated by TiO_2 and ZrO_2. Part I. Influence of NiO on phase transformations of ZnO-Al_2O_3-SiO_2 glass-ceramics nucleated by TiO_2 and ZrO_2, J. Non-Cryst. Solids 384 (2014) 73-82. https://doi.org/10.1016/j.jnoncrysol.2013.05.038.

[42] A. Chopelas, A.M. Hofmeister, Vibrational spectroscopy of aluminate spinels at 1 atm and of $MgAl_2O_4$ to over 200 kbar, Phys. Chem. Minerals 18 (1991) 279-293. https://doi.org/10.1007/BF00200186.

[43] J.X. Wang, A.Q. Wang, D.M. Hu, X.L. Wu, Y. Liu, T.J. Chen, Synthesis, characterization and properties of Ni^{2+}-doped $ZnAl_2O_4$-based spinel-type solid acid catalysts: $SO_4^{2-}/Ni_xZn_{1-x}Al_2O_4$, Mater. Chem. Phys. 239 (2020) 122319. https://doi.org/10.1016/j.matchemphys.2019.122319.

[44] E. Ghanti, R. Nagarajan, Synthesis of $CuAl_2(acac)_4(O^iPr)_4$, its hydrolysis and formation of bulk $CuAl_2O_4$ from the hydrolyzed gels; a case study of molecules to materials, Dalton Trans. 39 (26) (2010) 6056-6061. https://doi.org/10.1039/B926579A.

[45] L. Malavasi, P. Galinetto, M.C. Mozzati, C.B. Azzoni, G. Flor, Raman spectroscopy of AMn_2O_4 (A = Mn, Mg and Zn) spinels, Phys. Chem. Chem. Phys. 4 (15) (2002) 3876-3880. https://doi.org/10.1039/B203520K.

[46] V. Mohaček-Grošev, M. Vrankić, A. Maksimović, V. Mandić, Influence of titanium doping on the Raman spectra of nanocrystalline $ZnAl_2O_4$, J. Alloy. Compd. 697 (2017)

90-95. https://doi.org/10.1016/j.jallcom.2016.12.116.

[47] J.M. Xiang, X. Zhou, X.Q. Zhao, Z.Y. Wu, C.H. Chen, X.J. Zhou, C.F. Guo, Ab initio site-selective occupancy and luminescence enhancement in broadband NIR emitting phosphor $Mg_7Ga_2GeO_{12}:Cr^{3+}$, Laser Photonics Rev. 17 (7) (2023) 2200965. https://doi.org/10.1002/lpor.202200965.

[48] J. Qin, J.M. Xiang, H. Suo, Y.H. Chen, Z.Y. Zhang, X.Q. Zhao, Y.F. Wu, C.F. Guo, NIR persistent luminescence phosphor $Zn_{1.3}Ga_{1.4}Sn_{0.3}O_4:Yb^{3+},Er^{3+},Cr^{3+}$ with 980 nm laser excitation, J. Mater. Chem. C 7 (38) (2019) 11903-11910. https://doi.org/10.1039/C9TC03882E.

[49] S.V. Motloung, F.B. Dejene, H.C. Swart, O.M. Ntwaeaborwa, Effects of Cr^{3+} mol% on the structure and optical properties of the $ZnAl_2O_4:Cr^{3+}$ nanocrystals synthesized using sol-gel process, Ceram. Int. 41 (5) (2015) 6776-6783. https://doi.org/10.1016/j.ceramint.2015.01.124.

[50] Q. Wu, P.L. Li, Z.J. Ye, X.X. Huo, H.F. Yang, Y. Wang, D.W. Wang, J.X. Zhao, Z.P. Yang, Z.J. Wang, Near-infrared emitting phosphor $LaMg_{0.5}(SnGe)_{0.5}O_3:Cr^{3+}$ for plant growth applications: crystal structure, luminescence, and thermal stability, Inorg. Chem. 60 (21) (2021) 16593-16603. https://doi.org/10.1021/acs.inorgchem.1c02474.

[51] Q. Wang, S.W. Wang, T. Tan, J.T. Wang, R. Pang, D. Li, C.Y. Li, H.J. Zhang, Efficient Cr^{3+}-activated $NaInP_2O_7$ phosphor for broadband near-infrared LED applications, Inorg. Chem. Front. 9 (15) (2022) 3692-3701. https://doi.org/10.1039/D2QI00794K.

[52] S.K. Sampath, J.F. Cordaro, Optical properties of zinc aluminate, zinc gallate, and zinc aluminogallate spinels, J. Am. Ceram. Soc. 81 (3) (1998) 649-654. https://doi.org/10.1111/j.1151-2916.1998.tb02385.x.

[53] S.K. Sampath, D.G. Kanhere, R. Pandey, Electronic structure of spinel oxides: zinc aluminate and zinc gallate, J. Phys.: Condens. Matter 11 (1999) 3635-3644. https://doi.org/10.1088/0953-8984/11/18/301.

[54] L. Xi, L. Pan, Y. Wang, P.D. Townsend, The influence of doped Cr ions on the luminescence properties of infrared long persistent phosphor $ZnAl_2O_4$ with the substitution of Ge ions, J. Lumin. 233 (2021) 117941.

https://doi.org/10.1016/j.jlumin.2021.117941.

[55] W. Nie, F.M. Michel-Calendini, C. Linares, G. Boulon, C. Daul, New results on optical properties and term-energy calculations in Cr^{3+}-doped $ZnAl_2O_4$, J. Lumin. 46 (3) (1990) 177-190. https://doi.org/10.1016/0022-2313(90)90038-D.

[56] Y.X. Zhuang, J. Ueda, S. Tanabe, P. Dorenbos, Band-gap variation and a self-redox effect induced by compositional deviation in $Zn_xGa_2O_{3+x}$:Cr^{3+} persistent phosphors, J. Mater. Chem. C 2 (28) (2014) 5502-5509. https://doi.org/10.1039/C4TC00369A.

[57] M. Allix, S. Chenu, E. Véron, T. Poumeyrol, E.A. Kouadri-Boudjelthia, S. Alahraché, F. Porcher, D. Massiot, F. Fayon, Considerable improvement of long-persistent luminescence in germanium and tin substituted $ZnGa_2O_4$, Chem. Mater. 25 (9) (2013) 1600-1606. https://doi.org/10.1021/cm304101n.

[58] R. Chen, Glow curves with general order kinetics, J. Electrochem. Soc. 116 (1969) 1254-1257. https://doi.org/10.1149/1.2412291.

[59] G. Kitis, J.M. Gomez-Ros, J.W.N. Tuyn, Thermoluminescence glow-curve deconvolution functions for first, second and general orders of kinetics, J. Phys. D: Appl. Phys. 31 (1998) 2636-2641. https://doi.org/10.1088/0022-3727/31/19/037.

[60] N. Pathak, P.S. Ghosh, S. Saxena, D. Dutta, A.K. Yadav, D. Bhattacharyya, S.N. Jha, R.M. Kadam, Exploring defect-induced emission in $ZnAl_2O_4$: an exceptional color-tunable phosphor material with diverse lifetimes, Inorg. Chem. 57 (7) (2018) 3963-3982. https://doi.org/10.1021/acs.inorgchem.8b00172.

[61] Z.F. Qiu, Y.Y. Zhou, M.K. Lü, A.Y. Zhang, Q. Ma, Combustion synthesis of long-persistent luminescent MAl_2O_4:Eu^{2+},R^{3+} (M = Sr, Ba, Ca, R = Dy, Nd and La) nanoparticles and luminescence mechanism research, Acta Mater. 55 (8) (2007) 2615-2620. https://doi.org/10.1016/j.actamat.2006.12.018.

[62] C. Wang, Y.Y. Cai, H. Zhang, Z.C. Liu, H.Y. Lv, X.D. Zhu, Y. Liu, C.C. Wang, J.B. Qiu, X. Yu, X.H. Xu, Variation from zero to negative thermal quenching of phosphor with assistance of defect states, Inorg. Chem. 60 (24) (2021) 19365-19372. https://doi.org/10.1021/acs.inorgchem.1c03188.

[63] Z. Zhou, H.F. Zhu, X. Huang, Y.L. She, Y. Zhong, J. Wang, M. Liu, W. Li, M. Xia, Anti-thermal-quenching, color-tunable and ultra-narrow-band cyan green-emitting

phosphor for w-LEDs with enhanced color rendering, Chem. Eng. J. 433 (2022) 134079. https://doi.org/10.1016/j.cej.2021.134079.

[64] S.Y. Lee, Y.H. Shin, Y. Kim, S. Kim, S. Ju, Thermal quenching behavior of emission bands in Eu-doped ZnS nanowires, J. Lumin. 131 (7) (2011) 1336-1339. https://doi.org/10.1016/j.jlumin.2011.03.026.

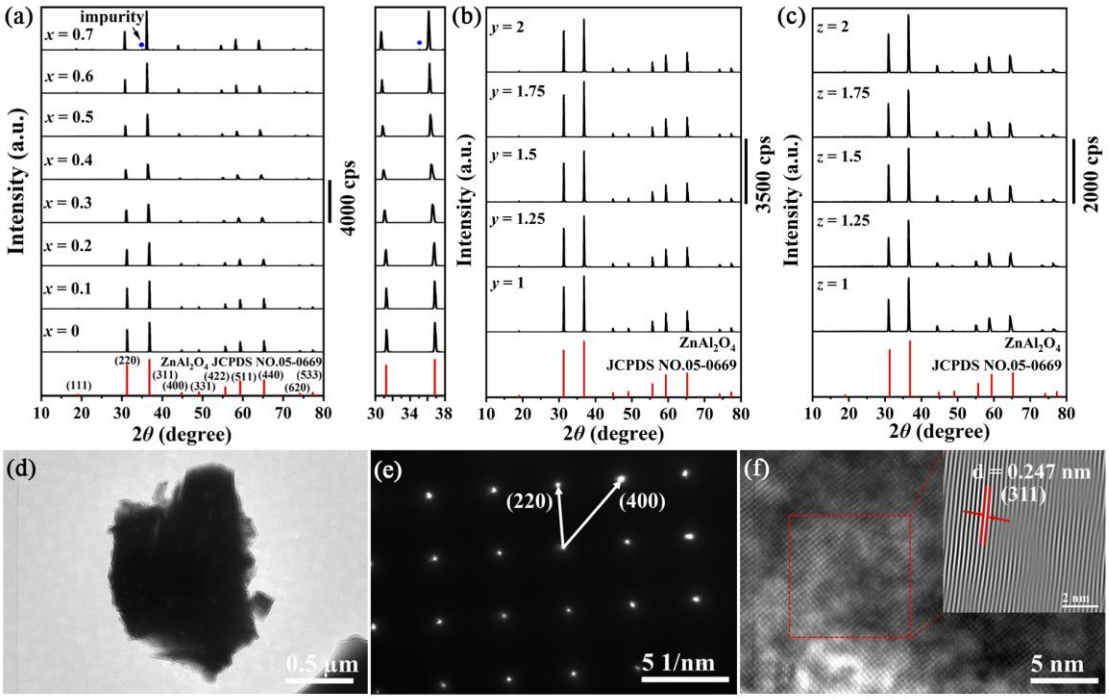

Fig. 1. XRD patterns for (a) $ZnAl_{1.975-2x}Mg_xGe_xO_4$:1.25 at.%$Cr^{3+}$ (x = 0-0.7) powders and enlarged XRD data within the 2θ range of 30-38°, (b) $ZnAl_2O_4$:y at.%Cr^{3+} (y = 1-2), and (c) $ZnAl_{1.2}Mg_{0.4}Ge_{0.4}O_4$:$z$ at.%Cr^{3+} (z = 1-2) powders calcined at 1500 ℃. The standard diffraction of $ZnAl_2O_4$ (JCPDS No.05-0669) is included as red vertical bars for comparison. (d) TEM image, (e) SAED pattern, and (f) HR-TEM image of the $ZnAl_{1.975-2x}Mg_xGe_xO_4$:1.25 at.% Cr^{3+} (x = 0.4) sample.

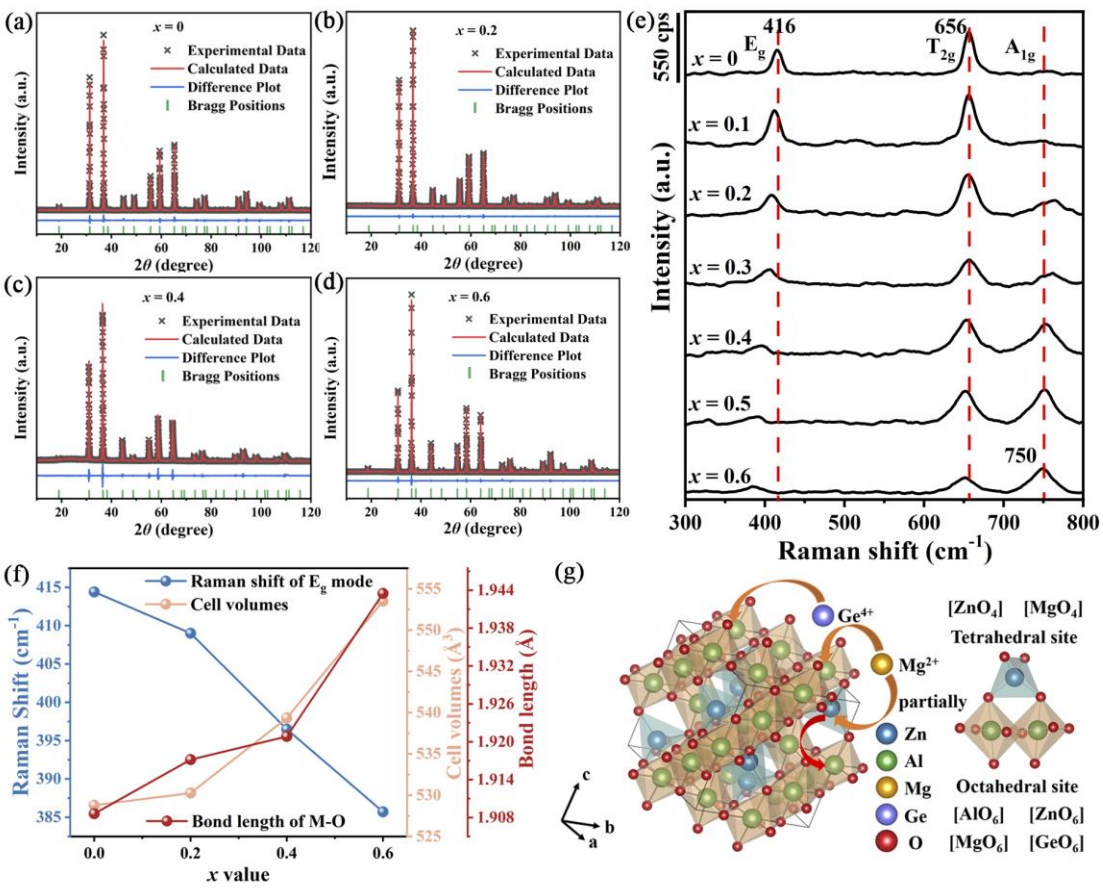

Fig. 2. The Rietveld refinements of the XRD patterns for the ZAMG:Cr^{3+} samples with different *x* values: (a) *x* = 0, (b) *x* = 0.2, (c) *x* = 0.4, and (d) *x* = 0.6. (e) Raman spectra for the ZAMG:Cr^{3+} samples (*x* = 0-0.6). (f) Raman shift of E_g mode, cell volume, and bond length of MO_6 (M = Al/Mg/Ge/Cr) octahedra evolution along with increased *x*. (g) Crystal structure of the $ZnAl_2O_4$ spinel, showing the occupancy of Mg^{2+}/Ge^{4+} and potential tetrahedral and octahedral coordinations.

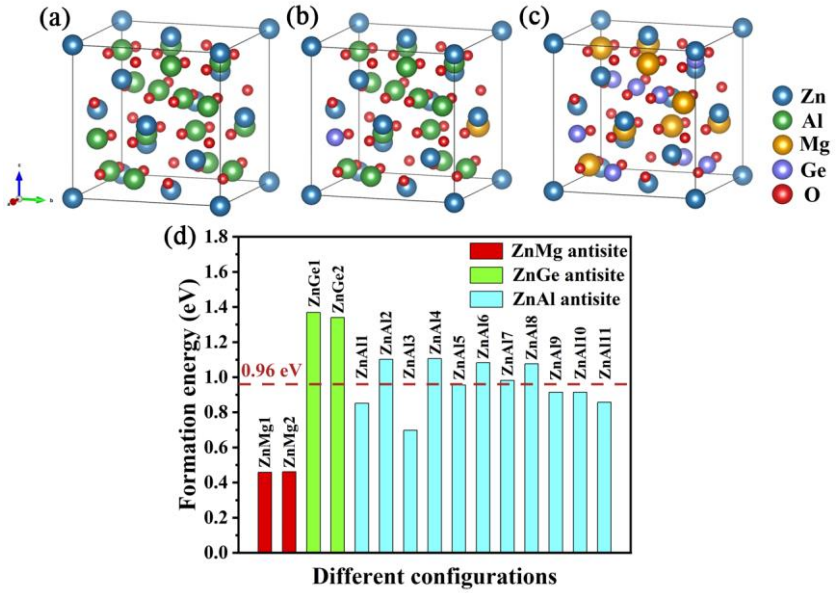

Fig. 3. Crystal structure of ZAMG with 56-atom unit cells: (a) UC-1, (b) UC-2, and (c) UC-3. (d) Calculated formation energies (ΔE_f) of potential antisite configurations in UC-2.

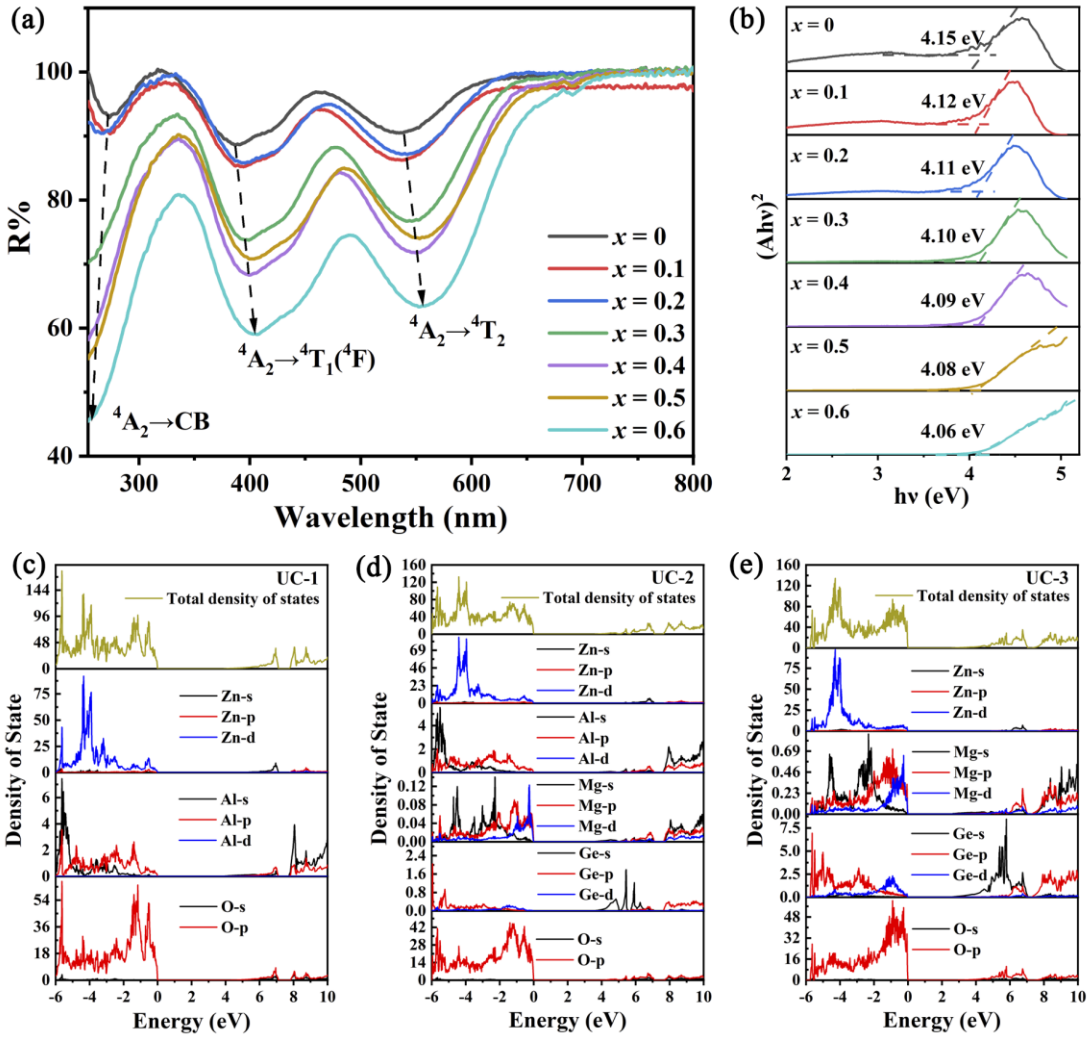

Fig. 4. (a) Diffuse Reflectance (DR) spectra of ZAMG:Cr^{3+} (x = 0-0.6) and (b) determination of bandgap energies for ZAMG (x = 0-0.6). Total and partial density of states (DOS) of $ZnAl_2O_4$ spinel with and without Mg^{2+}/Ge^{4+} doping: (c) UC-1, (d) UC-2, and (e) UC-3. The Fermi energy is used as zero energy.

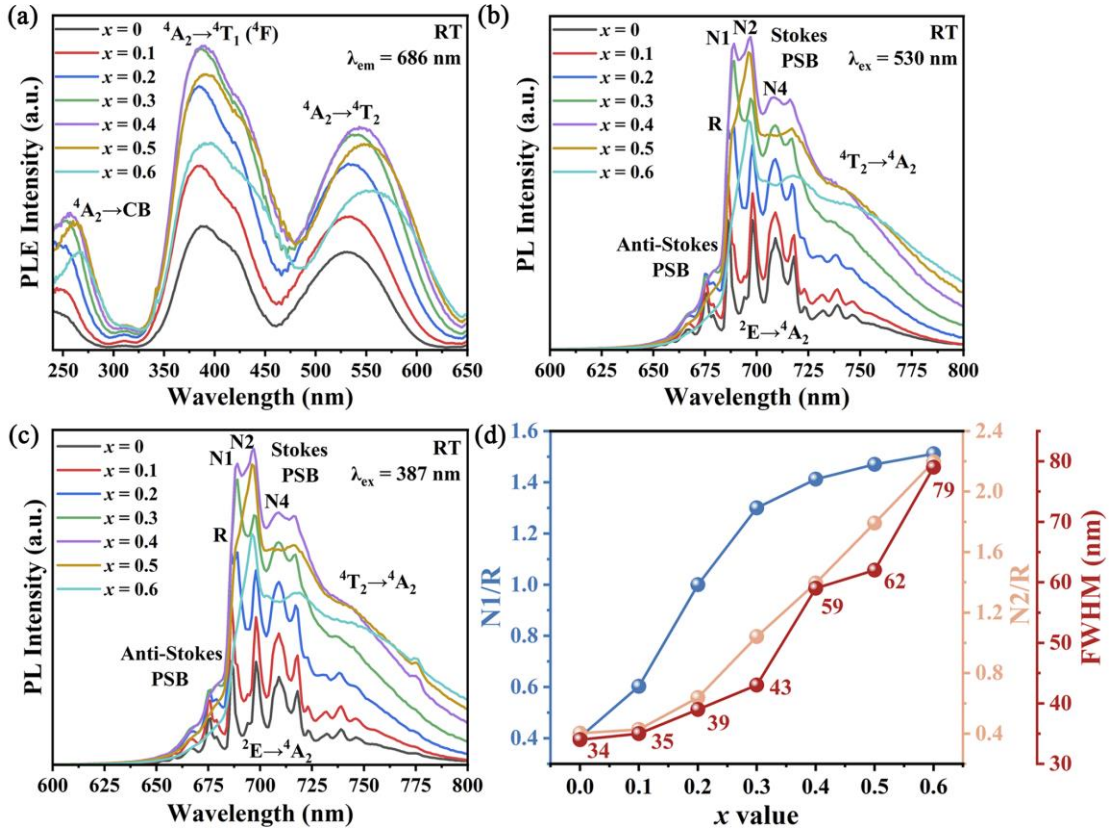

Fig. 5. (a) PLE and (b, c) PL spectra of the ZAMG:Cr^{3+} samples (x = 0-0.6) at room temperature. (d) The intensity ratios of the N1/R, N2/R lines, and FWHM of emission band obtained from normalized PL spectra of the ZAMG:Cr^{3+} samples (x = 0-0.6) under excitation at 387 nm.

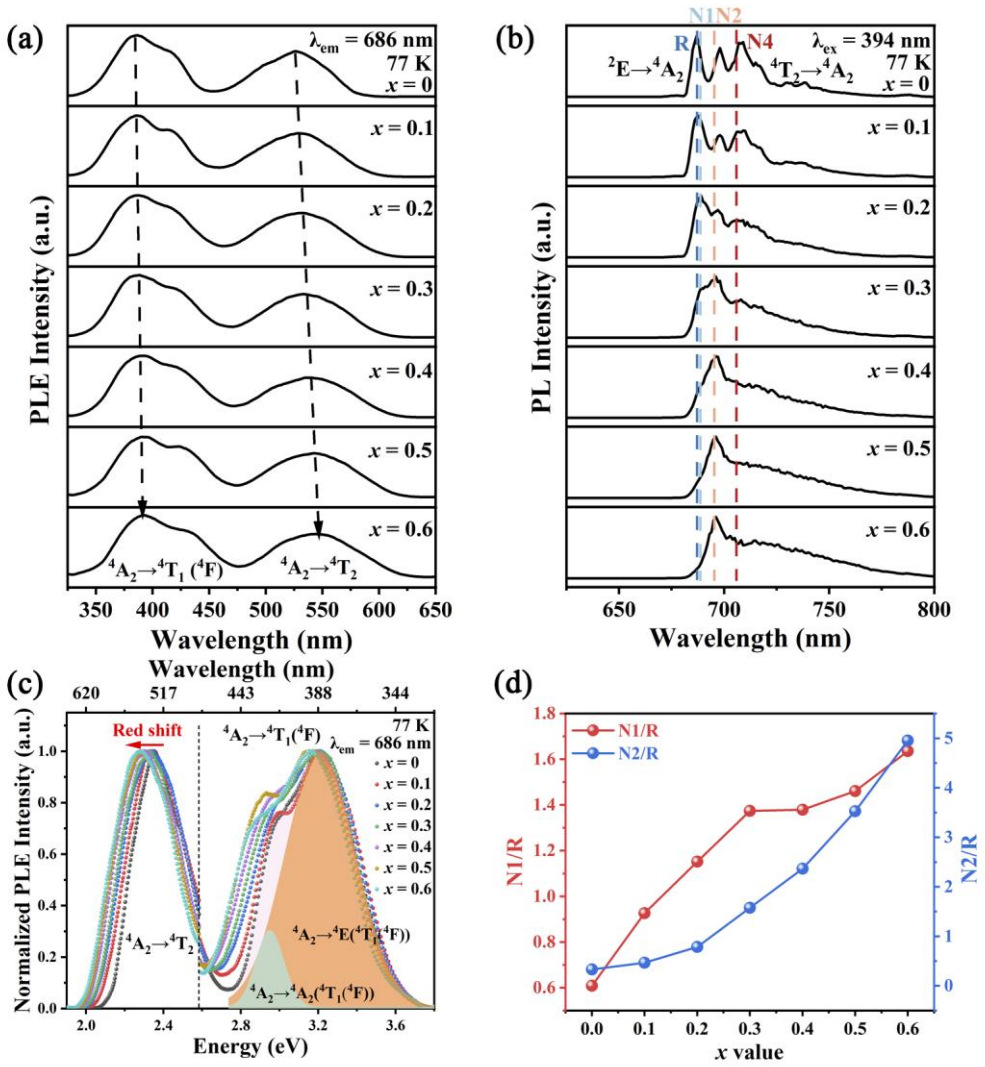

Fig. 6. (a) PLE and (b) PL spectra of the ZAMG:Cr^{3+} samples (x = 0-0.6) at 77 K. (c) The normalized PLE spectra from (a). (d) The intensity ratios of the N1/R and N2/R lines are taken as functions of x.

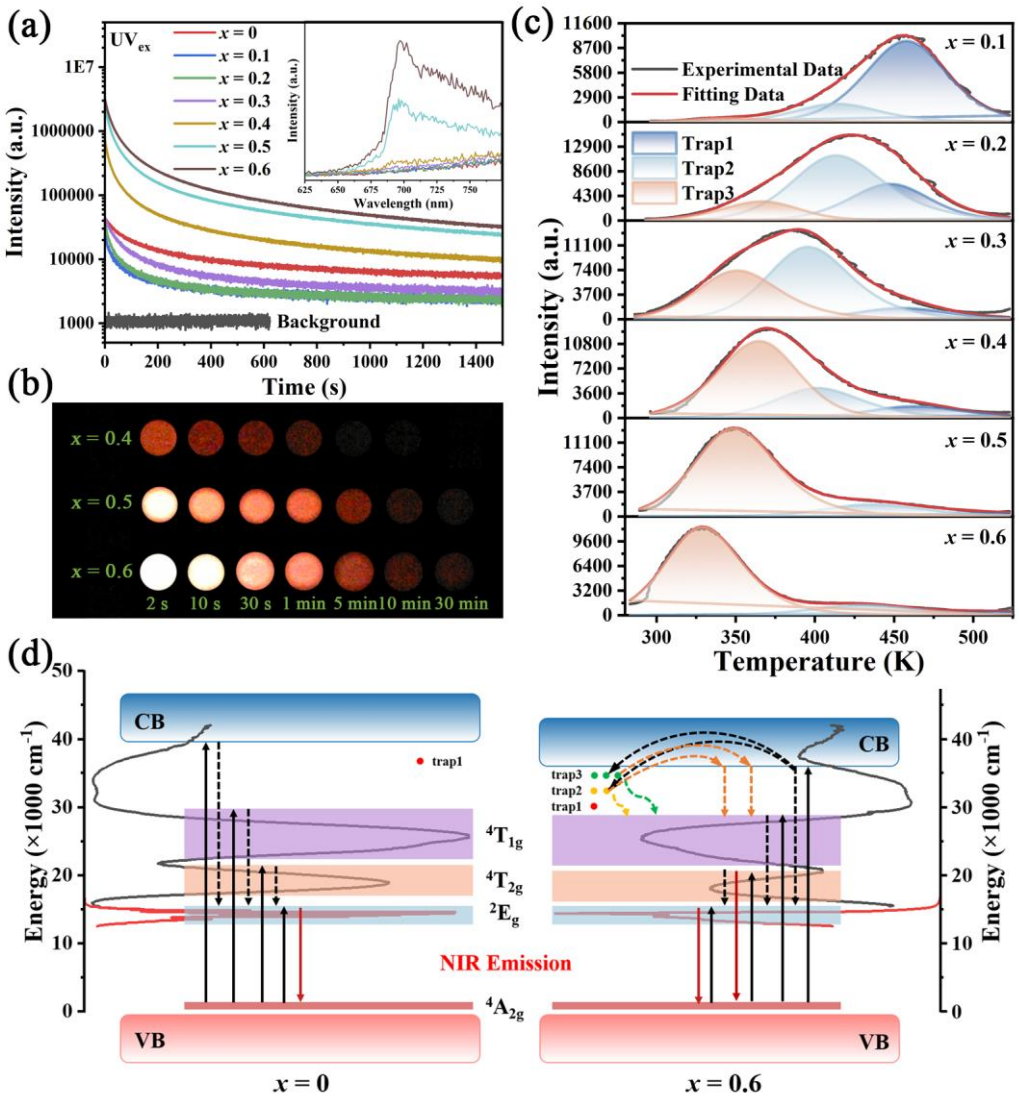

Fig. 7. (a) NIR-persistent luminescence decay curves, (b) NIR afterglow images, and (c) TL glow curves of the ZAMG:Cr^{3+} samples (x = 0-0.6) obtained after irradiation by UV light for 10 min. The inset of (a) shows their NIR-persistent luminescence spectra. (d) Mechanism diagram of persistent luminescence in the ZAMG:Cr^{3+} phosphors.

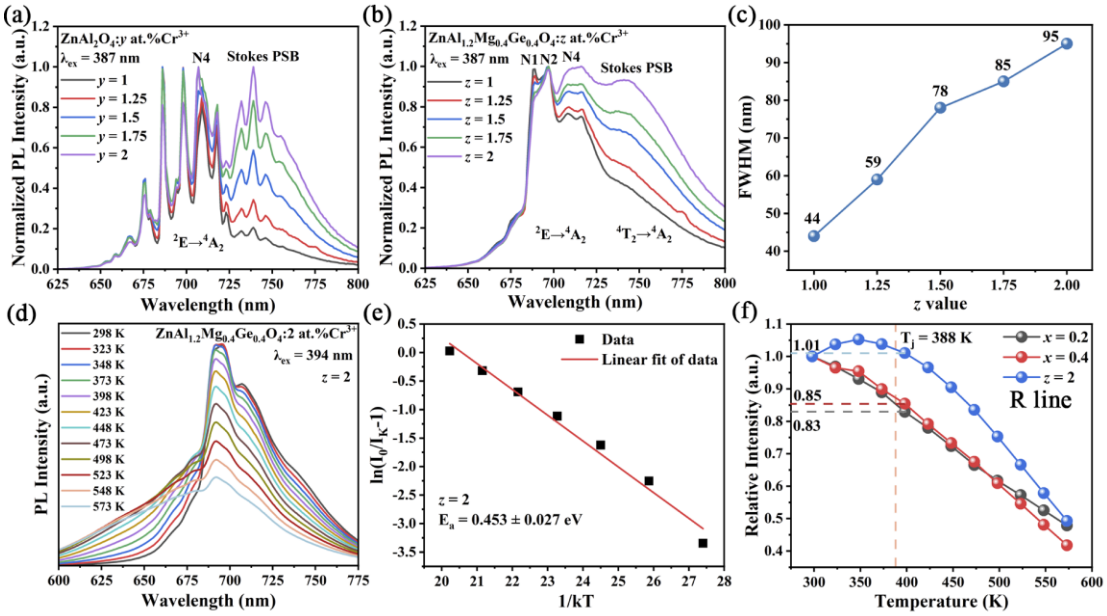

Fig. 8. Normalized PL spectra of (a) ZAO:Cr^{3+} (y = 1-2) and (b) ZA(MG)$_{0.4}$:Cr^{3+} (z = 1-2) under excitation at 387 nm at RT. (c) The variation of FWHM of ZA(MG)$_{0.4}$:Cr^{3+} as a function of z value. (d) Temperature-dependent PL spectra and (e) the Ln(I_0/I_K-1) *vs*. 1/kT plot for the ZA(MG)$_{0.4}$:Cr^{3+} (z = 2) sample. (f) is the temperature dependence of integral PL intensity of R line of the ZAMG:Cr^{3+} (x = 0.2, 0.4) and ZA(MG)$_{0.4}$:Cr^{3+} (z = 2) samples.

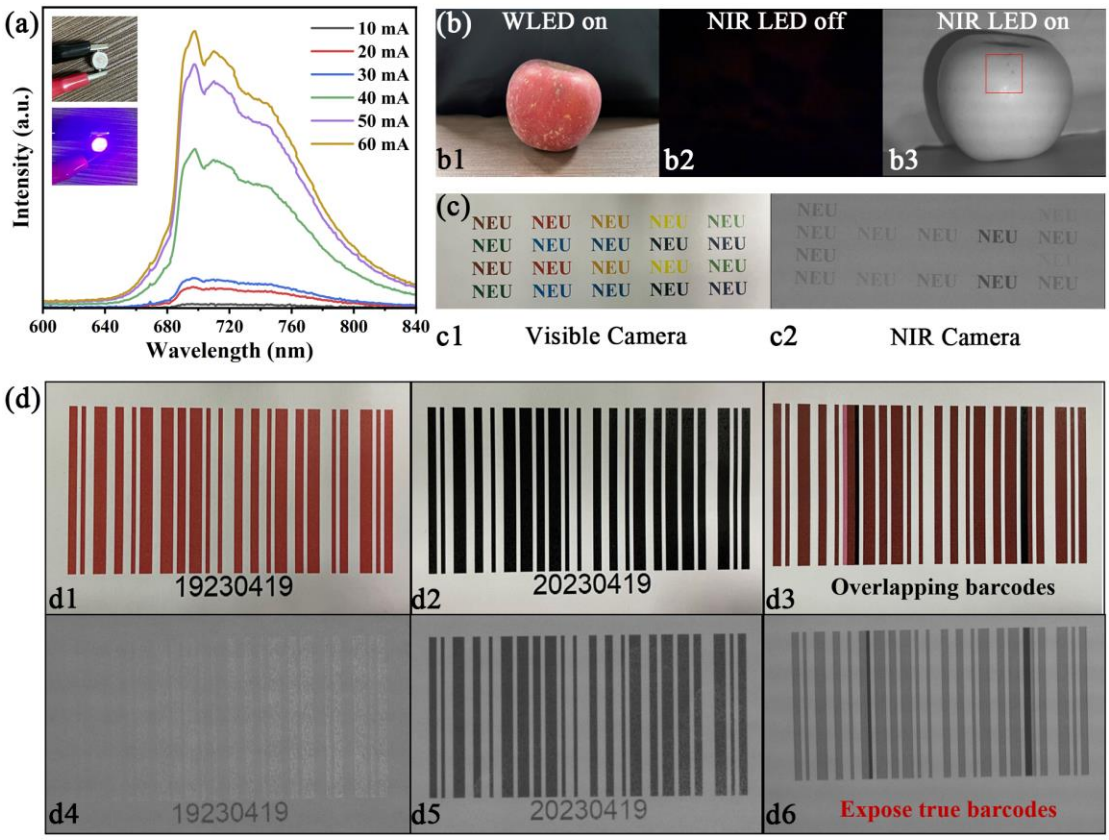

Fig. 9. (a) EL spectra of the fabricated NIR pc-LED. The insets show the images of the NIR pc-LED device under the lighted and unlighted states. Photographs of (b) apple, (c) printed words in different colors, and (d) barcodes in red or black detected by visible camera or NIR camera under corresponding white light or NIR pc-LED irradiation.

Large-scale irrigation of Cr^{3+} into different octahedra of zinc aluminate toward continual broadband near-infrared emission

Lu Chen[a], Sisi Yu[a], Guichang Shen[b], Shuai Tang[b], Tao Zhang[c], Ji-Guang Li[d], Qi Zhu[a*]

[a]*Key Laboratory for Anisotropy and Texture of Materials (Ministry of Education), School of Materials Science and Engineering, Northeastern University, Shenyang, Liaoning 110819, China*

[b]*State Key Laboratory of Rolling and Automation, Northeastern University, Shenyang, Liaoning 110819, China*

[c]*Shenyang National Laboratory for Materials Science, Northeastern University, Shenyang, Liaoning 110819, China*

[d]*Research Center for Functional Materials, National Institute for Materials Science, Namiki 1-1, Tsukuba, Ibaraki 305-0044, Japan*

*Corresponding author

Dr. Qi Zhu

Tel: +86-24-8367-2700

E-mail: zhuq@smm.neu.edu.cn

ABSTRACT

Broadband near-infrared (NIR) phosphors, as key materials in NIR phosphor-converted light-emitting diodes (pc-LED) for emerging applications, have recently attracted considerable attention. Herein, by selecting a comprehensive engineering strategy of co-substituting [Al^{3+}-Al^{3+}] with [Mg^{2+}-Ge^{4+}] units and increasing Cr^{3+} concentration, a novel Cr^{3+}-doped $ZnAl_{1.16}Mg_{0.4}Ge_{0.4}O_4$ ($ZA(MG)_{0.4}$:2 at.%Cr^{3+}) phosphor with continual broadband NIR emission was synthesized. The site occupation of Mg^{2+}/Ge^{4+} in $ZnAl_2O_4$ is unraveled by Rietveld structure refinement and density functional theory (DFT) calculations. According to the photoluminescence behaviors, the formed defect clusters of $Zn_{Al}^{'}$-Cr^{3+}-$Ge_{Al}^{\cdot}$ and $Mg_{Al}^{'}$-Cr^{3+}-$Ge_{Al}^{\cdot}$ can not only introduce shallow defects to serve as new traps to obtain long-persistent luminescence but can also enhance the emission intensity at ~689 nm and ~694 nm. The quantity and scale of Cr^{3+}-Cr^{3+} pairs and Cr^{3+} in distorted sites, which can improve the thermal quenching resistance and emission intensity in the range of 700-800 nm, can be accurately regulated by varying the concentration of Cr^{3+}. Under 387 nm excitation, the designed material exhibits intensive NIR emission from 685 to 750 nm with a wide full-width at half maximum (FWHM) of 95 nm. The electroluminescence spectrum and potential applications of the NIR pc-LED prepared using $ZA(MG)_{0.4}$:2 at.%Cr^{3+} phosphor are also reported. The results promise a feasible strategy to develop NIR phosphors as NIR pc-LEDs lighting sources for applications in nondestructive detection and anticounterfeiting.

Keywords: Chemical unit co-substitution, Defect clusters, Distorted site, Near-infrared persistent luminescence, Broadband emission

1. Introduction

Recently, near-infrared (NIR) light sources have attracted considerable research attention due to their wide application in the fields of bioimaging/sensing, night vision, plant growth, food detection, anticounterfeiting, and so on [1-3]. Traditional NIR light sources, such as tungsten-halogen lamps and supercontinuum lasers, usually have the disadvantages of bulkiness, low luminous efficiency, poor thermal stability, and narrow emission bands. These traditional NIR sources are expected to be replaced by NIR phosphor-converted light-emitting diodes (pc-LEDs), which consist of an LED chip and NIR-emitting phosphors. NIR pc-LEDs have the advantages of compactness, portability, efficiency, and low energy consumption [4-7]. Therefore, developing a highly efficient broadband NIR-emitting phosphor is crucial for expansion applications, as the performance of NIR pc-LEDs is determined by the NIR phosphors used. Both rare earth ions, such as Eu^{2+}, and transition metal ions, such as Cr^{3+} and Mn^{2+}, can serve as activators for broadband NIR-emitting phosphors [8-10]. However, the currently Eu^{2+}-doped NIR phosphors typically exhibit low quantum efficiency and limited emission bandwidth. In contrast, Cr^{3+}-doped NIR phosphors have received considerable attention owing to their broadband and efficient NIR emission, which are regarded as the most promising NIR phosphors for NIR pc-LEDs [11, 12]. Many kinds of broadband NIR phosphors doped with Cr^{3+} have been reported recently, for instance, $Ga_4GeO_8:Cr^{3+}$ (λ_{em} = 850 nm; FWHM = 215 nm) [13], $LiGaP_2O_7:Cr^{3+}$ (λ_{em} = 840 nm; FWHM = 170 nm) [14], $Lu_2CaMg_2Ge_3O_{12}:Cr^{3+}$ (λ_{em} = 795 nm; FWHM = 152 nm) [15], and $Mg_2SnO_4:Cr^{3+}$ (λ_{em} = 800 nm; FWHM = 180 nm) [6]. Unfortunately, most of these Cr^{3+}-doped NIR phosphors still suffer from low thermal stability and insufficient effective broadband emission (the emission intensity reaches the maximum only at a certain wavelength), which will hinder their applications for pc-LEDs. Hence, it is necessary to develop Cr^{3+}-activated NIR phosphors to achieve highly efficient broadband NIR emission.

It is known that the d-d transition of Cr^{3+} is greatly affected by the crystal field environment, which is dependent on the crystal structure of the matrix [16]. Owing to

the appropriate bandgap and tunable crystal field, spinel oxides AB_2O_4 are suitable for hosting Cr^{3+} to generate broadband NIR emission accompanied by a long afterglow duration. Normally, AB_2O_4 comprises two types of coordination polyhedral with the divalent cation A occupying the tetrahedral site and trivalent cation B occupying the octahedral site [17]. The antisite defects generated by the exchange of cations A and B can introduce a local electric field and serve as energy storage centers, which are crucial for the persistent luminescence (PersL) and duration of AB_2O_4:Cr^{3+} phosphors [18-20]. Among the spinel family, $ZnGa_2O_4$ and its related solid solutions are known to exhibit wide excitation and emission ranges as well as superlong NIR PersL due to a suitable number of antisite defects [21-23]. After being pre-charged by the excitation source, NIR PersL phosphors, which can continuously emit light for minutes to hours, have received particular interest as biomarker probes for background-free biomedical imaging [24]. Zinc aluminate ($ZnAl_2O_4$) is another AB_2O_4 compound with a similar structure to $ZnGa_2O_4$, which is considered a potential candidate for cost-prohibitive gallate and gallogermanate oxides. However, the low level of intrinsic antisite defects (less than 1%) results in unsatisfactory optical properties of $ZnAl_2O_4$:Cr^{3+}, including NIR photoluminescence (PL) and PersL [19, 20].

In consideration of the intensive influence of the matrix local structure on the optical properties of Cr^{3+}-activated phosphors, several strategies for broadening spectra and enhancing afterglow are effectively demonstrated. 1) Introducing dopants at the octahedral site to tailor the local crystal field around the activator center Cr^{3+}; this is because in the medium-strength ligand field with $Dq/B \approx 2.3$, Cr^{3+} would give a mixture of narrow-band emission (~700 nm) and broadband emission (650-1600 nm) originating from the $^2E \rightarrow {}^4A_2$ and $^4T_2 \rightarrow {}^4A_2$ transitions, respectively [25, 26]. For example, precise adjustment of the local crystal field around Cr^{3+} is realized by adding aluminum into the Sn^{4+} site of Zn_2SnO_4:Cr^{3+} [27] or replacing gallium with tin in $ZnGa_2O_4$: Cr^{3+} [28] to obtain a tunable chromium emission band. 2) Generating distorted octahedral defects could enhance the luminescence of Cr^{3+} in distorted sites using the chemical unit co-substitution method. Moreover, the formed defect clusters can store and release excited electrons that contribute to the long-lasting NIR PersL and

excellent thermal stability [7, 22, 29]. Successful examples can be found in increasing the delayed emission and the NIR emission intensity of $ZnGa_2O_4$ by co-substitution of [Mg^{2+}-Ge^{4+}] for [Ga^{3+}-Ga^{3+}] [30, 31]. 3) Increasing the concentration of Cr^{3+} can not only improve the emission corresponding to Cr^{3+}-Cr^{3+} pairs [32, 33] but also increase the probability of Cr^{3+} neighboring antisite defects (denoted as Cr_{N2}^{3+}) and further increase the emission intensity of Cr_{N2}^{3+}. Thus, comprehensively engineering a distorted environment is of utmost importance for integrating the broadband NIR PL and PersL for $ZnAl_2O_4$:Cr^{3+}.

In this work, we designed and synthesized a high-content Cr^{3+}-doped $ZnAl_{1.16}Mg_{0.4}Ge_{0.4}O_4$ phosphor that exhibits continuous broadband near-infrared emission with a full width at half maximum (FWHM) of 95 nm *via* a solid-state reaction. [Mg^{2+}-Ge^{4+}] was first used to replace [Al^{3+}-Al^{3+}] in $ZnAl_2O_4$:Cr^{3+} to generate defect clusters of $Zn_{Al}^{'}$-Cr^{3+}-$Ge_{Al}^{\cdot}$ and $Mg_{Al}^{'}$-Cr^{3+}-$Ge_{Al}^{\cdot}$, which are beneficial for obtaining long-lasting NIR PersL and enhancing the emission intensity at ~689 nm and ~694 nm. Then, the introduction of excessive Cr^{3+} led to further enhancement of the emission intensity in the range of 700-800 nm, mainly due to Cr^{3+}-Cr^{3+} pairs and more Cr^{3+} in distorted sites. This work not only presents a comprehensive strategy for developing tunable NIR phosphors, but also demonstrates the potential applications for NIR pc-LEDs lighting sources.

2. Experimental section

2.1. Materials and synthesis

A series of $ZnAl_{1.975-2x}Mg_xGe_xO_4$:1.25 at.% Cr^{3+} (ZAMG:Cr^{3+}, x = 0-0.7), $ZnAl_{2-0.02y}O_4$:y at.%Cr^{3+} (ZAO:Cr^{3+}, y = 1-2), and $ZnAl_{1.2-0.02z}Mg_{0.4}Ge_{0.4}O_4$:$z$ at.%Cr^{3+} (ZA(MG)$_{0.4}$:Cr^{3+}, z = 1-2) phosphors were synthesized through high-temperature solid-state reaction. Al_2O_3 (99.99%), ZnO (99.99%), Cr_2O_3 (99.95%), MgO (99.99%), and GeO_2 (99.99%) purchased from Aladdin were employed as raw materials. The above materials were weighted accurately according to the stoichiometric ratio. And then, the mixtures were transferred into an agate mortar and finely grounded for 30 min to form homogeneous powders. After prefiring at 1000 ℃ for 2 h, the materials were ground again for more than 10 min and subsequently sintered at 1500 °C for 6 h in air

atmosphere.

2.2. Measurements and characterization

X-ray diffraction (XRD, Model SmartLab, Rigaku, Tokyo, Japan) operating at 40 kV/200 mA and using nickel-filtered Cu Kα radiation (λ = 0.15406 nm) was used to collect the XRD results of all samples. The data was measured at a scanning speed of 10° 2θ/min from 10° to 80° in the continuous-scan mode. The XRD data for Rietveld refinement was obtained in a step-scan mode over the 2θ range of 10-120°, using a step interval of 0.02° and a counting time of 1 s/step. Transmission electron microscopy (TEM, Model JEM-2000FX, JEOL, Tokyo) was employed to observe the morphology of product. Selected area electron diffraction (SAED) and High-Resolution TEM (HR-TEM) were used to further confirm the crystal structure of the samples. The structure of coordination polyhedral was evaluated using the Raman microscope (Model R-XploRA Plus, Horiba, Kyoto, Japan) with a 532 nm laser as the excitation source. The formation energies (ΔE_f) of different antisite configurations were calculated using density functional theory (DFT) method with the help of the Vienna ab initio Simulation Package (VASP) [34-36]. The electron interaction with ions was replaced by the projector augmented wave (PAW) method, and the generalized gradient approximation (GGA) with the Perdew-Burke-Ernzerhof (PBE) functional was employed as the exchange-correlation potential [37]. The cut-off energy E_{cut} for the plane-wave basis set was fixed value of 520 eV. The crystal lattice was fully relaxed until the force on each atom was less than 0.01 eV $Å^{-1}$. Diffuse reflectance (DR) spectra were performed on the UV-Vis-NIR spectrophotometer (UV-3600 Plus, Shimadzu, Kyoto, Japan). The photoluminescence spectra, including the PL and PLE spectra, at 77 K and in the range of 298-573 K were measured by the fluorospectrophotometer (Model FP-8600, Jasco, Tokyo) with a slit of 10 nm for both excitation and emission. The PL, PLE, persistent luminescence emission (PersL) spectra, as well as persistent luminescence decay curves at room temperature (RT) were recorded using a model JY FL3-21 spectrophotometer (Horiba, Kyoto). The night vision apparatus (P4-0118, ZHANEN, China) was employed to take NIR pictures. The thermoluminescence (TL) glow curves were measured using an FJ-427A TL meter (Beijing Nuclear Instrument Factory). The

samples were first exposed to an UV lamp for 10 min before collecting PersL spectra, PersL decay curves, NIR pictures, and TL curves.

2.3. LED performances

The NIR pc-LED device was fabricated by using the 395 nm UV chip and the as-synthesized $ZnAl_{1.16}Mg_{0.4}Ge_{0.4}O_4$:2 at.%$Cr^{3+}$ phosphor with NIR broadband emitting. The mass ratio of the mixture of type A and B epoxy resin to NIR phosphor was set as 1:1. The electroluminescence (EL) spectra of the fabricated NIR pc-LED were collected with a Model HS-1000 spectral detector (Otsuka Electronics Co. Ltd., Osaka, Japan). The photoelectric properties of the pc-LEDs were measured by using an OHSP-350M photoelectric measuring system (600-900 nm, HOPOOCOLOR, China). The forward bias current for pc-LEDs was 20-100 mA. The electro-optical conversion efficiency is defined as the ratio of the output power of NIR emission (600-900 nm) to the input electric power of LED. Use the rear-facing camera of iPhone as the visible camera. The demonstration images using NIR pc-LED as the lighting source were taken by the near infrared IR CMOS USB digital camera (ADOS-TECH, UAB, Europe, Lithuania).

3. Results and discussion

3.1. Crystal structure and local structure of $ZnAl_{1.975-2x}Mg_xGe_xO_4$:1.25 at.% Cr^{3+}

The XRD patterns of the as-synthesized $ZnAl_{1.975-2x}Mg_xGe_xO_4$:1.25 at.% Cr^{3+} (ZAMG:Cr^{3+}, x = 0-0.7), $ZnAl_2O_4$:y at.%Cr^{3+} (ZAO:Cr^{3+}, y = 1-2), and $ZnAl_{1.2}Mg_{0.4}Ge_{0.4}O_4$:$z$ at.%Cr^{3+} (ZA(MG)$_{0.4}$:Cr^{3+}, z = 1-2) samples are shown in Fig. 1a-c. The phase structure of a series of powders is compared with the standard file of JCPDS No.05-0669 of the $ZnAl_2O_4$ phase (spinel structure). All diffraction peaks of the products coincide well with those of the standard $ZnAl_2O_4$ phase, whereas a secondary impurity of Zn_2GeO_4 (hexagonal structure) appears for ZAMG:Cr^{3+} when x further increases to 0.7. According to the amplified view of the diffractions at 2θ = 30-38°, it is clear that the diffraction peaks gradually shift toward the lower 2θ side with increasing x value. Herein, the chemical unit of [Mg^{2+}-Ge^{4+}] is introduced into $ZnAl_2O_4$ to replace [Al^{3+}-Al^{3+}], which can be attributed to the lattice expansion induced by the replacement of [Mg^{2+}-Ge^{4+}] for [Al^{3+}-Al^{3+}] in the octahedral sites, considering that the average ionic radius of the co-substituted ion pair (r = 0.625 Å, CN (coordination

number) = 6) is larger than that of Al^{3+} (r = 0.535 Å, CN = 6) [22, 29]. The ionic radii with different coordination of each substitution ion and substituted ion are shown in Table 1. In addition, the acceptable radius of Mg^{2+} (r = 0.57 Å, CN = 4) allows it to partially replace Zn^{2+} (r = 0.60 Å, CN = 4) in the tetrahedral sites, while an equal amount of Zn^{2+} will replace Al^{3+}. Given that the ionic radius of Ge^{4+} (r = 0.53 Å, CN = 6) is close to that of Al^{3+}, Ge^{4+} is more likely to replace Al^{3+} than Zn^{2+}. However, Huang and Guo et al. proposed that Ge^{4+} may also enter tetrahedral sites in the case of $Zn_{1+x}Al_{2-2x}Ge_xO_4:Cr^{3+}$ [22]. For ZAMG:Cr^{3+}, whether Ge^{4+} may replace Al^{3+} or Zn^{2+} will be discussed later. Fig. 1d shows the TEM morphology of the x = 0.4 sample. SAED and HR-TEM were performed for single particle, as shown in Fig. 1e and f. The SAED pattern shows the presence of the (220) and (400) planes of cubic $ZnAl_2O_4$, and the results indicate that the nanoparticles are single-crystalline with good crystallinity. Clear resolved lattice fringes can be observed in the HR-TEM image, and the d spacing of 0.247 nm is assigned to the (311) plane of $ZnAl_2O_4$ (cubic structure, d(311) = 0.244 nm, JCPDS No. 05-0669). Because [Mg^{2+}-Ge^{4+}] and Cr^{3+} doping contribute to lattice expansion, the interplanar spacing of the (311) plane of the ZAMG:Cr^{3+} (x = 0.4) sample was larger than the pure $ZnAl_2O_4$. The above results indicate that the sample belongs to the target cubic crystal structure.

Table 1 Ionic radii of metal elements in ZAMG:Cr^{3+} spinel solid solution.

r (Å)	Zn^{2+}	Al^{3+}	Cr^{3+}	Mg^{2+}	Ge^{4+}
r (CN = 4)	0.60	0.39	-	0.57	0.39
r (CN = 6)	0.74	0.535	0.615	0.72	0.53

To further elucidate the local structure evolution with the [Mg^{2+}-Ge^{4+}] unit co-substitution, the Rietveld refinement of the as-prepared ZAMG:Cr^{3+} (x = 0, 0.2, 0.4, and 0.6) samples was performed using TOPAS software, and the results are shown in Fig. 2a-d. All peaks can be indexed by cubic cell (*Fd3m*) and their parameters are close to the $ZnAl_2O_4$ spinel structure; hence, the crystallographic data of standard $ZnAl_2O_4$ (ICSD 94156) was taken as the initial structure model. The calculated data fit well with the experimental patterns, and the residual factors (R_{wp}, R_p and χ^2) show considerable credibility (Table S1). The consistency between the diffraction peaks and the standard

$ZnAl_2O_4$ card indicates the formation of the spinel solid solution phase without any impurities. With the increase in the substitution content of [Mg^{2+}-Ge^{4+}], the cell parameters $a = b = c$, cell volume V, and M-O (M = Al/Mg/Ge/Cr) average bond length of the MO_6 octahedra show a linear increase as shown in Fig. S1a-c, which implies the successful incorporation of Mg^{2+} and Ge^{4+}. As discussed previously, the expansion of the unit cell caused by the incorporation of [Mg^{2+}-Ge^{4+}] to replace [Al^{3+}-Al^{3+}] is due to the larger ionic radii of the Mg^{2+}-Ge^{4+} pair, which leads to the diffraction peaks shifting to the lower angle side (Fig. 1a). It has been reported that $ZnAl_2O_4$ is a near normal spinel structure without cation disorder [19, 38]. In other words, Zn^{2+} completely occupies the tetrahedral site, while Al^{3+} occupies the octahedral site in the pure $ZnAl_2O_4$ host. When the doping ion pair Mg^{2+}-Ge^{4+} is introduced, the co-substitution of Mg^{2+}/Ge^{4+} for Al^{3+} plays the dominant role due to the presence of many octahedral vacancies in the case of Zn/(Mg/Al/Ge)=0.5. On the one hand, considering the matching degree of the cation radius and valence states, it is assumed that Mg^{2+} mainly occupies the Al^{3+} site (octahedral site) and slightly occupies the Zn^{2+} site (tetrahedral site) accompanied by an equal amount of Zn^{2+} occupying the Al^{3+} site. On the other hand, the significant differences in ionic radii and valence states between Ge^{4+} (r = 0.39 Å, CN = 4) and Zn^{2+} (r = 0.60 Å, CN = 4) make Ge^{4+} entirely occupy the Al^{3+} site. The cation lattice occupancy has been refined, and the refined results are summarized in Table 2 and Table S2-5. Interestingly, with an increase in x, the occupation of Mg^{2+} in the tetrahedral site changes from 0.018 (x = 0.2) to 0.071 (x = 0.4), but with a further increase in the Mg^{2+} concentration, the occupation for x = 0.6 sample only increases slightly. This phenomenon shows that in the case of a high concentration of Mg^{2+}, $Mg_{Al}^{'}$ rather than $Zn_{Al}^{'}$ is the main defect component. Meanwhile, the substitution of the larger [MgO_6] and the smaller [GeO_6] polyhedra for [AlO_6] polyhedra could lead to local structural distortion and bond distance variation [29, 30].

The distortion of ZAMG:Cr^{3+} (x = 0-0.6) was further characterized by Raman spectroscopy, as shown in Fig. 2e. According to group theory, the phonon modes of cubic spinel (Fd3m) are predicted as follows: $\Gamma = A_{1g}(R) + E_g(R) + T_{1g} + 3T_{2g}(R) + 2A_{2u}$

+ $2E_u$ + $5T_{1u}$(IR) + $2T_{2u}$, from which the A_{1g}, E_g and $3T_{2g}$ modes are Raman-active, $5T_{1u}$ is IR-active, and the others are acoustic or silent [39, 40]. As a rule, the three strongest Raman bands at ~416, ~656 and ~750 cm^{-1} correspond to the E_g, T_{2g} and A_{1g} modes, respectively. However, it has been reported that the high-frequency band located at 750 cm^{-1} is much weaker than others in the gahnite spectrum [41, 42]. Thus, the observed band peaks at ~416 and ~656 cm^{-1} in the pure $ZnAl_2O_4$ (x = 0) sample are consistent with those for single crystal gahnite reported by Chopelas and Hofmeister [42]. It is widely accepted that the Raman modes of the spinel structure in the range of 300-600 cm^{-1} are assigned to MO_6 octahedra, while the modes in the range of 600-700 cm^{-1} are associated with MO_4 tetrahedra [30, 43, 44]. The result for x = 0 sample indicates that a large number of AlO_6 and ZnO_4 groups with symmetric stretching vibrations exist. Furthermore, with the increase in the x value, the intensities of the peaks at ~416 and ~656 cm^{-1} gradually decrease and shift to lower wavenumbers due to the transformation from symmetric AlO_6 and ZnO_4 groups to distorted AlO_6 and ZnO_4 groups by doping Mg^{2+}/Ge^{4+}. A similar phenomenon without the movement of the T_{2g} (~610 cm^{-1}) mode frequency emerges in the Raman spectra of $ZnGa_{2-x}(Mg/Ge)_xO_4:Cr^{3+}$ [30]. Here, all three Raman frequencies undergo a modest progressive softening passing, particularly the E_g mode, which is greatly related to the increase in cell volume and M-O bond length obtained from the Rietveld refinements [45], as shown in Fig. 2f; this suggests that the octahedra become more distorted and asymmetric with increasing x value, which may influence the crystal field of Cr^{3+}, thus affecting the luminescence property of the ZAMG:Cr^{3+} phosphors. In addition, an intense band with an inflection at ~750 cm^{-1} appears and gradually strengthens, due to the introduction of magnesium and germanium ions in the octahedral positions. Similarly, the Raman spectral activity present at ~720 cm^{-1} and ~780 cm^{-1} is attributed to the replacement of aluminum by titanium and zinc ions in the Ti-doped $ZnAl_2O_4$ [46]. The $ZnAl_2O_4$ spinel crystal structure is shown in Fig. 2g, which has two types of coordination polyhedra with different tetrahedral (ZnO_4 and MgO_4) and octahedral (AlO_6, ZnO_6, MgO_6 and GeO_6) sites based on the co-substitution of Mg^{2+}/Ge^{4+}. Moreover, since the average valence of [Mg^{2+}-Ge^{4+}] is similar to that of Al^{3+}, there is

no additional charge compensating defects. Thus, the opposite charged defect pairs of $Mg_{Al}^{'}$ or $Zn_{Al}^{'}$ and $Ge_{Al}^{\cdot}$ are formed, which provide a local electric field around Cr_{N2}^{3+} [30, 31]. The defect cluster of $Mg_{Al}^{'}$-Cr_{N2}^{3+}-$Ge_{Al}^{\cdot}$ may be used as an effective trap, contributing to the long-persistent luminescence [22, 30].

Table 2 The Rietveld refinement results of the octahedral and tetrahedral sites for the ZAMG:Cr^{3+} (x = 0-0.6) samples.

	Tetrahedral site		Octahedral site			
Sample	Zn^{IV}	Mg^{IV}	Zn^{VI}	Al^{VI}	Mg^{VI}	Ge^{VI}
x = 0	1	-	-	0.9875	-	-
x = 0.2	0.982	0.018	0.018	0.790	0.082	0.100
x = 0.4	0.929	0.071	0.071	0.590	0.129	0.200
x = 0.6	0.926	0.074	0.074	0.390	0.226	0.300

In addition, Mg^{2+}/Ge^{4+}/Al^{3+} may replace Zn^{2+} to form antisite defects due to Mg^{2+}/Ge^{4+} doping, leading to the different defect clusters associated with the traps. To investigate the preferential formation of antisite defects, the formation energy of potential configurations is calculated. A 56-atom unit cell of $ZnAl_2O_4$ containing 8-atom Zn, 16-atom Al, and 32-atom O is built as a model, which is defined as UC-1 in Fig. 3a. To demonstrate the variation in the band gap with increasing Mg^{2+}/Ge^{4+} doping, the model of the 56-atom unit cell of $ZnAl_2O_4$ with one Mg^{2+} and one Ge^{4+} replacing two Al^{3+} is defined as UC-2, while the similar model of $ZnAl_2O_4$ with Mg^{2+}/Ge^{4+} completely replacing Al^{3+} is used as UC-3, as shown in Figs. 3b and c. According to the atomic number ratio of Mg/Ge and Al, the corresponding Mg^{2+}/Ge^{4+} doping concentrations for UC-1, UC-2, and UC-3 crystal structure types are 0 at.%, 12.5 at.%, and 100 at.%, respectively. The exchange of Zn atoms and nearest Al atoms is equivalent in the $ZnAl_2O_4$ host, and the formation energy for Zn and Al in a non-nearby position is too large; thus, one Zn-Al antisite is first built in UC-1. To further study the site preference of ZAMG, 15 possible configurations of antisite in UC-2 are also built. These 15 configurations are established by exchanging the site of Mg, Al, and Ge atoms with one of the surrounding Zn atoms, while some antisite configurations with excessive formation energies are ignored. The formation energies (ΔE_f) are given in Fig. 3d and are calculated as [18, 31]

$$\Delta E_f = E(\text{antisite}) - E(\text{perfect}) \quad (1)$$

where E(perfect) is the total energy of the $ZnAl_2O_4$ host with or without Mg^{2+}/Ge^{4+} doping (UC-1 or UC-2) and E(antisite) is the total energy of the unit cell with either one antisite. The formation energy of the Zn-Al antisite in UC-1 is calculated as 0.96 eV. According to the work of Kashii et al. [38] and Priolkar et al. [19, 20], there is almost no cation disorder in the $ZnAl_2O_4$ spinel structure, which implies that the formation energy of Zn-Al antisite in UC-1 is too large. However, the formation energy of the Zn-Al antisite at certain positions can be reduced to below 0.96 eV in the case of UC-2, indicating that it is possible to form a small amount of Zn-Al antisite due to local structural distortion by Mg^{2+}/Ge^{4+} doping. Meanwhile, the formation energy of the Zn-Mg antisite is only 0.46 eV, while that of the Zn-Ge antisite is approximately 1.34-1.37 eV. These results indicate that Zn-Mg antisite is easily formed, but Zn-Ge antisite hardly exists. The behavior of antisite defect configurations obtained via DFT theoretically proves the correctness of the XRD Rietveld structure refinement results, although a small percentage of Zn-Al antisite is ignored when Mg^{2+}/Ge^{4+} doping occurs. Additionally, these antisite configurations prefer to form more stable antisite pairs rather than isolated antisites [18]. Therefore, Mg^{2+}/Ge^{4+} doping effectively generates more Zn-Mg and a few Zn-Al antisite defects in $ZnAl_2O_4$, leading to the formation of $Mg_{Al}^{'} - Ge_{Al}^{\bullet}$ and $Zn_{Al}^{'} - Ge_{Al}^{\bullet}$ defect clusters. This phenomenon agrees with previous findings of Zhu et al. on the structure evolution in $ZnGa_2O_4$ codoped with Mg^{2+}/Ge^{4+} [30, 31]. The luminescent chromium dopants always preferentially occupy the distorted octahedral site [18]. The insertion of antisite defect clusters provides a severe distortion of the local environment for Cr^{3+}, which influences the emission of Cr^{3+} and contributes to the persistent luminescence. As previously published, the emission intensity of Cr^{3+} can be increased by replacing Mg^{2+} with alkaline-metal atoms (Ca, Sr, Ba) in $Mg_7Ga_2GeO_{12}:Cr^{3+}$ [47], and the afterglow of $ZnGa_2O_4:Cr^{3+}$ can be improved through Sn^{4+} partially replacing Ga^{3+} [48].

3.2. Photoluminescence and persistent luminescence properties

The diffuse reflectance (DR) spectra of the ZAMG:Cr^{3+} (x = 0-0.6) phosphors are shown in Fig. 4a, while the bandgap energies of the samples were estimated from the

DR spectra of ZAMG (Fig. 4b). All the samples have three characteristic absorption bands at 273 nm (near ultraviolet region, $^4A_2 \rightarrow CB$), 387 nm (ultraviolet region, $^4A_2 \rightarrow {}^4T_1$ (^4F)), and 535 nm (visible region, $^4A_2 \rightarrow {}^4T_2$) [49]. Mg^{2+}/Ge^{4+} doping yields enhanced intensity of the absorption bands, indicating that Mg^{2+}/Ge^{4+} doping contributes to the increased absorption of ultraviolet and visible light. A redshift of the latter two bands is found by increasing the Cr^{3+} concentration. The optical bandgap energy (E_g) of the ZAMG (x = 0-0.6) host can be calculated by the Kubelka-Munk formula [50, 51]:

$$F(R)=\frac{K}{S}=\frac{(1-R)^2}{2R} \quad (2)$$

$$[F(R)\times h\nu]^2=A(h\nu-E_g) \quad (3)$$

where K, S, R, A, $h\nu$, and E_g are the molar absorption coefficient, scattering factor, diffuse reflectance, absorption constant, incident photon energy, and bandgap energy, respectively. The calculated E_g of the ZAMG host gradually decreases from 4.15 eV to 4.06 eV along with the increase in the x value, illustrating that Mg^{2+}/Ge^{4+} doping results in a narrower bandgap. To investigate the change in the electronic band structure of $ZnAl_2O_4$ and $ZnAl_2O_4$ with low and high concentrations of Mg^{2+}/Ge^{4+} doping, the total and partial density of states (DOS) of UC-1, UC-2, and UC-3 (Fig. 3a-c) are calculated by density functional theory and plotted in Fig. 4c-e. For $ZnAl_2O_4$ in Fig. 4c, the valence band (VB) in the lower part is mainly composed of the hybridization of Zn 3d, Al 3s, Al 3p, and O 2p states, while the conduction band (CB) in the upper part has major contributions from Al 3s and Al 3p states. The composition of the electronic structure of $ZnAl_2O_4$ after Mg^{2+}/Ge^{4+} doping still originates predominantly from the states of Al, Zn, and O, as shown in Fig. 4d. As the concentration of Mg^{2+}/Ge^{4+} increases until Al^{3+} is completely replaced, the CB and VB are affected by the states of Ge (Fig. 4e), resulting in significant changes in the band gap. The calculated band gaps for UC-1, UC-2, and UC-3 are 3.82, 3.50, and 2.48 eV, respectively, which are close to that reported earlier of 3.8-3.9 eV [52, 53]. However, the calculated values are always smaller than the values measured from the optical reflectivity experiment since the standard DFT exchange-correlation function greatly underestimates the size of the band

gap [37]. Above all, the band gaps calculated by DFT-GGA are in good agreement with the experimental values from the UV−vis analysis. All of the results demonstrate that the band gap decreases with increasing Mg^{2+}/Ge^{4+} doping.

Fig. 5 shows the photoluminescence excitation (PLE) and emission (PL) spectra of the ZAMG:Cr^{3+} samples (x = 0-0.6) at room temperature. The PLE spectra monitored at 686 nm contain two strong excitation bands centered at 387 nm and 530 nm, which are attributed to the $^4A_2 \rightarrow {}^4T_1$ (^4F) and $^4A_2 \rightarrow {}^4T_2$ transitions of Cr^{3+} ions (Fig. 5a) [22, 54]. Moreover, the asymmetric broad band at 394 nm can be regarded as the overlap of two bands at 390 nm and 414 nm. These two peaks originate from the energy level splitting in the trigonal crystal field and under the spin-orbit effect and correspond to $^4A_2(^4F) \rightarrow {}^4E(^4T_1(^4F))$ and $^4A_2(^4F) \rightarrow {}^4A_2(^4T_1(^4F))$ transitions [32, 55]. The band at approximately 252 nm ascribed to the transition of $^4A_2 \rightarrow$CB shifts to lower energy with increasing x, which is consistent with the reduction in the band gap of ZAMG (x = 0-0.6) [23, 24, 56]. It is worth noting that the peaks of the PLE spectra exhibit an obvious redshift with increasing x value. This shift can be ascribed to the weakening of the crystal field with increasing Mg^{2+}/Ge^{4+} co-doping [27]. The dominating emission lines at 686 nm in the PL spectra for all samples are related to the spin-forbidden $^2E \rightarrow {}^4A_2$ transition of Cr^{3+} in the octahedral crystal field under excitation at 530 nm or 387 nm (Figs. 5b and c). The zero phonon R lines at 686 nm are associated with Cr^{3+} in undistorted octahedral sites, while the N1 (~689 nm) and N2 (~694 nm) lines correspond to Cr^{3+} neighboring one certain defect [19, 20]. As previously reported, the N1 line may correspond to Cr^{3+} close to $Zn_{Al}^{'}$ and $Ge_{Al}^{\cdot}$ antisite defects (referred to as Cr_{N1}), and the N2 line is assigned to Cr^{3+} adjoining $Mg_{Al}^{'}$ and $Ge_{Al}^{\cdot}$ antisite defects as the first cationic neighbor (Cr_{N2}) [19, 22, 30]. However, the N1 and N2 lines are too low to detect for the x = 0 sample, which is due to the lack of intrinsic antisite defects ($Zn_{Al}^{'}$ and $Al_{Zn}^{\cdot}$) [19, 20]. The R lines are always accompanied by the Stokes phonon side bands (PSB, 706-721 nm) and anti-Stokes PSB (648-683 nm). Remarkably, the relative intensity of the R line becomes weaker than that of the N1 and N2 lines with an incremental substitution of Mg^{2+}-Ge^{4+}, and the latter emerges as a dominating influence in the emission spectra, as shown in Fig. 5d. Another interesting finding is

that the emission band of the $^2E \rightarrow {}^4A_2$ transition becomes broader than that of the sample without Mg^{2+}-Ge^{4+} co-doping. The FWHM of the emission band increases from 34 nm to 79 nm with an increase in *x* (Fig. S2 and Fig. 5d). This phenomenon can be interpreted to arise from the increasing disorder of Cr^{3+} ions induced by Mg^{2+}-Ge^{4+} incorporation [22]. In addition, the peak at approximately 704 nm (denoted by N4) is assigned to Cr^{3+}-Cr^{3+} pairs in the samples with sufficiently high Cr^{3+} concentrations accompanied by its phonon-sidebands in the range of 727-750 nm [32]. The results of Zhang et al. [32] and Jia et al. [33] suggested the presence of coupling Cr-Cr pairs in the spinel lattice when the Cr^{3+} ion concentration was above 0.5% through high-resolution XPS spectra of Cr 2p and EPR.

To further elucidate the luminescence mechanism of Cr^{3+}, the high-resolution PLE and PL spectra of the ZAMG:Cr^{3+} samples were obtained at 77 K. From the PLE and the normalized PLE spectra in Figs. 6a and c, there is a distinct redshift from 527 nm to 545 nm as the *x* value increases from 0 to 0.6. The luminescence of Cr^{3+} is easily affected by the crystal field environment; as a result, the redshift of PLE may be related to the change in the crystal field and nephelauxetic effect caused by Mg^{2+}-Ge^{4+} co-doping. The crystal field intensity *Dq*/*B* is determined by using the following formula [14]:

$$\Delta E = E\ (^4A_2 \rightarrow {}^4T_1) - E\ (^4A_2 \rightarrow {}^4T_2) \quad (4)$$

$$\Delta S = E\ (^4A_2 \rightarrow {}^4T_2) - E\ (^4T_2 \rightarrow {}^4A_2) \quad (5)$$

$$10 \times D_q = E\ (^4A_2 \rightarrow {}^4T_2) - \Delta S/2 \quad (6)$$

$$\frac{Dq}{B} = \frac{15(x\text{-}8)}{x^2\text{-}10x} \quad (7)$$

$$x = \frac{\Delta E}{Dq} \quad (8)$$

where *Dq* is the crystal field parameter and *B* is the Racah electron repulsion parameter. According to Figs. 6a and b, the values of ΔE (the energy difference between $^4A_2 \rightarrow {}^4T_1$ and $^4A_2 \rightarrow {}^4T_2$), ΔS (the Stokes shift), and *Dq*/*B* are calculated and summarized in Table 3. The calculated value of *Dq*/*B* for the $x = 0$ sample is 2.42, reflecting that Cr^{3+} ions are in a strong crystal field. By comparison, the values of *Dq*/*B* for $x = 0.1$, 0.2, 0.3, 0.4, 0.5, and 0.6 are relatively low, which implies that the crystal field of Cr^{3+}

becomes weaker at a higher Mg^{2+}/Ge^{4+} concentration. The weakening crystal field of Cr^{3+} in ZAMG is presented with the help of the Tanabe-Sugano diagram (Fig. S3). It is well known that Cr^{3+} generates narrowband emission (~700 nm) due to $^2E \rightarrow {}^4A_2$ in the high field (Dq/B>2.3), while Cr^{3+} exhibits broadband emission (650-1600 nm) arising from $^4T_2 \rightarrow {}^4A_2$ in the low field (Dq/B<2.3). Among previous reports, the $^2E \rightarrow {}^4A_2$ and $^4T_2 \rightarrow {}^4A_2$ luminescence transitions occurred simultaneously in Cr^{3+}-doped gallogermanate with an intermediate crystal field [25, 26]. By comparing the measured band shapes with those given in the references [25, 26], the broad emission at approximately 720 nm can be assigned to the $^4T_2 \rightarrow {}^4A_2$ transition. The PL intensity of the $^4T_2 \rightarrow {}^4A_2$ transition increases with increasing x values at RT and 77 K because the weaker the crystal field is, the higher the transition probability of the $^4T_2 \rightarrow {}^4A_2$ transition. In addition, the PL intensity ratios of the as-measured N1/R and N2/R lines as a function of x are shown in Fig. 6d. The R line of the ZAMG:Cr^{3+} sample (x = 0) is strong, while the N1 and N2 lines can be ignored. With the increase in x, the N1 and N2 lines become stronger and wider, and in the case of higher x values, the N2 line gradually dominates. This phenomenon indicates that the antisite defect clusters $Zn_{Al}^{'}$-Cr^{3+}-$Ge_{Al}^{\cdot}$ and $Mg_{Al}^{'}$-Cr^{3+}-$Ge_{Al}^{\cdot}$ significantly increase due to the incorporation of Mg^{2+}-Ge^{4+}, which would enhance the inversion disorder of the host [19, 20, 57]. Generally, the resulting defect clusters and increasing disorder remarkably improve the persistent luminescence.

Table 3 Crystal field parameters of ZAMG:Cr^{3+} samples (x = 0-0.6) at 77 K.

Sample	$E(^4A_2 \rightarrow {}^4T_1)$ (cm^{-1})	$E(^4A_2 \rightarrow {}^4T_2)$ (cm^{-1})	$E(^4T_2 \rightarrow {}^4A_2)$ (cm^{-1})	ΔE (cm^{-1})	ΔS (cm^{-1})	Dq	B	Dq/B
x = 0	25840	18975	14556	6864	4419	1677	692	2.42
x = 0.1	25840	18939	14556	6900	4383	1675	697	2.40
x = 0.2	25840	18832	14556	7007	4276	1669	713	2.34
x = 0.3	25773	18762	14556	7011	4206	1666	714	2.33
x = 0.4	25641	18553	14556	7088	3997	1655	727	2.28
x = 0.5	25575	18416	14556	7159	3860	1649	738	2.23
x = 0.6	25510	18349	14556	7162	3793	1645	739	2.22

In addition to the broad NIR photoluminescence, intense and long persistent NIR luminescence can be observed from the high levels of the Mg^{2+}-Ge^{4+} substituted

samples after removal of the excitation source. Fig. 7a shows the NIR afterglow decay time and persistent luminescence curves of the ZAMG:Cr^{3+} samples (x = 0-0.6) monitored at 686 nm after irradiation by UV light for 10 min. After 1500 s of decay, the persistent luminescence intensity remains 10 times that of the background for the sample with x = 0.4. This result indicates that the NIR afterglow of ZAMG:Cr^{3+} samples (x = 0.4-0.6) can last much longer than 1500 s. The Mg^{2+}-Ge^{4+} co-doping can significantly improve the afterglow performance of ZAO:Cr^{3+}, and with increasing Mg^{2+}-Ge^{4+} concentration, the afterglow intensity and decay time of ZAMG:Cr^{3+} increase. The long persistent NIR afterglow of ZAMG:Cr^{3+} (x = 0.4-0.6) phosphors is further confirmed by a night vision device, as shown in Fig. 7b. The x = 0.6 sample exhibits the best persistent NIR luminescence, which can last longer than 30 min. To further elucidate the variation in the trap after Mg^{2+}-Ge^{4+} substitution, the thermoluminescence (TL) spectra of the ZAMG:Cr^{3+} samples (x = 0.1-0.6) were obtained, as shown in Fig. 7c. Both the shape and the maximum temperature of the TL glow curves are significantly affected by increasing Mg^{2+}-Ge^{4+} content (Fig. S4). Apparently, with increasing Mg^{2+}-Ge^{4+} content, the entire glow curves progressively shift toward lower temperatures, except for x = 0; this may indicate that the trap depth can become shallow, resulting in a lower thermal energy needed to release the trapped charges and thus a longer afterglow. The trap depths were evaluated by the following general order kinetic equation [58, 59]:

$$I(T)=sn_0 \exp\left\{-\frac{E_t}{kT}\right\} \times \left[\frac{(b\text{-}1)s}{\beta}\int_{T_0}^{T} \exp\left\{-\frac{E_t}{kT}\right\} dT+1\right]^{-\frac{b}{(b\text{-}1)}} \quad (9)$$

where s is the frequency factor, n_0 is the initial number of trapped electrons after irradiation, E_t is the trap depth, k is Boltzmann's constant, β is the heating rate (1 K/s for this experiment), b is the kinetic order, and T is the absolute temperature. Considering that there are three possible defects in ZAMG:Cr^{3+}, resulting in close but different trap levels, three trap components have been added to fit these asymmetric glow curves. According to this general order kinetic equation, the accumulation peak of the fit curve (red line) agrees with the experimental data (black line), as shown in Fig. 7c. The trap depth E_t and initial number of trapped electrons n_0 of the three trap

components are listed in Table 4, and the main fitting parameters are summarized in Table S6. The fitted data of kinetic order *b* for all samples are in the range of 1~2, which could suggest that the kinetic processes are not pure first-order or second-order, but rather general order kinetic processes. Based on the general order kinetic equation, three traps with trap depths E_t of ~0.8 eV, ~0.7 eV, and ~0.5 eV are obtained. When the Mg^{2+}-Ge^{4+} content contains a low level, the initial number of trapped electrons n_0 of trap 1 is high, indicating that it corresponds to a large number of certain defects. It seems probable that trap 1 is related to the reported intrinsic defects in $ZnAl_2O_4$, such as V_O^+ and V_O^{2+} [60]. With increasing Mg^{2+}-Ge^{4+} co-doping concentration, the n_0 of trap 2 first increases and then decreases. Trap 2 is more likely to correspond to $Al_{Zn}^{\cdot}$ defects caused by Zn-Al antisites, as the number of such defects does not always increase but remains at a certain level at high Mg^{2+}-Ge^{4+} concentrations. Notably, the proportion of n_0 of trap 3 in that of the three traps gradually increases as the *x* value increases. Trap 3 may be attributed to the major $Ge_{Al}^{\cdot}$ defects formed by Mg^{2+}-Ge^{4+} co-doping. This significantly improves the probability of carrier capture by the $Ge_{Al}^{\cdot}$ defects related to trap 3 due to its shallower trap depth E_t; it can enhance the afterglow level and reduce the photoluminescence intensity of ZAMG:Cr^{3+} phosphors [61]. At the same time, the E_t of all three traps slowly decreases with increasing *x* from 0 to 0.6, possibly due to a decrease in the band gap. According to the above results, the mechanism diagram of luminescence and afterglow for ZAMG:Cr^{3+} phosphors is presented in Fig. 7d. For *x* = 0 samples, the electrons of Cr^{3+} in ZAO:Cr^{3+} are pumped from the ground state level $^4A_{2g}$ to the excited state levels $^4T_{2g}$, $^4T_{1g}$, and conduction band (CB), then transferred to the ^2E_g level *via* non-radiative relaxation, and finally returned back to the $^4A_{2g}$ level, which has a good NIR light output. The content of the defects associated with trap 1 in ZAO:Cr^{3+} is very low and has no ability to trap electrons, so the ZAO:Cr^{3+} phosphor exhibits no afterglow. For other samples, a portion of the electrons is trapped by trap2 and trap3 *via* CB after excitation to CB. When irradiation is stopped, the recombination of the de-trapping electrons occurs *via* CB or through a thermal tunneling process. Meanwhile, the PLE spectra exhibit a distinct redshift with an increased *x* value. This phenomenon can be explained by using the Tanabe-Sugano energy-level diagram (Fig.

S3), which proves that the existence of broad NIR emission corresponds to the $^4T_2 \rightarrow {}^4A_2$ transition in the ZAMG:Cr^{3+} (x = 0.6) phosphor.

Table 4 Fitting results of TL curves of ZAMG:Cr^{3+} samples (x = 0.1-0.6).

Sample	Trap1		Trap2		Trap3		Proportion of trap 3
	E_t (eV)	n_0	E_t (eV)	n_0	E_t (eV)	n_0	
x = 0.1	0.87	6.47×10^5	0.73	1.50×10^5	0.57	2.71×10^4	3.29%
x = 0.2	0.84	4.24×10^5	0.69	8.81×10^5	0.54	2.10×10^5	13.88%
x = 0.3	0.83	1.28×10^5	0.68	7.63×10^5	0.53	5.01×10^5	35.99%
x = 0.4	0.82	1.33×10^5	0.67	3.16×10^5	0.52	7.29×10^5	61.86%
x = 0.5	0.80	4.48×10^4	0.66	1.55×10^5	0.52	9.06×10^5	81.93%
x = 0.6	0.80	3.25×10^4	0.65	1.15×10^5	0.51	7.12×10^5	82.82%

To further broaden the PL emission of ZAMG:Cr^{3+}, the concentration of Cr^{3+} was increased when fixing the Mg^{2+}-Ge^{4+} concentration to increase the Cr^{3+} at the distorted sites. The normalized PLE and PL spectra of ZAO:Cr^{3+} (y = 1-2) and ZA$(MG)_{0.4}$:Cr^{3+} (z = 1-2) are displayed in Fig. S5, Figs. 8a and b. When the Cr^{3+} concentration increases from 1 at.% to 2 at.%, the intensity of the PL spectra ranging from 730 to 750 nm shows a continuous increase. By referring to the previous results [32,33], it can be seen that the emission of N4 (704 nm) and its phonon-sidebands (727-750 nm) should result from the interaction between Cr-Cr pairs. On the one hand, the emission bands at 704 nm and 727-750 nm corresponding to N4 and its PSB become broader with the increase in the concentration of Cr^{3+} for ZAO:Cr^{3+} (y = 1-2). This phenomenon may have resulted from the increase in the Cr^{3+}-Cr^{3+} pairs [32]. On the other hand, the PL emission peaks further become the connected band as the Cr^{3+} concentration increases for ZA$(MG)_{0.4}$:Cr^{3+} (z = 1-2), which can be caused by some possible reasons. First, the peaks at N1 (~689 nm) and N2 (~694 nm) broaden due to the appearance of Cr^{3+} neighboring the antisite defect clusters of $Zn_{Al}^{'}$-Cr^{3+}-$Ge_{Al}^{\cdot}$ and $Mg_{Al}^{'}$-Cr^{3+}-$Ge_{Al}^{\cdot}$ with the [Mg^{2+}-Ge^{4+}] unit replacing the [Al^{3+}-Al^{3+}] unit. Subsequently, the addition of Cr^{3+} may not only form Cr^{3+}-Cr^{3+} pairs, but also significantly increase the probability of adjacent antisite defect clusters of Cr^{3+}, thus widening N4 and the PSB of the N4. Then, the broadened emission at 720-800 nm assigned to the $^4T_2 \rightarrow {}^4A_2$ transition is due to the

weakened crystal field strength caused by Mg^{2+}-Ge^{4+} substitution [25, 26]. In conclusion, the broad-band emission of $ZA(MG)_{0.4}:Cr^{3+}$ can be comprehensively ascribed to the substitution-induced and high content Cr^{3+} causing an increase in Cr^{3+} at distorted sites. As shown in Fig. S6 and Fig. 8c, the FWHM of the overall emission of $ZA(MG)_{0.4}:Cr^{3+}$ changes from 44 nm to 95 nm.

The luminescence thermal stability is vital to assess the practicability of pc-LED devices since the junction temperature is usually above 388 K. Thus, the temperature-dependent PL spectra of $ZAMG:Cr^{3+}$ (x = 0.2, 0.4) and $ZA(MG)_{0.4}:Cr^{3+}$ (z = 2) phosphors under excitation at 394 nm were measured from 298 K to 573 K, as depicted in Fig. S7 and Fig. 8d. Due to the thermal quenching effect, the PL intensity of the $ZAMG:Cr^{3+}$ (x = 0.2, 0.4) phosphors decreases at higher heating temperatures. A special point to note is that the emission intensity of $ZA(MG)_{0.4}:Cr^{3+}$ (z = 2) at the R line (686 nm) is slightly greater than 100% in the temperature range of 323-398 K and then gradually decreases with a further increase in temperature, which proves the satisfactory thermal stability of this phosphor. Such a negative thermal quenching phenomenon can be attributed to the direct energy transfer from the defect states and the high efficiency of capturing carriers for the trap centers [62, 63]. The thermal ionization of Cr^{3+} 3d electrons entering the CB of the host could be partially compensated by the captured electrons detrapped from the shallow trap state at high temperature, which results in enhanced thermal stability. In addition, the multi-phonon relaxation caused by lattice vibration is the main reason for the decrease in the PL intensity at high temperatures [6]. To assess the thermal quenching behavior, the activation energy (E_a) was analyzed based on the Arrhenius equation [64]:

$$I_K = \frac{I_0}{1+A\exp(-\frac{\Delta E_a}{kT})} \tag{10}$$

where I_K and I_0 represent the PL intensity at the given temperature and 298 K, respectively. A is the constant related to the host, and k stands for the Boltzmann constant (8.629×10^{-5} eV). The value of E_a could be obtained by linear fitting of $\mathrm{Ln}(I_0/I_K\text{-}1)$ *vs*. $1/kT$. The E_a values of the $ZAMG:Cr^{3+}$ (x = 0.2, 0.4) and $ZA(MG)_{0.4}:Cr^{3+}$ (z = 2) phosphors are determined to be 0.216, 0.238, and 0.453 eV (Fig. S8 and Fig. 8e),

which is consistent with the higher quenching temperature of luminescence of the latter. As shown in Fig. 8f, the $ZA(MG)_{0.4}:Cr^{3+}$ (z = 2) sample shows a better thermal stability compared with the other two samples, and the integral PL intensity at 398 K can maintain 101% of the initial intensity at 298 K. For the $ZA(MG)_{0.4}:Cr^{3+}$ (z = 2) sample, the probability that electrons trapped in shallow traps tunnel into the Cr^{3+} center and recombine with holes increases, due to the high content of Cr^{3+} [62]; this may be the reason why only the $ZA(MG)_{0.4}:Cr^{3+}$ (z = 2) sample exhibits a negative thermal quenching phenomenon. This result indicates that the $ZA(MG)_{0.4}:Cr^{3+}$ (z = 2) phosphor is more suitable for pc-LEDs.

3.3. Application for the NIR pc-LED device

A NIR pc-LED device was constructed by combining the optimized $ZA(MG)_{0.4}:Cr^{3+}$ (z = 2) phosphor with a 395 nm ultraviolet LED chip. Fig. 9a depicts the electroluminescence (EL) spectra of the prepared pc-LED under various driving currents, and the insets show the images of pc-LED in both current on and off states. With the rise of the driving currents from 10 to 60 mA, the emission intensity gradually increases. The NIR output power of the fabricated devices is 19 mW at an input current of 100 mA with an electro-optical conversion efficiency of 7.7%. Due to more Cr^{3+} located in distorted sites in $ZA(MG)_{0.4}:Cr^{3+}$ (z = 2), the as-prepared NIR pc-LED has broadband emission that can cover the NIR-Ⅰ region from 700 to 900 nm. By utilizing the remarkable penetration ability of NIR light, non-destructive detection can be conducted on fruits, such as apples, to detect internal bruises caused by collision or extrusion during packaging and transportation (Fig. 9b). Using a fluorescent lamp as the light source, the printed words of all colors can be observed under a visible camera. However, only words with deep colors (deep red, blue, green, etc.) can be clearly detected by the NIR camera using the light source of the fabricated NIR pc-LED (Fig. 9c). Depending on this property, the NIR pc-LED can be applied as a lighting source for information encryption with the help of an NIR camera. For example, the barcodes representing “19230419” and “20230419” are printed in red and black words, respectively, and can be detected with different results under different light sources and cameras, as shown in Fig. 9d. Both types of barcodes and their overlapping information

can be clearly displayed under white light irradiation. The black barcode represents true information, while the red barcode indicates false information. The true information can be identified via the NIR camera under NIR pc-LED irradiation because black ink exhibits stronger absorption in the NIR than other colors. These phenomena strongly demonstrate the application prospects of the ZAMG:Cr^{3+} phosphor as an NIR pc-LEDs light source in non-destructive testing and anti-counterfeiting.

4. Conclusion

We developed a series of $ZnAl_{1.975-2x}Mg_xGe_xO_4$:1.25 at.% Cr^{3+} (ZAMG:Cr^{3+}, x = 0-0.7), $ZnAl_{2-0.02y}O_4$:y at.%Cr^{3+} (ZAO:Cr^{3+}, y = 1-2), and $ZnAl_{1.2-0.02z}Mg_{0.4}Ge_{0.4}O_4$:$z$ at.%Cr^{3+} (ZA$(MG)_{0.4}$:Cr^{3+}, z = 1-2) samples using high-temperature solid-state reaction. Substituting Mg^{2+}-Ge^{4+} for Al^{3+}-Al^{3+} contributes to the formation of distorted octahedral defect clusters of $Zn_{Al}^{'}$-Cr^{3+}-$Ge_{Al}^{\cdot}$ and $Mg_{Al}^{'}$-Cr^{3+}-$Ge_{Al}^{\cdot}$, which enhances the NIR emission intensity at the N1 and N2 lines and achieves long-lasting NIR persistent luminescence for ZAMG:Cr^{3+} phosphors. Moreover, the redshift of the excitation band and the simultaneous emission from the $^2E \rightarrow {}^4A_2$ and $^4T_2 \rightarrow {}^4A_2$ transitions are both due to the variation in crystal field strength by substitution. The introduced positive charged defects $Al_{Zn}^{\cdot}$ and $Ge_{Al}^{\cdot}$ serve as shallow traps, which can efficiently store and release excited electrons after radiation to obtain a long afterglow duration and negative thermal quenching. On the basis of co-substitution of [Mg^{2+}-Ge^{4+}], we further improved the concentration of Cr^{3+} ions. The high content of Cr^{3+} causes the formation of Cr^{3+}-Cr^{3+} pairs and a higher probability of adjoining antisite defects, which leads to a never-before-reported continuous broadband NIR emission of Cr^{3+}. By using this comprehensive strategy, the FWHM of the emission band was ultimately modulated from 34 nm (for $ZnAl_{1.975}O_4$:1.25 at.% Cr^{3+}) to 95 nm (for $ZnAl_{1.16}Mg_{0.4}Ge_{0.4}O_4$:2 at.% Cr^{3+}), in the absence of emission intensity loss in the range of 685-750 nm. We demonstrated that the NIR pc-LED prepared using the ZA$(MG)_{0.4}$:Cr^{3+} (z = 2) phosphor has a potential application in non-destructive analysis and anti-counterfeiting.

Declaration of competing interest

The authors declare that they have no known competing financial interests or personal relationships that could have appeared to influence the work reported in this paper.

Acknowledgements

This work was supported in part by the Fundamental Research Funds for the Central Universities (Grant N2302004), and National Natural Science Foundation of China (Grant 52371057, U21A2045, 52172112).

References

[1] F.Q. He, E.H. Song, Y.Y. Zhou, H. Ming, Z.T. Chen, J.C. Wu, P.S. Shao, X.F. Yang, Z.G. Xia, Q.Y. Zhang, A general ammonium salt assisted synthesis strategy for Cr^{3+}-doped hexafluorides with highly efficient near infrared emissions, Adv. Funct. Mater. 31 (36) (2021) 2103743. https://doi.org/10.1002/adfm.202103743.

[2] Y. Yan, M.M. Shang, S. Huang, Y.N. Wang, Y.X. Sun, P.P. Dang, J. Lin, Photoluminescence properties of $AScSi_2O_6:Cr^{3+}$ (A = Na and Li) phosphors with high efficiency and thermal stability for near-infrared phosphor-converted light-emitting diode light sources, ACS Appl. Mater. Inter. 14 (6) (2022) 8179-8190. https://doi.org/10.1021/acsami.1c23940.

[3] X.K. Zou, X.J. Wang, H.R. Zhang, Y.Y. Kang, X. Yang, X.J. Zhang, M.S. Molokeev, B.F. Lei, A highly efficient and suitable spectral profile Cr^{3+}-doped garnet near-infrared emitting phosphor for regulating photomorphogenesis of plants, Chem. Eng. J. 428 (2022) 132003. https://doi.org/10.1016/j.cej.2021.132003.

[4] W.T. Huang, C.L. Cheng, Z. Bao, C.W. Yang, K.M. Lu, C.Y. Kang, C.M. Lin, R.S. Liu, Broadband Cr^{3+}, Sn^{4+}-doped oxide nanophosphors for infrared mini light-emitting diodes, Angew. Chem. Int. Ed. 58 (7) (2019) 2069-2072. https://doi.org/10.1002/anie.201813340.

[5] V. Rajendran, W.T. Huang, K.C. Chen, H. Chang, R.S. Liu, Energy-saving chromium-activated garnet-structured phosphor-converted near-infrared light-emitting

diodes, J. Mater. Chem. C 10 (39) (2022) 14367-14378. https://doi.org/10.1039/D2TC02817D.

[6] Z.H. Zhou, F.Q. He, E.H. Song, S. Zhang, X.D. Yi, H. Zhang, Y.K. Le, S. Ye, S.H. Xu, J.R. Qiu, G.P. Dong, Broadband and multimode near-infrared emitter based on Cr^{3+}-activated stannate for multifunctional applications, Adv. Optical Mater. 11 (7) (2023) 2202466. https://doi.org/10.1002/adom.202202466.

[7] S. Huang, Y. Yan, M.M. Shang, Y.N. Wang, Y.X. Sun, P.P. Dang, J. Lin, Super broadband near-infrared solid solution phosphors with adjustable peak wavelengths from 1165 to 875 nm for NIR spectroscopy applications, Adv. Optical Mater. 11 (5) (2022) 2202291. https://doi.org/10.1002/adom.202202291.

[8] Z.B. Tang, F. Du, H. Liu, Z.H. Leng, X.Q. Sun, H.D. Xie, M.D. Que, Y.H. Wang, Eu^{2+}-doped layered double borate phosphor with ultrawide near-infrared spectral distribution in response to ultraviolet-blue light excitation, Adv. Optical Mater. 10 (5) (2022) 2102204. https://doi.org/10.1002/adom.202102204.

[9] F.Y. Zhao, Z. Song, Q.L. Liu, Advances in chromium-activated phosphors for near-infrared light sources, Laser Photon. Rev. 16 (11) (2022) 2200380. https://doi.org/10.1002/lpor.202200380.

[10] E.H. Song, X.X. Jiang, Y.Y. Zhou, Z.S. Lin, S. Ye, Z.G. Xia, Q.Y. Zhang, Heavy Mn^{2+} doped $MgAl_2O_4$ phosphor for high-efficient near-infrared light-emitting diode and the night-vision application, Adv. Optical Mater. 7 (24) (2019) 1901105. https://doi.org/10.1002/adom.201901105.

[11] X.X. Xu, Q.Y. Shao, L.Q. Yao, Y. Dong, J.Q. Jiang, Highly efficient and thermally stable Cr^{3+}-activated silicate phosphors for broadband near-infrared LED applications, Chem. Eng. J. 383 (2020) 123108. https://doi.org/10.1016/j.cej.2019.123108.

[12] M.Q. Mao, T.L. Zhou, H.T. Zeng, L. Wang, F. Huang, X.Y. Tang, R.J. Xie, Broadband near-infrared (NIR) emission realized by the crystal-field engineering of $Y_{3-x}Ca_xAl_{5-x}Si_xO_{12}:Cr^{3+}$ (x = 0-2.0) garnet phosphors, J. Mater. Chem. C 8 (6) (2020) 1981-1988. https://doi.org/10.1039/C9TC05775G.

[13] L.Q. Yao, Q.Y. Shao, M.L. Shi, T.Q. Shang, Y. Dong, C. Liang, J.H. He, J.Q. Jiang, Efficient ultra-broadband $Ga_4GeO_8:Cr^{3+}$ phosphors with tunable peak wavelengths

from 835 to 980 nm for NIR pc-LED application, Adv. Optical Mater. 10 (4) (2022) 2102229. https://doi.org/10.1002/adom.202102229.

[14] C.X. Yuan, R.Y. Li, Y.F. Liu, L.L. Zhang, J.H. Zhang, G. Leniec, P. Sun, Z.H. Liu, Z.H. Luo, R. Dong, J. Jiang, Efficient and broadband $LiGaP_2O_7:Cr^{3+}$ phosphors for smart near-infrared light-emitting diodes, Laser Photon. Rev. 15 (11) (2021) 2100227. https://doi.org/10.1002/lpor.202100227.

[15] M.U. Dumesso, W.G. Xiao, G.J. Zheng, E.T. Basore, M.X. Tang, X.F. Liu, J.R. Qiu, Efficient, stable, and ultra-broadband near-infrared garnet phosphors for miniaturized optical applications, Adv. Optical Mater. 10 (16) (2022) 2200676. https://doi.org/10.1002/adom.202200676.

[16] L.M. Fang, L.L. Zhang, H. Wu, H.J. Wu, G.H. Pan, Z.D. Hao, F. Liu, J.H. Zhang, Efficient broadband near-infrared $CaMgGe_2O_6:Cr^{3+}$ phosphor for pc-LED, Inorg. Chem. 61 (23) (2022) 8815-8822. https://doi.org/10.1021/acs.inorgchem.2c00798.

[17] K.E. Sickafus, J.M. Wills, N.W. Grimes, Structure of spinel, J. Am. Ceram. Soc. 82 (12) (1999) 3279-3292. https://doi.org/10.1111/j.1151-2916.1999.tb02241.x.

[18] A. De Vos, K. Lejaeghere, D.E.P. Vanpoucke, J.J. Joos, P.F. Smet, K. Hemelsoet, First-principles study of antisite defect configurations in $ZnGa_2O_4$:Cr persistent phosphors, Inorg. Chem. 55 (5) (2016) 2402-2412. https://doi.org/10.1021/acs.inorgchem.5b02805.

[19] N. Basavaraju, K.R. Priolkar, D. Gourier, S.K. Sharma, A. Bessière, B. Viana, The importance of inversion disorder in the visible light induced persistent luminescence in Cr^{3+} doped AB_2O_4 (A = Zn or Mg and B = Ga or Al), Phys. Chem. Chem. Phys. 17 (3) (2015) 1790-1799. https://doi.org/10.1039/C4CP03866E.

[20] N. Basavaraju, K.R. Priolkar, D. Gourier, A. Bessière, B. Viana, Order and disorder around Cr^{3+} in chromium doped persistent luminescent AB_2O_4 spinels, Phys. Chem. Chem. Phys. 17 (16) (2015) 10993-10999. https://doi.org/10.1039/C5CP01097G.

[21] X.D. Huang, X.J. Wei, Y. Zeng, L.H. Jing, H.R. Ning, X.D. Sun, Y.Y. Li, D. Li, Y.P. Yi, M.Y. Gao, Turning-on persistent luminescence out of chromium-doped zinc aluminate nanoparticles by instilling antisite defects under mild conditions, Nanoscale 13 (18) (2021) 8514-8523. https://doi.org/10.1039/D0NR08267H.

[22] Y. Zhang, R. Huang, H.L. Li, D.J. Hou, Z.X. Lin, J. Song, Y.Z. Guo, H.H. Lin, C. Song, Z.W. Lin, J. Robertson, Germanium substitution endowing Cr^{3+}-doped zinc aluminate phosphors with bright and super-long near-infrared persistent luminescence, Acta Mater. 155 (2018) 214-221. https://doi.org/10.1016/j.actamat.2018.06.020.

[23] Z.W. Pan, Y.Y. Lu, F. Liu, Sunlight-activated long-persistent luminescence in the near-infrared from Cr^{3+}-doped zinc gallogermanates, Nat. Mater. 11 (2012) 58-63. https://doi.org/10.1038/nmat3173.

[24] T. Maldiney, A. Bessière, J. Seguin, E. Teston, S.K. Sharma, B. Viana, A.J.J. Bos, P. Dorenbos, M. Bessodes, D. Gourier, D. Scherman, C. Richard, The *in vivo* activation of persistent nanophosphors for optical imaging of vascularization, tumours and grafted cells, Nat. Mater. 13 (2014) 418-426. https://doi.org/10.1038/nmat3908.

[25] M. Back, E. Trave, J. Ueda, S. Tanabe, Ratiometric optical thermometer based on dual near-infrared emission in Cr^{3+}-doped bismuth-based gallate host, Chem. Mater. 28 (22) (2016) 8347-8356. https://doi.org/10.1021/acs.chemmater.6b03625.

[26] J. Yang, Y.X. Liu, Y.Y. Zhao, Z. Gong, M. Zhang, D.T. Yan, H.C. Zhu, C.G. Liu, C.S. Xu, H. Zhang, Ratiometric afterglow nanothermometer for simultaneous *in situ* bioimaging and local tissue temperature sensing, Chem. Mater. 29 (19) (2017) 8119-8131. https://doi.org/10.1021/acs.chemmater.7b01958.

[27] Y. Li, Y.Y. Li, R.C. Chen, K. Sharafudeen, S.F. Zhou, M. Gecevicius, H.H. Wang, G.P. Dong, Y.L. Wu, X.X. Qin, J.R. Qiu, Tailoring of the trap distribution and crystal field in Cr^{3+}-doped non-gallate phosphors with near-infrared long-persistence phosphorescence, NPG Asia Mater. 7 (2015) e180. https://doi.org/10.1038/am.2015.38.

[28] Z.F. Pan, V. Castaing, L.P. Yan, L.L. Zhang, C. Zhang, K. Shao, Y.F. Zheng, C.K. Duan, J.H. Liu, C. Richard, B. Viana, Facilitating low-energy activation in the near-infrared persistent luminescent phosphor $Zn_{1+x}Ga_{2-2x}Sn_xO_4:Cr^{3+}$ *via* crystal field strength modulations, J. Phys. Chem. C 124 (15) (2020) 8347-8358. https://doi.org/10.1021/acs.jpcc.0c01951.

[29] S.Y. Li, Q. Zhu, X.D. Sun, J.G. Li, Magical polyhedral twist *via* chemical unit co-substitution in $LaAlO_3:Mn^{4+}$ to greatly enhance the zero phonon line for high-efficiency plant-growth LEDs, J. Mater. Chem. C 9 (22) (2021) 7163-7173.

https://doi.org/10.1039/D1TC01116B.

[30] Q. Zhu, J.Q. Xiahou, X.D. Li, X.D. Sun, J.G. Li, Defect cluster engineering in $ZnGa_{2-x}(Mg/Ge)_xO_4:Cr^{3+}$ nanoparticles for remarkably improved NIR persistent luminescence, J. Am. Ceram. Soc. 104 (9) (2021) 4594-4605. https://doi.org/10.1111/jace.17864.

[31] J.Q. Xiahou, Q. Zhu, L. Zhu, S.Y. Li, J.G. Li, Local structure regulation in near-infrared persistent phosphor of $ZnGa_2O_4:Cr^{3+}$ to fabricate natural-light rechargeable optical thermometer, ACS Appl. Electron. Mater. 3 (9) (2021) 3789-3803. https://doi.org/10.1021/acsaelm.1c00305.

[32] D. Zhang, Q.J. Guo, Y.F. Ren, C.Z. Wang, Q. Shi, Q.L. Wang, X. Xiao, W.J. Wang, Q.L. Fan, Influence of inversion defects and Cr-Cr pairs on the photoluminescent performance of $ZnAl_2O_4$ crystals, J Sol-Gel Sci Technol 85 (2018) 121-131. https://doi.org/10.1007/s10971-017-4527-4.

[33] Z.W. Jia, C.X. Yuan, Y.F. Liu, X.J. Wang, P. Sun, L. Wang, H.C. Jiang, J. Jiang, Strategies to approach high performance in Cr^{3+}-doped phosphors for high-power NIR-LED light sources, Light Sci. Appl. 9 (2020) 86. https://doi.org/10.1038/s41377-020-0326-8.

[34] P.E. Blöchl, Projector augmented-wave method, Phys. Rev. B 50 (24) (1994) 17953. https://doi.org/10.1103/PhysRevB.50.17953.

[35] G. Kresse, J. Furthmüller, Efficient iterative schemes for *ab initio* total-energy calculations using a plane-wave basis set, Phys. Rev. B 54 (16) (1996) 11169. https://doi.org/10.1103/PhysRevB.54.11169.

[36] G. Kresse, J. Furthmüller, Efficiency of ab-initio total energy calculations for metals and semiconductors using a plane-wave basis set, Comp. Mater. Sci. 6 (1) (1996) 15-50. https://doi.org/10.1016/0927-0256(96)00008-0.

[37] J.P. Perdew, K. Burke, M. Ernzerhof, Generalized gradient approximation made simple, Phys. Rev. Lett. 77 (18) (1996) 3865. https://doi.org/10.1103/PhysRevLett.77.3865.

[38] N. Kashii, H. Maekawa, Y. Hinatsu, Dynamics of the cation mixing of $MgAl_2O_4$ and $ZnAl_2O_4$ spinel, J. Am. Ceram. Soc. 82 (7) (1999) 1844-

1848. https://doi.org/10.1111/j.1151-2916.1999.tb02007.x.

[39] W.B. White, B.A. DeAngelis, Interpretation of the vibrational spectra of spinels, Spectrochim. Acta A 23 (4) (1967) 985-995. https://doi.org/10.1016/0584-8539(67)80023-0.

[40] P. Loiko, A. Belyaev, O. Dymshits, I. Evdokimov, V. Vitkin, K. Volkova, M. Tsenter, A. Volokitina, M. Baranov, E. Vilejshikova, A. Baranov, A. Zhilin, Synthesis, characterization and absorption saturation of Co:$ZnAl_2O_4$ (gahnite) transparent ceramic and glass-ceramics: a comparative study, J. Alloy. Compd. 725 (2017) 998-1005. https://doi.org/10.1016/j.jallcom.2017.07.239.

[41] I.P. Alekseeva, O.S. Dymshits, V.V. Golubkov, P.A. Loiko, M.Y. Tsenter, K.V. Yumashev, S.S. Zapalova, A.A. Zhilin, Influence of NiO on phase transformations and optical properties of ZnO-Al_2O_3-SiO_2 glass-ceramics nucleated by TiO_2 and ZrO_2. Part I. Influence of NiO on phase transformations of ZnO-Al_2O_3-SiO_2 glass-ceramics nucleated by TiO_2 and ZrO_2, J. Non-Cryst. Solids 384 (2014) 73-82. https://doi.org/10.1016/j.jnoncrysol.2013.05.038.

[42] A. Chopelas, A.M. Hofmeister, Vibrational spectroscopy of aluminate spinels at 1 atm and of $MgAl_2O_4$ to over 200 kbar, Phys. Chem. Minerals 18 (1991) 279-293. https://doi.org/10.1007/BF00200186.

[43] J.X. Wang, A.Q. Wang, D.M. Hu, X.L. Wu, Y. Liu, T.J. Chen, Synthesis, characterization and properties of Ni^{2+}-doped $ZnAl_2O_4$-based spinel-type solid acid catalysts: $SO_4^{2-}/Ni_xZn_{1-x}Al_2O_4$, Mater. Chem. Phys. 239 (2020) 122319. https://doi.org/10.1016/j.matchemphys.2019.122319.

[44] E. Ghanti, R. Nagarajan, Synthesis of $CuAl_2(acac)_4(O^iPr)_4$, its hydrolysis and formation of bulk $CuAl_2O_4$ from the hydrolyzed gels; a case study of molecules to materials, Dalton Trans. 39 (26) (2010) 6056-6061. https://doi.org/10.1039/B926579A.

[45] L. Malavasi, P. Galinetto, M.C. Mozzati, C.B. Azzoni, G. Flor, Raman spectroscopy of AMn_2O_4 (A = Mn, Mg and Zn) spinels, Phys. Chem. Chem. Phys. 4 (15) (2002) 3876-3880. https://doi.org/10.1039/B203520K.

[46] V. Mohaček-Grošev, M. Vrankić, A. Maksimović, V. Mandić, Influence of titanium doping on the Raman spectra of nanocrystalline $ZnAl_2O_4$, J. Alloy. Compd. 697 (2017)

90-95. https://doi.org/10.1016/j.jallcom.2016.12.116.

[47] J.M. Xiang, X. Zhou, X.Q. Zhao, Z.Y. Wu, C.H. Chen, X.J. Zhou, C.F. Guo, Ab initio site-selective occupancy and luminescence enhancement in broadband NIR emitting phosphor $Mg_7Ga_2GeO_{12}:Cr^{3+}$, Laser Photonics Rev. 17 (7) (2023) 2200965. https://doi.org/10.1002/lpor.202200965.

[48] J. Qin, J.M. Xiang, H. Suo, Y.H. Chen, Z.Y. Zhang, X.Q. Zhao, Y.F. Wu, C.F. Guo, NIR persistent luminescence phosphor $Zn_{1.3}Ga_{1.4}Sn_{0.3}O_4:Yb^{3+},Er^{3+},Cr^{3+}$ with 980 nm laser excitation, J. Mater. Chem. C 7 (38) (2019) 11903-11910. https://doi.org/10.1039/C9TC03882E.

[49] S.V. Motloung, F.B. Dejene, H.C. Swart, O.M. Ntwaeaborwa, Effects of Cr^{3+} mol% on the structure and optical properties of the $ZnAl_2O_4:Cr^{3+}$ nanocrystals synthesized using sol-gel process, Ceram. Int. 41 (5) (2015) 6776-6783. https://doi.org/10.1016/j.ceramint.2015.01.124.

[50] Q. Wu, P.L. Li, Z.J. Ye, X.X. Huo, H.F. Yang, Y. Wang, D.W. Wang, J.X. Zhao, Z.P. Yang, Z.J. Wang, Near-infrared emitting phosphor $LaMg_{0.5}(SnGe)_{0.5}O_3:Cr^{3+}$ for plant growth applications: crystal structure, luminescence, and thermal stability, Inorg. Chem. 60 (21) (2021) 16593-16603. https://doi.org/10.1021/acs.inorgchem.1c02474.

[51] Q. Wang, S.W. Wang, T. Tan, J.T. Wang, R. Pang, D. Li, C.Y. Li, H.J. Zhang, Efficient Cr^{3+}-activated $NaInP_2O_7$ phosphor for broadband near-infrared LED applications, Inorg. Chem. Front. 9 (15) (2022) 3692-3701. https://doi.org/10.1039/D2QI00794K.

[52] S.K. Sampath, J.F. Cordaro, Optical properties of zinc aluminate, zinc gallate, and zinc aluminogallate spinels, J. Am. Ceram. Soc. 81 (3) (1998) 649-654. https://doi.org/10.1111/j.1151-2916.1998.tb02385.x.

[53] S.K. Sampath, D.G. Kanhere, R. Pandey, Electronic structure of spinel oxides: zinc aluminate and zinc gallate, J. Phys.: Condens. Matter 11 (1999) 3635-3644. https://doi.org/10.1088/0953-8984/11/18/301.

[54] L. Xi, L. Pan, Y. Wang, P.D. Townsend, The influence of doped Cr ions on the luminescence properties of infrared long persistent phosphor $ZnAl_2O_4$ with the substitution of Ge ions, J. Lumin. 233 (2021) 117941.

https://doi.org/10.1016/j.jlumin.2021.117941.

[55] W. Nie, F.M. Michel-Calendini, C. Linares, G. Boulon, C. Daul, New results on optical properties and term-energy calculations in Cr^{3+}-doped $ZnAl_2O_4$, J. Lumin. 46 (3) (1990) 177-190. https://doi.org/10.1016/0022-2313(90)90038-D.

[56] Y.X. Zhuang, J. Ueda, S. Tanabe, P. Dorenbos, Band-gap variation and a self-redox effect induced by compositional deviation in $Zn_xGa_2O_{3+x}$:Cr^{3+} persistent phosphors, J. Mater. Chem. C 2 (28) (2014) 5502-5509. https://doi.org/10.1039/C4TC00369A.

[57] M. Allix, S. Chenu, E. Véron, T. Poumeyrol, E.A. Kouadri-Boudjelthia, S. Alahraché, F. Porcher, D. Massiot, F. Fayon, Considerable improvement of long-persistent luminescence in germanium and tin substituted $ZnGa_2O_4$, Chem. Mater. 25 (9) (2013) 1600-1606. https://doi.org/10.1021/cm304101n.

[58] R. Chen, Glow curves with general order kinetics, J. Electrochem. Soc. 116 (1969) 1254-1257. https://doi.org/10.1149/1.2412291.

[59] G. Kitis, J.M. Gomez-Ros, J.W.N. Tuyn, Thermoluminescence glow-curve deconvolution functions for first, second and general orders of kinetics, J. Phys. D: Appl. Phys. 31 (1998) 2636-2641. https://doi.org/10.1088/0022-3727/31/19/037.

[60] N. Pathak, P.S. Ghosh, S. Saxena, D. Dutta, A.K. Yadav, D. Bhattacharyya, S.N. Jha, R.M. Kadam, Exploring defect-induced emission in $ZnAl_2O_4$: an exceptional color-tunable phosphor material with diverse lifetimes, Inorg. Chem. 57 (7) (2018) 3963-3982. https://doi.org/10.1021/acs.inorgchem.8b00172.

[61] Z.F. Qiu, Y.Y. Zhou, M.K. Lü, A.Y. Zhang, Q. Ma, Combustion synthesis of long-persistent luminescent MAl_2O_4:Eu^{2+},R^{3+} (M = Sr, Ba, Ca, R = Dy, Nd and La) nanoparticles and luminescence mechanism research, Acta Mater. 55 (8) (2007) 2615-2620. https://doi.org/10.1016/j.actamat.2006.12.018.

[62] C. Wang, Y.Y. Cai, H. Zhang, Z.C. Liu, H.Y. Lv, X.D. Zhu, Y. Liu, C.C. Wang, J.B. Qiu, X. Yu, X.H. Xu, Variation from zero to negative thermal quenching of phosphor with assistance of defect states, Inorg. Chem. 60 (24) (2021) 19365-19372. https://doi.org/10.1021/acs.inorgchem.1c03188.

[63] Z. Zhou, H.F. Zhu, X. Huang, Y.L. She, Y. Zhong, J. Wang, M. Liu, W. Li, M. Xia, Anti-thermal-quenching, color-tunable and ultra-narrow-band cyan green-emitting

phosphor for w-LEDs with enhanced color rendering, Chem. Eng. J. 433 (2022) 134079. https://doi.org/10.1016/j.cej.2021.134079.

[64] S.Y. Lee, Y.H. Shin, Y. Kim, S. Kim, S. Ju, Thermal quenching behavior of emission bands in Eu-doped ZnS nanowires, J. Lumin. 131 (7) (2011) 1336-1339. https://doi.org/10.1016/j.jlumin.2011.03.026.

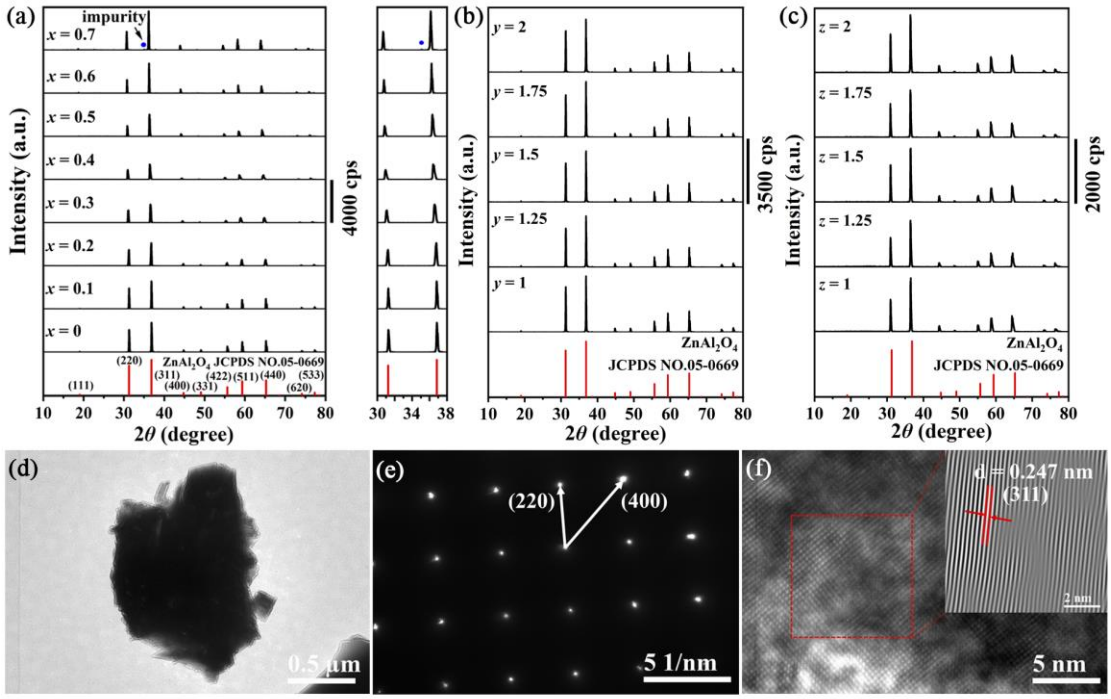

Fig. 1. XRD patterns for (a) $ZnAl_{1.975-2x}Mg_xGe_xO_4$:1.25 at.%$Cr^{3+}$ (x = 0-0.7) powders and enlarged XRD data within the 2θ range of 30-38°, (b) $ZnAl_2O_4$:y at.%Cr^{3+} (y = 1-2), and (c) $ZnAl_{1.2}Mg_{0.4}Ge_{0.4}O_4$:$z$ at.%Cr^{3+} (z = 1-2) powders calcined at 1500 ℃. The standard diffraction of $ZnAl_2O_4$ (JCPDS No.05-0669) is included as red vertical bars for comparison. (d) TEM image, (e) SAED pattern, and (f) HR-TEM image of the $ZnAl_{1.975-2x}Mg_xGe_xO_4$:1.25 at.% Cr^{3+} (x = 0.4) sample.

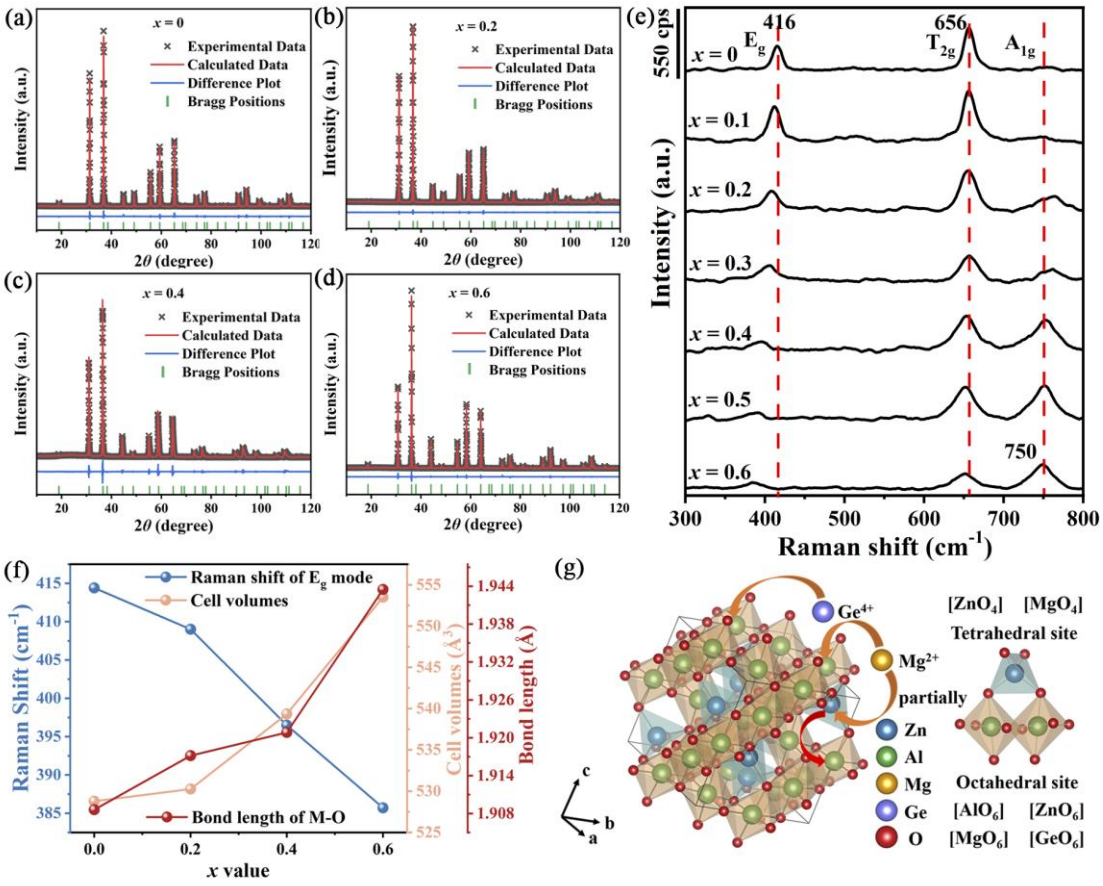

Fig. 2. The Rietveld refinements of the XRD patterns for the ZAMG:Cr^{3+} samples with different *x* values: (a) *x* = 0, (b) *x* = 0.2, (c) *x* = 0.4, and (d) *x* = 0.6. (e) Raman spectra for the ZAMG:Cr^{3+} samples (*x* = 0-0.6). (f) Raman shift of E_g mode, cell volume, and bond length of MO_6 (M = Al/Mg/Ge/Cr) octahedra evolution along with increased *x*. (g) Crystal structure of the $ZnAl_2O_4$ spinel, showing the occupancy of Mg^{2+}/Ge^{4+} and potential tetrahedral and octahedral coordinations.

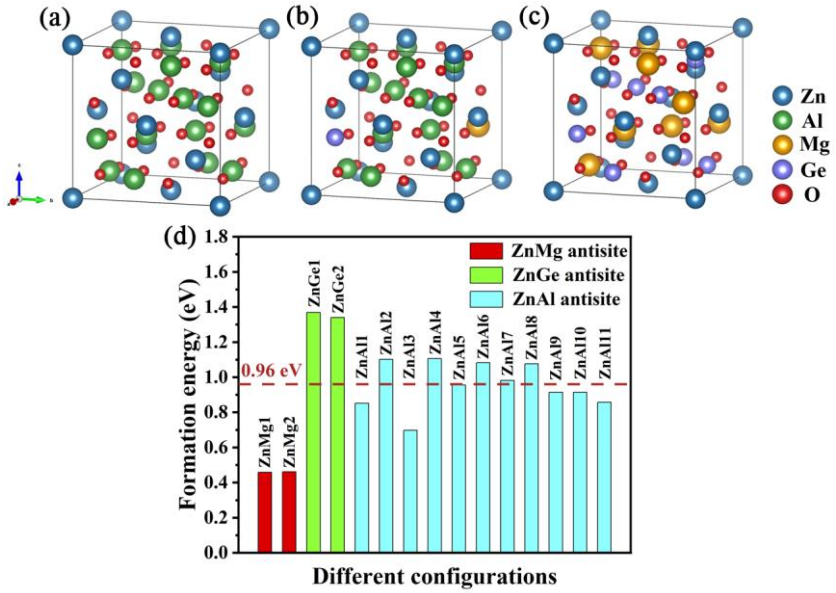

Fig. 3. Crystal structure of ZAMG with 56-atom unit cells: (a) UC-1, (b) UC-2, and (c) UC-3. (d) Calculated formation energies (ΔE_f) of potential antisite configurations in UC-2.

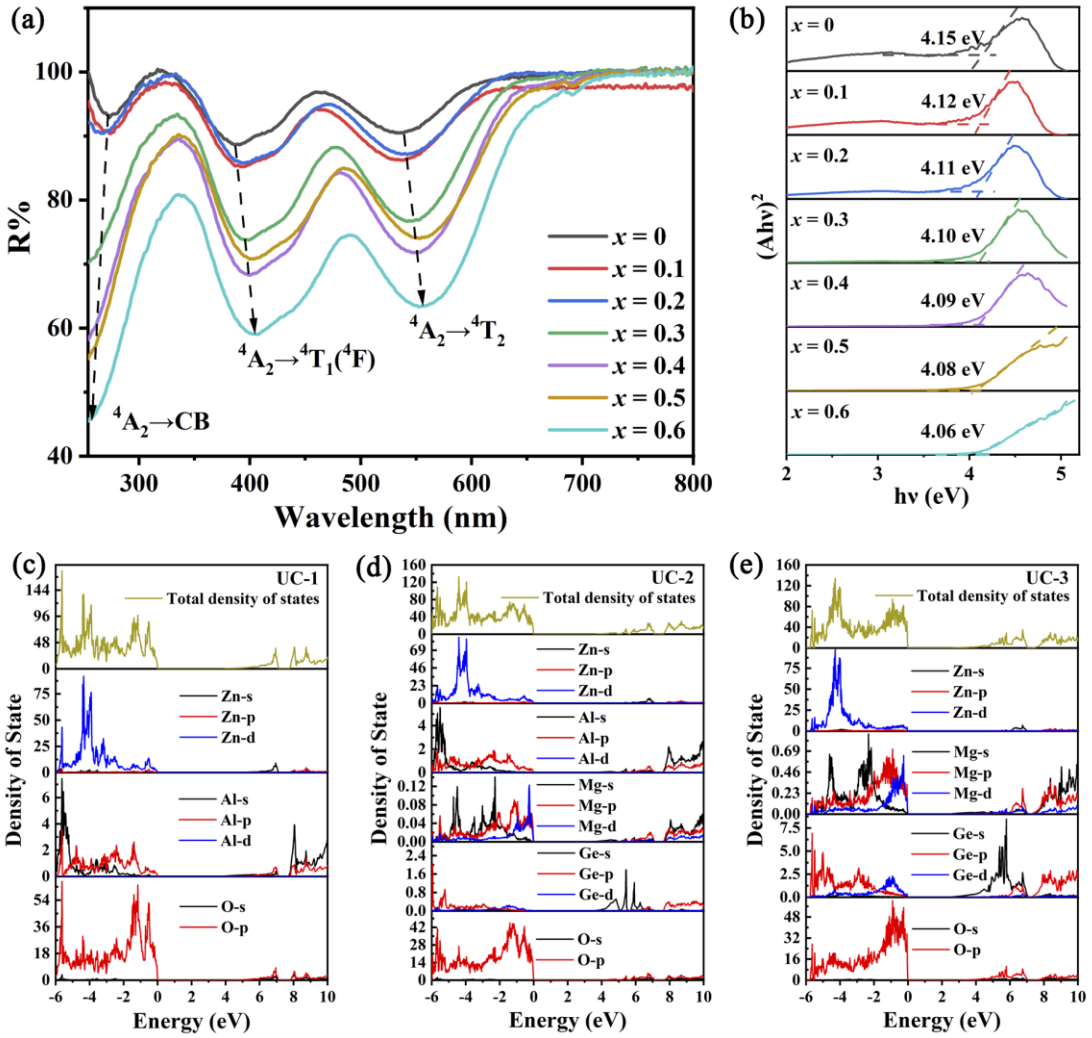

Fig. 4. (a) Diffuse Reflectance (DR) spectra of ZAMG:Cr^{3+} (x = 0-0.6) and (b) determination of bandgap energies for ZAMG (x = 0-0.6). Total and partial density of states (DOS) of $ZnAl_2O_4$ spinel with and without Mg^{2+}/Ge^{4+} doping: (c) UC-1, (d) UC-2, and (e) UC-3. The Fermi energy is used as zero energy.

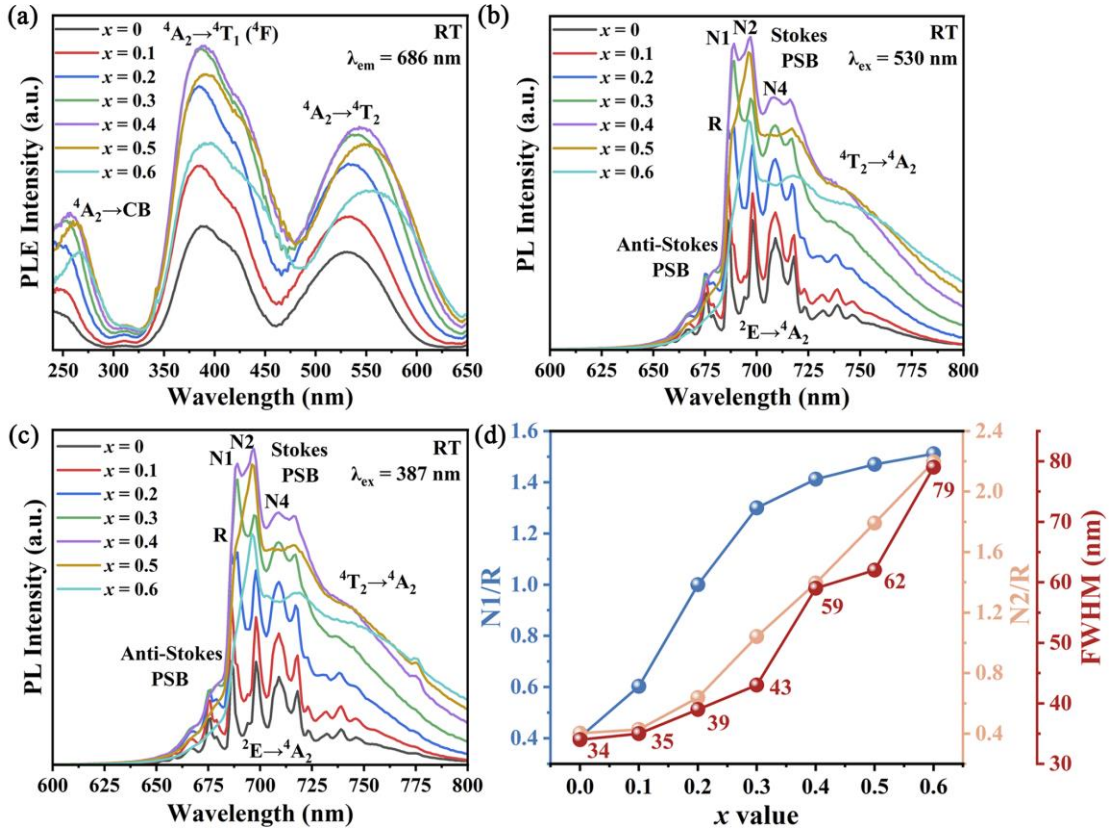

Fig. 5. (a) PLE and (b, c) PL spectra of the ZAMG:Cr^{3+} samples (x = 0-0.6) at room temperature. (d) The intensity ratios of the N1/R, N2/R lines, and FWHM of emission band obtained from normalized PL spectra of the ZAMG:Cr^{3+} samples (x = 0-0.6) under excitation at 387 nm.

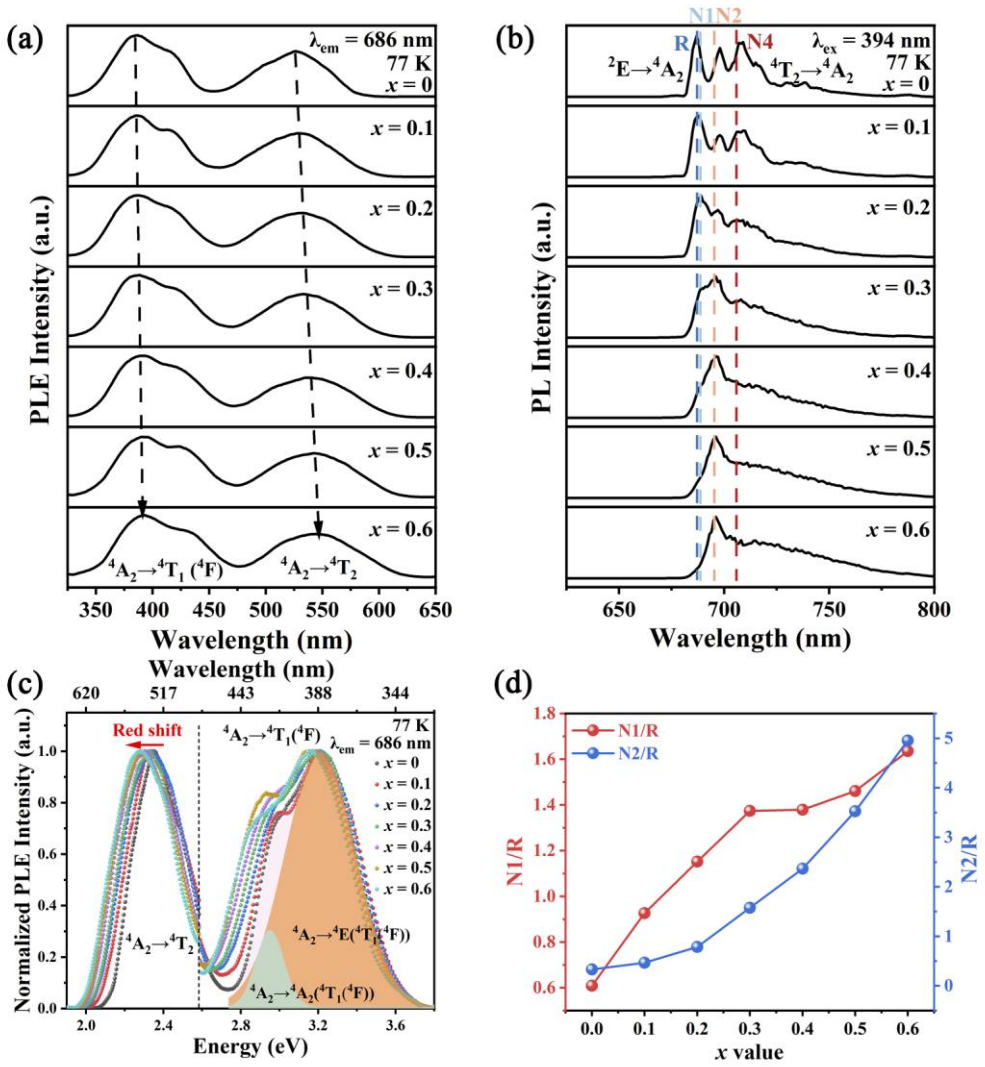

Fig. 6. (a) PLE and (b) PL spectra of the ZAMG:Cr^{3+} samples (x = 0-0.6) at 77 K. (c) The normalized PLE spectra from (a). (d) The intensity ratios of the N1/R and N2/R lines are taken as functions of x.

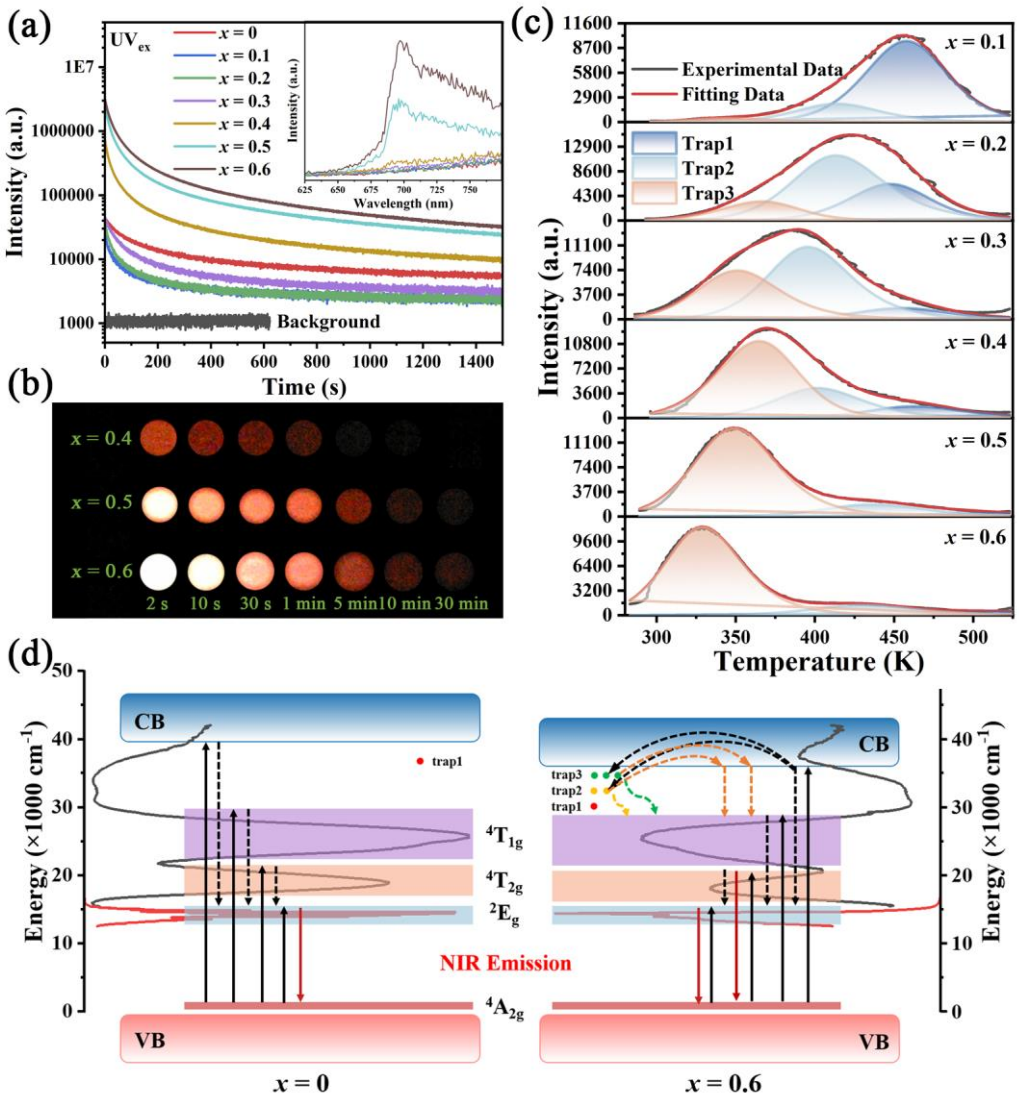

Fig. 7. (a) NIR-persistent luminescence decay curves, (b) NIR afterglow images, and (c) TL glow curves of the ZAMG:Cr^{3+} samples (x = 0-0.6) obtained after irradiation by UV light for 10 min. The inset of (a) shows their NIR-persistent luminescence spectra. (d) Mechanism diagram of persistent luminescence in the ZAMG:Cr^{3+} phosphors.

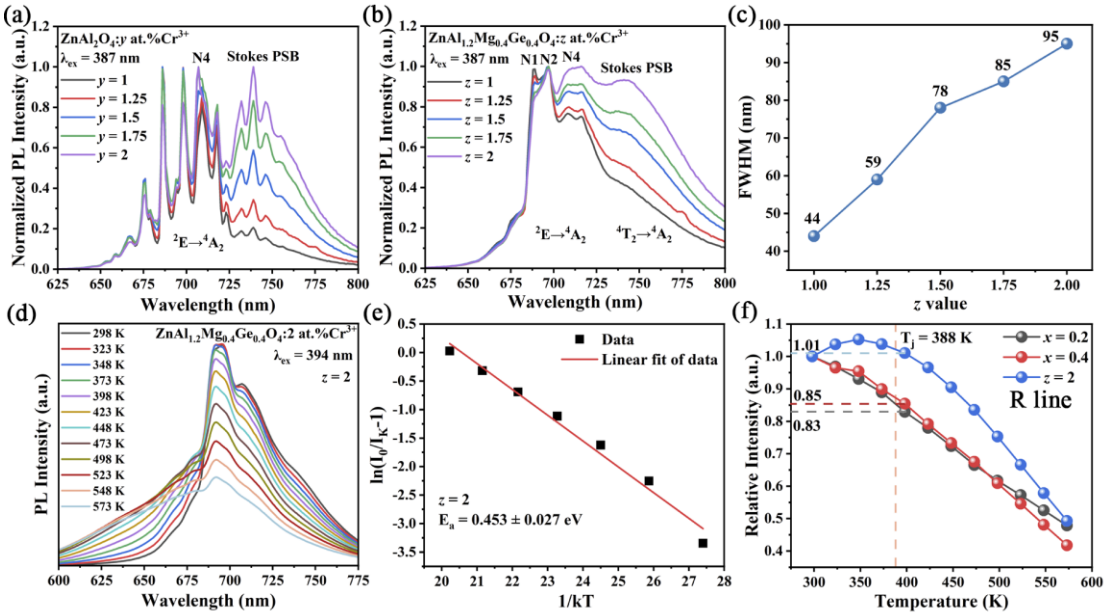

Fig. 8. Normalized PL spectra of (a) ZAO:Cr^{3+} (y = 1-2) and (b) ZA(MG)$_{0.4}$:Cr^{3+} (z = 1-2) under excitation at 387 nm at RT. (c) The variation of FWHM of ZA(MG)$_{0.4}$:Cr^{3+} as a function of z value. (d) Temperature-dependent PL spectra and (e) the Ln(I_0/I_K-1) *vs*. 1/kT plot for the ZA(MG)$_{0.4}$:Cr^{3+} (z = 2) sample. (f) is the temperature dependence of integral PL intensity of R line of the ZAMG:Cr^{3+} (x = 0.2, 0.4) and ZA(MG)$_{0.4}$:Cr^{3+} (z = 2) samples.

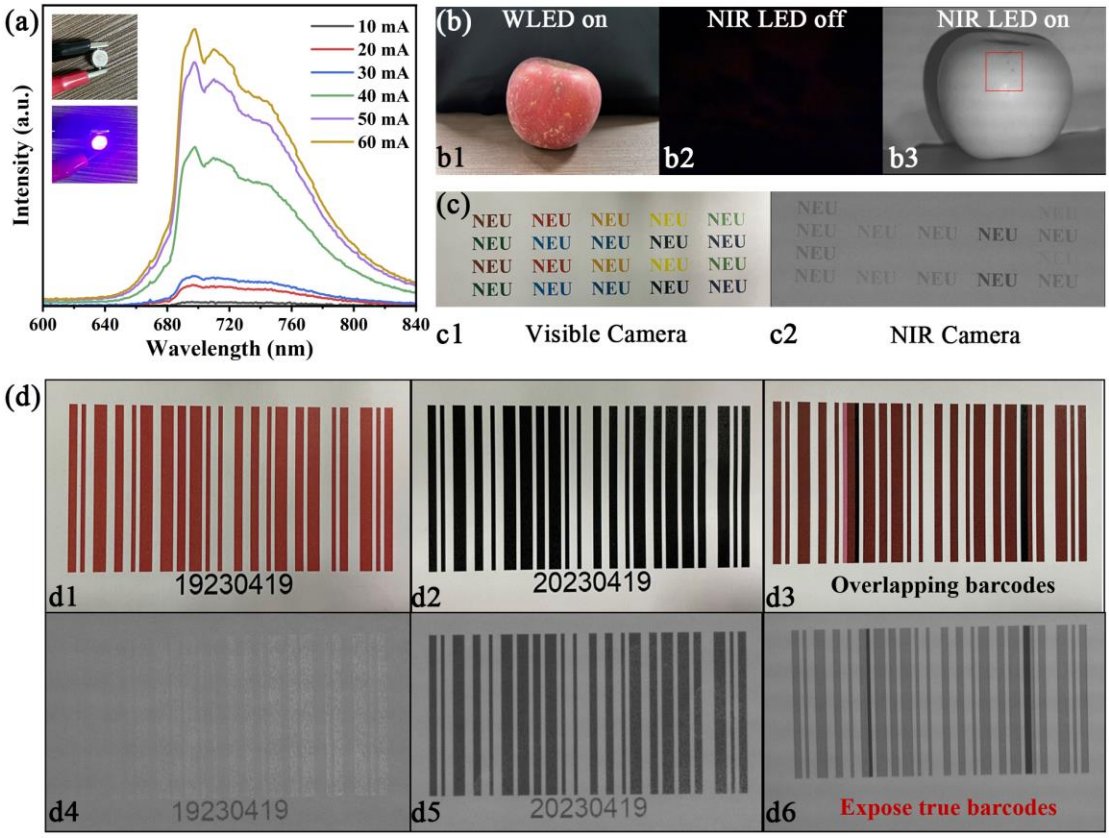

Fig. 9. (a) EL spectra of the fabricated NIR pc-LED. The insets show the images of the NIR pc-LED device under the lighted and unlighted states. Photographs of (b) apple, (c) printed words in different colors, and (d) barcodes in red or black detected by visible camera or NIR camera under corresponding white light or NIR pc-LED irradiation.

Declaration of interests

☒The authors declare that they have no known competing financial interests or personal relationships that could have appeared to influence the work reported in this paper.

☐The authors declare the following financial interests/personal relationships which may be considered as potential competing interests: